# LITHOGRAPHY-FREE MICRO- AND NANOSTRUCTURING BASED ON CONVENTIONAL PLASMA ETCHING

An Inaugural Dissertation
for Obtaining of the Degree
Doctor of Natural Sciences
(Dr. Rer. Nat.)

Presented at
Fachbereich Physik
Universität Kassel
Universität des Landes Hessen

by
Georgi Todorov Georgiev
from Sofia, Bulgaria

Kassel
28 April 2004

Supervisor: Prof. Dr. R. Kassing

First Referee: Prof. Dr. R. Kassing

Second Referee: Prof. Dr. K. Röll

Examination Board: Prof. Dr. R. Kassing
Prof. Dr. K. Röll
PD Dr. E. Oesterschulze
PD Dr. S. Fritzsche

Day of the Oral Examination: 26. May 2004

# Table of contents

# Introduction

Miniaturization of mechanical systems promises unique opportunities for new directions in the progress of science and technology. Micromechanical devices and systems are inherently smaller, lighter, faster, and usually more precise than their macroscopic counterparts. However, the development of micromechanical systems requires appropriate fabrication technologies that enable the following features in general systems:

- Definition of small geometries
- Precise dimensional control
- Design flexibility
- Interfacing with control electronics
- Repeatability, reliability, and high yield
- Low cost per device

The manufacturing of microsystems uses traditional semiconductor process technologies. However, the 3D micromechanical elements are sufficiently different from mainstream semiconductor devices and require new process steps and manufacturing equipment. Double-side lithography and wafer-level aligned bonding is now regularly used for high volume MEMS production [1]. Both micromachining and microelectronic fabrication steps start with photolithography followed by structuring (*Top-Down approaches*). Therefore, the photolithography becomes crucial for fulfilling the above-described requirements. Widespread method is the UV lithography, but it has its limits concerning the dimensions of desired structures. For this reason, advanced lithography methods have been developed, such as X-Ray lithography [2], charged particle beam lithography [3], stereolithography [4], etc. Main disadvantages of these methods are that they are restricted to plane surfaces and extremely cost-intensive. The ITRS microelectronic roadmap presents its prognosis for the near future of microelectronic technology within about ten years showing that the conventional Top-Down Approaches will meet their limit at ~ 50 nm [5]. To keep on scaling down, a new route for the technology must be opened.

As a result from the meeting of traditional fields of science, like physics, chemistry, biology and engineering, new technology was created – *Nanotechnology* [6]. It is reasonable to point out that the word “nanotechnology” is used to describe many types of research and structures where the characteristic dimensions are in the range of 1 – 100 nm. An integral part of the nanotechnology is the self-adjusting technique. It has the potential to replace the top-down approaches with so-known *Self-Assembly* techniques. Self-Assembly offers the possibility from single atom, molecule or even larger structures to build completely functional devices. Therefore, these techniques are called *Bottom-Up approaches* [7]. It is believed that Self-Assembly is the way to bridge the microscopic and nanoscopic worlds. However, these techniques are not in conventional use, since they have limits concerning the compatibility with the conventional technological processes currently applied in IC and MEMS technology.

Therefore, the aim of this work is to find ways to meet the conventional technique with Self-Assembly and to develop a new technology for self-adjusted, lithography-free micro- and nanostructuring. The unique properties of the conventional plasma etching process, concerning its mechanism and angular dependence of the etching rate are proposed to be the key element in this thesis that can be used for fulfilling this task. Plasma etching combined with self-adjusted and self-assembly techniques, opens a new route for combining the Top-Down with Bottom-Up approaches.

Because silicon and silicon dioxide are used as substrate materials, in Chapter 1 a brief description about their properties is given. Additionally, discussion about the silicon oxidation mechanism is given, since this process is an integral part of self-adjusting technique, giving possibilities for nanostructure fabrication. Structuring silicon and silicon dioxide is important in both MEMS and IC technologies. Therefore, Chapter 2 deals with the mechanism behind wet etching of these materials. Through this mechanism, it is demonstrated why this process is suitable for microstructure, but not for nanostructure fabrication. Chapters 3 – 5 are the main part of the thesis. In Chapter 3 a general description of plasma and glow discharges is given with focus on aspect of their technical applications. Additionally, the etching mechanism of silicon and silicon dioxide is shown. The angular dependence of etching rate of silicon and silicon dioxide is also discussed. The combination of the self-adjusting silicon oxidation, silicon dioxide plasma etching mechanism and the angular dependence of the etching rate, raise the curtain for novel routes for nanostructuring. This is demonstrated in Chapter 4, where a novel self-adjusting technique for fabrication of nanostructures is shown. The capability of this technique for technological application was demonstrated through fabrication of SNOM calibration standards. Chapter 5 presents the possibilities of *Natural Lithography* for fabrication of nanostructures. For this reason a self-assembly of silicon dioxide spheres (bottom-up approach) is used as masking layer with respect of conventional photolithography patterning of silicon dioxide layer. Utilizing again plasma etching, nanostructures formation is feasible with extremely little efforts.

# Chapter 1

# Silicon and silicon dioxide as basic materials for micromachining

In semiconductor technology, silicon and silicon dioxide have found extensive use in last decades. Silicon widespread use in microelectronics is mainly due to the advent of hyper-pure semiconductors and of a technology, which allows the controlled addition of foreign atoms in well-specified quantities. The crystal and electronic structure of silicon gives the semiconductor properties needed for microelectronic circuits. In addition, silicon offers a stable high quality native oxide even at room temperature. Furthermore, silicon has desirable mechanical properties, which makes it ideal for MEMS (*Micro-Electro-Mechanical-System*) devices.

This chapter is focused on the main physical properties of silicon and silicon dioxide. The possibility of structuring silicon, defined by its crystal planes, makes it suitable for bulk micromachining. Silicon dioxide, especially its dielectric properties is ideal for passivation and masking layer during developing of microstructures.

## 1.1 Silicon

### 1.1.1 Physical properties of silicon

Silicon has a tensile strength greater than steel and is almost perfectly elastic, making it a versatile material for use in MEMS devices [11]. Its crystalline structure is well-suited to the fabrication of miniature precision devices.

The fabrication of MEMS devices and microelectronic components needs silicon substrate with very high crystalline perfection and must have impurities concentration in the parts per billion atoms range. The method of obtaining such single crystal silicon consists of several steps. After refining the raw material (quartzite), multi stage process is performed for producing *electronic grade polysilicon*. From this polysilicon, single crystal silicon is grown utilizing different methods such as *Czochralski crystal growth (CZ)* or *float zone (FZ) growth* [12].

Silicon is an indirect band gap semiconductor with a band gap of 1.11 eV. The electrical properties of silicon can be varied significantly by the addition of impurities. The pure material has impurities lower than $10^{13}$ cm$^{-3}$ to meet the needs for device application. A dopant (n- or p- type) can be added for producing an appropriate doped crystal. The doping is capable in the range of $10^{20}$ cm$^{-3}$ for n-type and $>1\times10^{20}$ cm$^{-3}$ for p-type dopants respectively [13]. This doping is important not only for electronics, but also for MEMS applications. Heavily p-doped silicon has lower etch rate than pure material and therefore can be used as etch stop layer against anisotropic wet etching [14].

The most important silicon properties are summarized in Table 1:

| Property | Measure |
|---|---|
| Crystal structure | Diamond |
| Melting point | 1,412°C |
| Thermal expansion coefficient | $2.6\times10^{-6}$ °C $^{-1}$ |
| Density | 2.33 g/cm$^3$ (solid)<br>2.53 g/cm$^3$ (liquid 1,421°C) |
| Young's modulus for 300K | $Y_{111}=18.5\times10^{11}$ dyn/cm$^2$<br>$Y_{110}=17\times10^{11}$ dyn/cm$^2$<br>$Y_{100}=13\times10^{11}$ dyn/cm$^2$ |
| Knoop hardness | 1,150 kg/mm$^2$ |
| Band gap energy | 1.11 eV |
| Mobility electrons | ≤ 1,400 cm$^2$/Vs |
| Mobility holes | ≤ 450 cm$^2$/Vs |
| Intrinsic resistivity | $2.3\times10^5$ Ωcm |
| Dielectric constant | 11.8 |

Table 1. Basic mechanical properties of Silicon considered at 300 K [15].

### 1.1.2 Crystal structure of silicon

Silicon has a diamond cubic structure (Figure 1.1) that can be described as two interpenetrating face-centered cubes displaced from each other along x-y-z axes for ¼ of $a_0$, where $a_0$ is the lattice spacing i.e. the length of the unit cell. Lattice constant of silicon is 5.43 Å, 8 atoms belong to single unit cell. The atoms are surrounded by four others in tetrahedral arrangement. The angle between two neighbor atomic bonds is 109°28'.

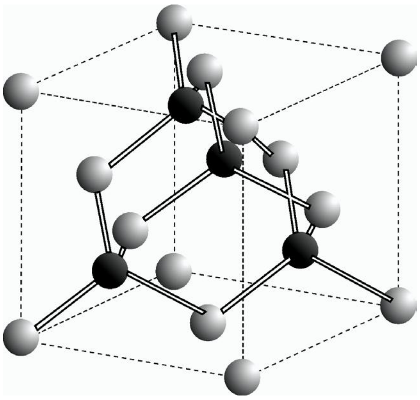

Figure 1.1. A unit cell of the silicon lattice. It has the same structure as cubic diamond. Silicon forms four covalent bonds, forming tetrahedrons [13].

Crystal planes and directions are characterized by sets of three indices (Figure 1.2), the so-called Miller indices [16]. They are written as (hkl) and represent the reciprocals of distances where a plane is intersecting the x-y-z axes. The round brackets represent the crystal plane and the square brackets express crystallographic direction.

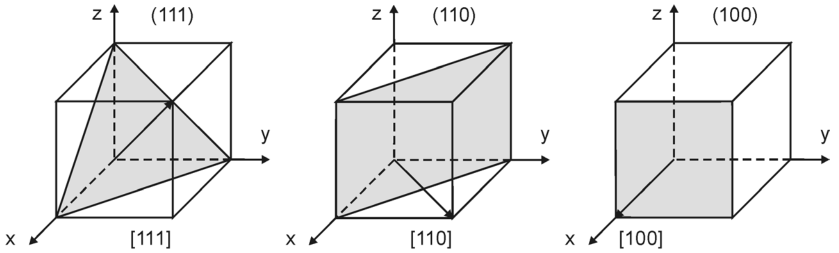

Figure 1.2. Miller indices of important crystal planes (shadowed areas) and directions in silicon crystal.

Various structural properties of silicon depend on crystal orientation, as do many MEMS fabrication steps [1]. Figure 1.2 shows the important directions in respect to etching behavior. This is going to be discussed in 0.

## 1.2 Silicon dioxide

Silicon dioxide is one of the most commonly encountered dielectric materials in electronic and MEMS manufacturing. This material has gained importance in the technology due to its masking and surface passivating capabilities.

### 1.2.1 Silicon dioxide properties

$SiO_2$, especially its form quartz, has a well-defined local structure: four oxygen atoms are arrayed at the corners of a tetrahedron around a central silicon atom (Figure 1.3). The bond angles around O-Si-O are essentially the tetrahedral angle, 109° 28'; the Si-O distance is 1.61 Å with very little variation. The oxygen "bridge" bonds between silicon atoms give $SiO_2$ many of its unique properties. The bond angle of Si-O-Si bonds is nominally about 145°, but can vary from about 100° to 170° with very little change in bond energy [15]. Furthermore, rotation of the bond about the axis is almost completely free. The result of this flexibility in the bridge bonds is that $SiO_2$ can very easily form amorphous materials (Figure 1.3). Essentially all deposited and thermally grown oxides in semiconductor processing are amorphous. Unlike e.g. amorphous silicon, amorphous silicon dioxide will not crystallize upon annealing at normal temperatures. The amorphous structure tends to be very "open": even in thermally grown oxides, channels exist through which small positive ions such as $Na^+$ and $K^+$ can readily migrate [17]. These ions can move under the influence of electric fields within the gate oxides of MOS transistors, causing shifts in the voltage at which the transistor turns on ("threshold shifts"). Exclusion of such ions is imperative for reliable operation of MOS transistors and integrated circuits.

Silicon dioxide is normally quite stable chemically, which makes it an excellent masking material for etching processes. This is the only native oxide of a common semiconductor, which is stable in water and at elevated temperatures [15]. The whole of planar electronics processing and the modern IC industry has been made possible by the unique dielectric properties of silicon dioxide. The functions of silicon dioxide are highly varied such as passivation of the p-n junctions, isolation of the gate in MOS transistors, masking layer for etching, diffusion, ion implantation, etc. [15]

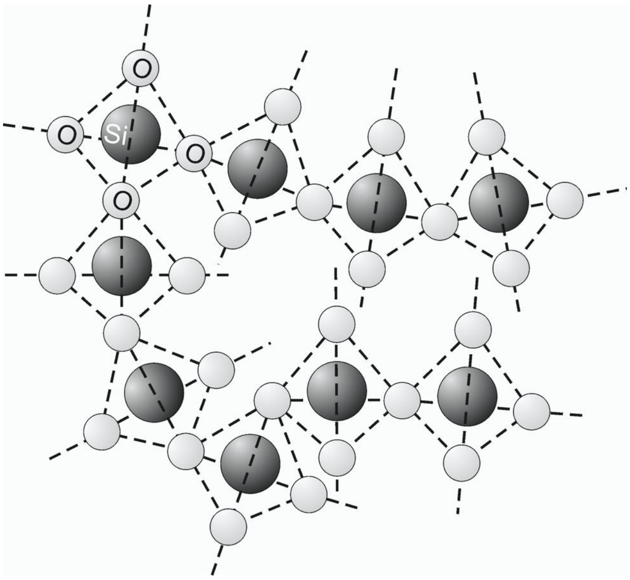

Figure 1.3. Schematic view of silicon dioxide, tetrahedra arranged in a random pattern. Each silicon atom is connected to four oxygen atoms, and each oxygen atom is bonded to two silicon atoms. The bulk material displays a band gap of approximately 8 eV.

All these applications stipulate different requirements towards the parameters of silicon dioxide. When the layer is used as an etching mask, the coating must be amorphous, homogeneous and no pores or cracks must occur. Layers used for passivation must have very good dielectric properties, high bulk and surface resistance and high breakdown voltage. The properties of silicon dioxide strongly depend on the obtaining method. Some of the common properties of silicon dioxide are listed in Table 2:

| **Property** | **Measure** |
|---|---|
| DC resistivity | $10^{14} – 10^{16}$ Ωcm, 25°C |
| Density | 2.27 g/cm$^3$ |
| Dielectric constant | 3.8 – 3.9 |
| Dielectric strength[1] | $(5 – 10)\times10^6$ V/cm |
| Energy gap | ~8 eV |
| Linear expansion coefficient | $5.0\times10^{-7}$ °C$^{-1}$ |
| Melting point | ~1,700 °C |
| Molecular weight | 60.08 |
| Stress in film on Si (compression) | $(2 – 4)\times10^9$ dyne/cm$^2$ |

Table 2. Properties of thermal silicon dioxide [18].

---

[1] Dielectric strength is defined as the maximum electric field required to produce a dielectric breakdown through the material.

### 1.2.2 Oxidation of silicon

Silicon has a great affinity to oxygen. Thin silicon dioxide film (~1 – 5 nm) occurs even at room temperature onto cleaned silicon surface [11]. The most common method for obtaining silicon dioxide is thermal oxidation with dry oxygen or steam oxidation (mixed flow of oxygen and water vapor) or anodic oxidation, etc. The desired thickness and properties of the silicon dioxide determine, which method can be utilized. For example, a $SiO_2$ layer with the densest structure is produced by dry oxidation. Wet oxidation is preferable when thicker layer is needed [12].

The possible reactions, which take place by dry or wet oxidation respectively, are:

$$Si + O_2 \rightarrow SiO_2 . \qquad (1.1)$$

$$Si + 2H_2O \rightarrow SiO_2 + 2H_2 . \qquad (1.2)$$

Thermal oxidation takes place at temperatures of 700 – 1300°C. The properties of the layer can be varied by gas additions in the oxidant [19, 20]. The mechanism of thermal oxidation of planar silicon surface can be described as follows:

1. Gas phase transport of the oxidant to the silicon substrate and adsorption onto the surface;
2. Diffusion of the oxidant through the already existing thin oxide layer to the non-reacted silicon on the Si-$SiO_2$ interface;
3. Chemical reaction leading to formation of $SiO_2$ and pushing the silicon-silicon dioxide interface into depth.

For the growth of silicon dioxide layer with thickness $\delta_0$, silicon with thickness $0.45\delta_0$ is consumed. As a result, an expansion of the silicon dioxide's volume can be observed (Figure 1.4 a)). This is clear in view of the fact that the volume of $SiO_2$ molecule is by factor of 2.25 larger than that of single Si atom [21, 22].

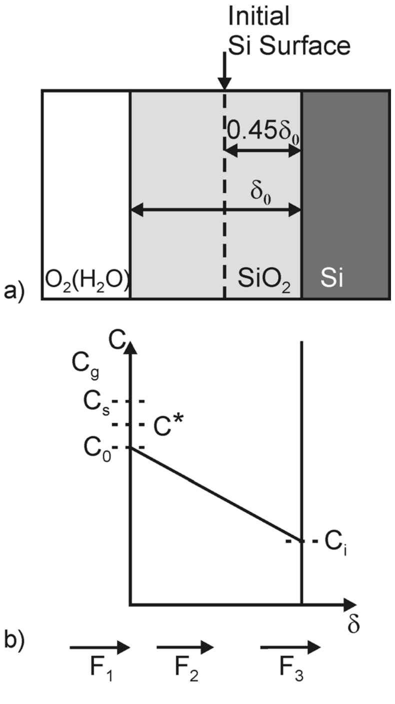

Figure 1.4. Model for the oxidation of plane silicon surface. a) Cross section through the partly oxidized surface. b) The Deal-Groove model of thermal oxidation. In steady-state conditions, the concentration of the oxidant C in the region of the oxide changes linearly. $C_0$ is the concentration of the oxidant at the outer surface of the oxide; $C_i$ is the concentration of the oxidant near the oxide-silicon interface.

Stemming from the oxidation mechanism, the process can be presented schematically (Figure 1.4 b)) as three flows – $F_1$ is the oxidant's flow from the gas phase to the $SiO_2$ layer, $F_2$ oxidant's flow through the $SiO_2$ layer and $F_3$ the oxidant's flow consumed by the oxidation reaction on the $SiO_2$-Silicon interface [23].

The growth rate of the oxide layer can be defined if one knows the number of oxidant molecules $N_1$ incorporated in unit volume of the oxide layer, which are $2.2 \times 10^{22}$ molecules per $1 cm^3$ oxide [15]. Therefore, by oxidation in dry oxygen the same number of molecules is needed, since in case of steam oxidation double amount molecules per cubic centimeter are required (See Eq. 1.2). The rate of growth of the oxide layer is defined by the differential equation [23]:

$$\frac{d\delta_0}{dt} = \frac{F}{N_1} = \left(\frac{k_S C^*}{N_1}\right) \Big/ \left(1 + k_S/\beta + k_S \delta_0/D\right). \tag{1.3}$$

The coefficient of the mass transport from the gas phase is presented as $\beta$ in Eq. 1.3, $D$ is the diffusion coefficient, $k_S$ is the rate constant of the chemical reaction, $C^*$ is the equilibrium concentration of the oxidant in the oxide surface. $C^*$ is related to the partial pressure of the oxidant in the gas phase by Henry's law:

$$C^* = Hp. \tag{1.4}$$

Equation 1.3 is solved by initial conditions $\delta_0(t_0=0) = \delta_i$. To arrive at initial conditions, it is assumed that the silicon surface is already covered with a native oxide layer with thickness $\delta_i$.

The solution of Eq. 1.3 is:

$$\delta_0^2 + A\delta_0 = B(t + \tau). \tag{1.5}$$

For oxidation in dry oxygen $\delta_i = 20$ nm, while for steam oxidation $\delta_i = 0$. The quantity of $\tau$ corresponds to a shift in time coordinate, which corrects for the presence of natural oxide layer $\delta_i$.

Solving the Eq. 1.5 yields the form that gives the oxide thickness as a function of oxidation time:

$$\delta_0 = \left(\sqrt{1 + \frac{t + \tau}{A^2/4B}} - 1\right)\frac{A}{2}, \tag{1.6}$$

where:

$$\tau = \left(\delta_i^2 + A\delta_i\right)/B. \tag{1.7}$$

There are two limiting forms:

1. When the oxidation time is relatively small ($(t+\tau) << A^2/4B$) the oxidation takes place following linear law:

$$\delta_0 \cong \frac{B}{A}(t + \tau), \tag{1.8}$$

where $B/A$ is the linear rate constant and it is defined by:

$$\frac{B}{A} = \frac{k_S \beta}{k_S + \beta}\left(\frac{C^*}{N_1}\right). \tag{1.9}$$

In this case, the growth rate is limited by the reaction at the $SiO_2$-Si interface, $C_i \approx C_0$ and the diffusion is negligible. This is applicable for thin layers.

2. Continuing the oxidation leads to increasing the determinative role of the diffusion, because with the growth of the layer the concentration of the oxidant at the $SiO_2$-Si interface decreases. Hence, for oxidation time $t>A^2/4B$ a transition into diffusion control range occurs. When the oxidation time is relatively large ($(t+\tau) >> A^2/4B$), the oxidation takes place following parabolic law:

$$\delta_0 \cong \sqrt{B\ t}\ , \tag{1.10}$$

where coefficient $B$ presents the parabolic constant of the oxidation rate. The growth rate in this case is limited by the diffusion of the oxidant species through the oxide layer.

The temperature dependence of both linear and parabolic oxidation rate constants follows an Arrhenius law, since the constant $B$ is proportional to $D$ [23]. In the Deal-Groove study, the values of the oxidation rate constants were plotted to determine the activation energies for these constants at different temperatures (Figure 1.5) [23].

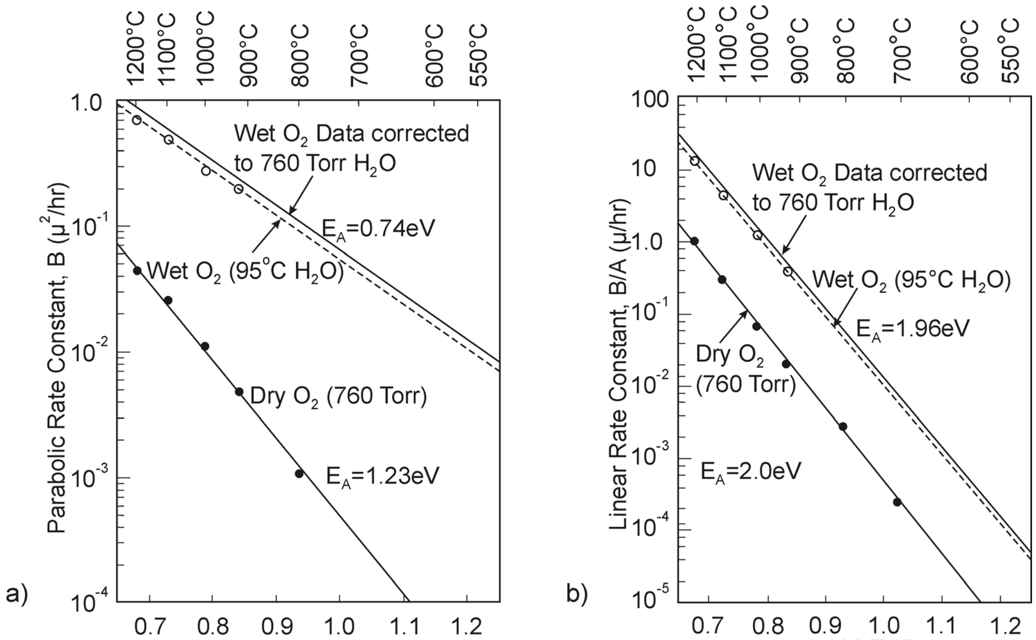

Figure 1.5. The effect of temperature on: a) parabolic constant *B* and b) linear rate constant *B/A* [23].

In case of diffusion limit, the activation energies for dry and wet oxidation respectively are $E_a=1.23eV$ and $E_a=0.74eV$ (Figure 1.5 a)). These values are in good agreement with those activation energies known from bulk fused-silica, and they are found to be $E_a=1.18eV$ for oxygen and $E_a=0.79eV$ for $H_2O$ [24, 25]. By known diffusion coefficient, it is possible to calculate $C^*$ and the values are $C^*=5\times10^{16}\ cm^{-3}$ for oxygen and $C^*=3\times10^{19}\ cm^{-3}$ for water. Therefore, it can be concluded that in case of wet oxidation the growth rate of the layer is higher than that obtained by dry oxidation.

For the reaction limit, the calculated activation energies are $E_a=2.0eV$ for dry and $E_a=1.96eV$ for wet oxidation, respectively. The values are comparable to the one required for breaking a Si-Si bond ($1.83eV$). This shows that in the range where the oxidation depends on the linear rate constant, the process is limited by the reaction on $SiO_2$-Si interface.

Another parameter that has influence on the oxidation is the crystallographic orientation [26]. The constant $B/A$ is related to the kinetics of the reaction at the $SiO_2$-Si interface. The reaction rate constant ($k_S$) depends on the density of the atoms of the surface exposed to the oxidant. $B/A$ is larger for (111)-Si than (100), which means, that for the same oxidation conditions the oxide thickness on (111) will be larger than on (100) [27, 28].

The model of Deal-Groove works fine for description of only planar silicon surfaces when the oxide thickness is larger than 30 nm. However, significant differences occur investigating the oxide layer on structured surfaces. In this case, silicon dioxide growth exhibits a complex mechanical stress distribution, in particular at shaped surfaces, owing to its rheological behavior [29]. The intrinsic compressive stress locally degrades the diffusion rate of the oxidizing species through the already grown oxide layer and furthermore decreases the oxidation rate at the Si – $SiO_2$ interface. Therefore, a reduction of the oxide thickness is observed that depends strongly on the shape of the silicon surface.

In the model of Kao et al. the silicon dioxide is treated as viscous material [26]. Stress relaxation due to the viscous flow is restricted to temperature above the glass temperature of $SiO_2$ ($T_G$ = 965°C) [29]. Senez et al. point to the fact that the silicon dioxide exhibits elastic properties under hydrostatic stress state in view of Hooke's element and creep characteristics under deviatoric stress state [30]. Therefore, this rheological behavior can be described in terms of Maxwell liquid:

$$\dot{\varepsilon}-\left(\frac{\dot{\sigma}}{G}+\frac{\sigma}{\eta}\right)=0, \tag{1.11}$$

where $\dot{\varepsilon}$ is the strain rate, $\dot{\sigma}$ the stress rate, and $\sigma$ is the stress. $G$ and $\eta$ are the shear modulus and dynamic viscosity of silicon dioxide respectively. Below the glass temperature, the viscosity is too big, so the term $\sigma/\eta$ can be ignored, i.e. there is elastic behavior of the material. The mechanical strain in this condition remains constant and cannot be relaxed. They affect the diffusion and oxidation kinetics and provoke the inhomogeneity observed in non-planar silicon dioxide layers.

When the oxidation temperature is above $T_G$, relaxation of strain components occurs. The relaxation time is given by:

$$\tau = \frac{\eta}{G}. \tag{1.12}$$

At the same time, a non-linear dependence of the viscosity on the maximum local stress $\sigma_{max}$ and on the temperature is evaluated in view of Eyring's nonlinear flow model for glasses:

$$\eta = \eta_0 \frac{\sigma_{\max} V_\eta / (2k_B T)}{\sinh\left(\sigma_{\max} V_\eta / (2k_B T)\right)}, \tag{1.13}$$

where $\eta_0$ is the viscosity of stress-free oxide and $V_\eta$ is the activation volume and as can be seen, the stress relaxation must be taken into account even at low temperatures. Concerning the results from Landsberger et al., $\tau$ is expected to decrease, in particular at low temperatures [31]. In view of the long oxidation time at temperatures below $T_G$, the material has sufficient time to relax a substantial amount of the intrinsic stress by viscous flow, while at high temperatures the oxidation time is too short in comparison to $\tau$ for stress relaxation. Vollkopf et al. reported stress value of ~ 30 MPa for low oxidation temperatures and ~ 90 MPa for high temperatures in case of V-groove and inverse pyramidal structures [32]. Therefore, a noticeable decrease of the oxide growth at structures of low radius of curvature at high oxidation temperatures is expected.

# Chapter 2

# Wet Etching

Etching in the technology of microelectromechanical systems and microelectronic fabrication is a process by which material is removed from substrate by chemical reaction. The reagent used for etching is called *etchant*. With the development of the semiconductor technology, etching was applied mostly for thin film patterning after photolithography step. In order to form either functional MEMS or 3-dimensional structures, the bulk of the substrate is etched. For this reason it was named *bulk micromachining*. The standard technological steps for performing etching are shown in Figure 2.1.

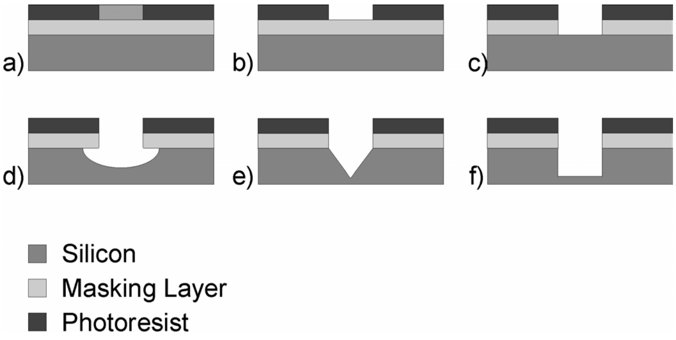

Figure 2.1. Basic technological steps for performing etching. a) Photolithography – the photoresist deposited onto the masking layer is exposed to UV light, b) developing of the photoresist, c) patterning the masking layer d) isotropic etching of substrate. e) and f) anisotropic etching of substrate.

First three steps are connected to photolithography processes, which are necessary to create two-dimensional pattern in oxide or other masking material deposited on the substrate. The pattern defines the mask opening for bulk etching of the substrate. The etching can be *isotropic* if the etching rate is homogeneous in all directions (Figure 2.1 d)) or *anisotropic* if the etching rate is dependent on direction (Figure 2.1 e) and f)).

The very basic mechanism of etching process is shown in Figure 2.2. The etching process consist of three steps:

- Mass transport of reactants through a boundary layer to the surface to be etched
- Reaction between reactants and the film (substrate) to be etched at the surface
- Mass transport of reaction products from the surface through the surface boundary layer.

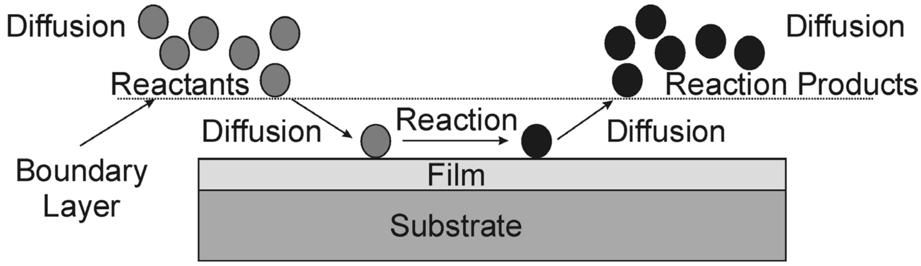

Figure 2.2. General schematic of etching process.

The parameters important to etching processes are: selectivity, anisotropy, etching rate, undercut, tolerance, over etch, feature size control, and loading effects [13]. An important characteristic of the etch process is the *selectivity*, which is defined as the ratio of etching rates of substrate, $ER_{substrate}$, and masking material, $ER_{mask}$, under the same etching conditions:

$$S = ER_{substrate} / ER_{mask} \ . \tag{2.1}$$

If $S > 100$ then the selectivity is very good. For $S = 1$ selectivity is zero. Higher selectivity enables deeper etching and higher value of *vertical aspect ratio*. This is the ratio of height and width of the structure. *Undercut* and *tolerance* are related to the degree to which an etch process fails to satisfy the ideal one. *Undercut* is the difference in lateral dimensions between the etched image and mask image. *Tolerance* characterizes the uniformity of etching and is a measure of the statistical distribution of the undercut values.

Wet etching simply can be described as a process of oxidation of the etched material, followed by dissolution of this oxide. The etch solutions, therefore, consist of oxidizer, acid or base to dissolve oxidized surface and diluent media to transport reactants and products through.

There are different kinds of solutions used for wet etching depending on the process (isotropic or anisotropic). The most common are [33]:

- HNA – Hydrofluoric acid + Nitric acid + Acetic acid – this solution is used for polishing and nearly isotropic etching of silicon.
- Alkali hydroxides – most counted etching solution, because of its selectivity, fast etching, easy to handle and readily available.
- TMAH – Tetra Methyl Ammonium Hydroxide – this solution is MOS/CMOS compatible, because it contains no alkali metals but has nearly the same etch characteristics as KOH.

## 2.1 Anisotropic etching of silicon in alkaline solutions

The anisotropic etching in alkaline solutions is a widespread process for structuring silicon surfaces. It has been used to fabricate a variety of active and passive, three-dimensional MEMS devices. The material properties and its crystallographic structure influence the final shape of the microstructure. Anisotropic etching of single crystal results in perfect geometry shapes composed of flat and smooth crystallographic planes.

The structuring is based on the different etching rates depending on the silicon crystallographic orientation. The [111] direction has the lowest etching rate in alkaline solutions, therefore for appropriate mask alignment, on different crystallographic oriented substrates several structures can be created [34]. In Figure 2.3 the anisotropic etching examples are shown:

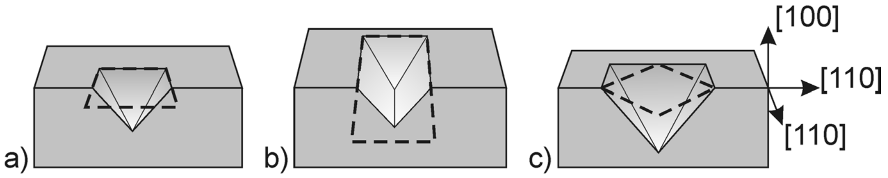

Figure 2.3. The resulting structures from anisotropic etching of (100) oriented silicon substrate through: a) square mask pattern gives an inverse pyramidal structure and b) rectangular mask pattern results in V-groove formation. c) the mask pattern is aligned on 45° toward [110] direction obtaining inverse pyramid. The dashed line represents the mask opening.

A square and a rectangular pattern are defined in an oxide mask following the steps a) – c) from Figure 2.1 with sides aligned along [110] directions on (100) oriented silicon wafer. When the etching is through square pattern, the result is a pyramidal tip with well-defined (111) sidewalls (Figure 2.3 a)) at angles of 54.74° to the surface. A rectangular pattern aligned along [110] on a (100) wafer results to long *V-shaped grooves* (Figure 2.3 b)). During the etching, if the mask pattern deviates from the square (rectangular) form or alignment along [110] direction firstly occur a rough and irregular etch contour between the small (111) planes, which originates from the corners of the mask. In the next step, these planes are developed at the expense of the neighboring ones and the mask is underetched. The etching of the contours between the (111) planes passes with higher etching rate until the irregular planes disappear. Since the (111) has slowest etching rate, a pyramid or V-groove is built with smooth sidewalls, which lay under the mask (Figure 2.3 c)). The amount of underetching scales with the deviation from [110]. The resulting distinctions are desired in some MEMS fabrication steps [35, 36].

In order to obtain detailed data on the crystal orientation dependence of the etch rate, pre-etch alignment targets are used to outline the planes of interest. Seidel et al. used a wagon-wheel or star shaped masking pattern, consisting of radially divergent segments with an angular separation of one degree [37]. After etching, a blossom-like figure was obtained due to the total underetching of the masking layer in the vicinity of the center of the pattern, leaving an area of bare exposed silicon. The radial extension of this area depends on the crystal orientation of the individual segments, leading to different amount of lateral underetching. In order to establish the lateral etch rate as a function of crystal orientation, the width of the bulged masking layer was measured. The results are plotted on polar coordinate diagram (Figure 2.4), where the etching rates shown are normal to the actual crystal surface:

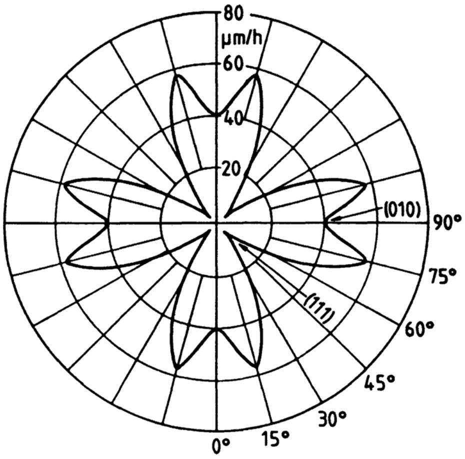

Figure 2.4. Lateral underetching rate as a function of orientation of (100) silicon wafer using a 50% KOH solution at temperature of 78°C [37].

The distance from the origin to the polar plot surface indicates the rate for that particular direction. It can be seen the deep minima at the (111) planes and that the etch rate depends linearly on misalignment. These observations have important consequences for the interpretation of anisotropy of wet etching.

### 2.1.1 Anisotropic etching reaction mechanism

The etching in alkaline solutions follows one and the same mechanism, where the process results from redox reaction. In this reaction, the silicon surface is oxidized by hydroxide ions and the water is reduced leading to evolution of hydroxide ions and elementary hydrogen. The reaction can be written as [38]:

$$\begin{aligned} Oxidation&: \; Si + 4OH^- \rightarrow SiO_2 + 2H_2O + 4e^-. \\ Reduction&: \; \underline{4H_2O + 4e^- \rightarrow 4OH^- + 2H_2 \uparrow.} \end{aligned} \tag{2.2}$$

$$Si + 2H_2O \rightarrow SiO_2 + 2H_2 \uparrow.$$

According to Eq. 2.2 in the first step, the hydroxyl group is attached to silicon atom leading to oxidation and at the same time, injection of four electrons into conduction band of the silicon. During the final step, the water molecule is reduced to hydrogen and hydroxyl ions. In fact the etch rate of $SiO_2$ in KOH solution is smaller than that of silicon [37]. This means that, following the above described reaction, the oxidized surface could act as etch stop layer. In reality, this effect cannot be observed. Actually, the hydroxyl ions are used to create soluble highly complex species. The reaction is:

$$SiO_2 + 2OH^- \rightarrow H_2SiO_4^{2-}. \tag{2.3}$$

Due to the high pH environment the $H_2SiO_4^{2-}$ is converted to $SiO_2(OH)_2^{2-}$. Therefore, the overall reaction is:

$$Si + 2OH^- + 2H_2O \rightarrow SiO_2(OH)_2^{2-} + 2H_2 \uparrow . \qquad (2.4)$$

In accordance to the above-described mechanism, the etch rate depends on the concentration of KOH. This dependence is described in Arrhenius form at standard conditions [37, 39]. In fact, it can be expressed as:

$$R = k_0 [H_2O]^4 [KOH]^{\frac{1}{4}} e^{-E_a/k_B T}, \qquad (2.5)$$

which is proved to be in close agreement with the experimental data.

The above described mechanism gives an explanation how the dissolution of silicon in alkaline media takes place. However, for explanation of the anisotropic behavior a detailed examination of the etching processes is necessary. There are numerous models describing the anisotropy in etching for different Si orientations. The most widespread are those proposed by Seidel et al. [37, 39] and Elwenspoek et al. [40].

### 2.1.2 Anisotropic etching theoretical models

In the first model, it is assumed that the anisotropy is due to differences in energy levels of backbond associated surface states for different crystal orientations. Seidel et al. have considered that during the oxidation step (Eg. 2.2) four electrons are injected into the conduction band, originating from the reacting hydroxide ions. In case of (100) silicon planes, two of these electrons are transferred via dangling bonds[1] surface states and the other two via back-bond surface states. As a consequence of the electronegativity of the oxygen atoms, the two bonded hydroxide groups at the silicon atom reduce the strength of the silicon back-bonds. The breaking of the back-bonds is considered to be rate limiting. The breaking is induced by thermal excitation of electrons from the orbitals of the respective surface states into the conduction band. The energy level of the back-bond states is assumed to be varying for different surface orientation, being lowest for (111) planes. These planes have only one dangling bond to react with the hydroxide ion. Then in the second step three back-bonds must be broken. A detailed description of the model is given elsewhere [41, 42].

The model of Elwenspoek intends that the degree of atomic smoothness of various surfaces is responsible for the anisotropy. A nucleation barrier that is absent on rough surfaces controls the kinetics of smooth faces. The terms rough and smooth are defined as the state of the crystal planes by which the lower respectively highest bond density is presented [43]. The (111) plane in silicon crystal is example for a smooth face. Etching or growing of material starts at active kink sites[2] on step (island by growth or cavity by etching). A perfectly flat (111) surface in silicon lattice has no kink positions, while the (001) face has two back-bonds and two dangling bonds for every atom. Following this one can conclude, that in case of (111) it will be harder to brake three back-bonds for creating an adatom-cavity pair than in case of (001) face. Therefore, the step-free

---

[1] A chemical bond associated with an atom on the surface layer of a crystal or inside an amorphous material. The bond does not join with another atom of the crystal, thus producing a defect in the material.

[2] Atoms with as many bonds to the crystal as to the liquid.

energy will be different at different crystallographic orientations. Smooth faces grow and etch with rate [40]:

$$R \propto \exp\left(\frac{-\pi\gamma^2}{h\rho k_B T\Delta\mu}\right), \tag{2.7}$$

where $\gamma$ is the step-free energy, $h$ represents the height of the step, $\rho$ the density of the solid material, $k_B$ the Boltzmann constant, $T$ the absolute temperature, and $\Delta\mu$ the chemical potential difference between silicon atoms in solid state and the solution.

Equation 2.7 predicts that faces with large step-free energy grow and etch much slower than faces with smaller step-free energy. $\gamma$ and $\Delta\mu$ depend on temperature and ambient solution, hence the degree of anisotropy will depend on the etchant. This can explain why in certain solutions the silicon etching is isotropic.

## 2.2 Isotropic etching of silicon dioxide

The etching of silicon dioxide in alkaline solutions is described with the reaction [37]:

$$SiO_2 + 2OH^- \rightarrow H_2SiO_4^{2-}. \tag{2.8}$$

Experimental results show that there is a linear dependence of the etch rate of $SiO_2$ and the concentration of hydroxide ions. There is a certain concentration (~ 35%) above which, the etch rate of silicon dioxide will decrease. This corresponds roughly to the square of the molar water concentration.

The selectivity (Eq. 2.1) between silicon and silicon dioxide is very important for practical application when the oxide is used as a masking layer during etching. For using $SiO_2$ as masking layer, it must be structured. The steps are given in Fig. 2.1. For creating a pattern onto the silicon dioxide normally an aqueous 40% HF is used. The etching takes place following the reaction:

$$SiO_2 + 6HF \rightarrow H_2SiF_6 + 2H_2O. \tag{2.9}$$

For improving the masking properties of the photoresist, generally a buffered HF solution is used, where the hydrofluoric acid is diluted with ammonium fluoride. The addition of $NH_4F$ to HF controls the pH value and prevents depletion of the fluoride ions, thus maintaining stable etching performance.

The etching rate of silicon dioxide in HF media depends linear on the concentration of $HF$ and $HF_2^-$, where $HF_2^-$ plays a major role [44]:

$$R = 2.5[HF] + 9.66[HF_2^-] + C. \tag{2.10}$$

The etching of silicon dioxide in HF solutions is strongly isotropic. In most cases, the photoresist does not stick ideally on the $SiO_2$ and underetching occurs. If very small features are needed the wet chemical etching is not the optimal method for structuring. For this reason dry etching methods were developed and they will be discussed in the next chapter.

# Chapter 3

# Dry etching

As it was described in the previous chapter the anisotropy of wet etching of monocrystalline silicon depends on the crystal orientation. This means that the structuring of the substrate is strongly related to this material feature. When a specific profile is desired wet etching is not appropriate and another process is needed. Dry etching, also called plasma etching, is a group of methods for structuring the substrate in the gas phase, physically by ion bombardment, chemically by chemical reaction, or by combination of both. Depending on the etching mechanism, isotropic, directional, or vertical etch profiles can be obtained [45-47]. Utilizing dry etching, the desired profiles can be generated in polycrystalline as well as in single crystalline and amorphous materials [48]. The degree of anisotropy is controlled by the plasma conditions [49-52].

The most commonly used dry etching methods in IC manufacture and micromachining are those based on glow discharges. Glow discharges are weakly ionized media at low gas temperature, working at low pressure. The words “plasma” and “glow discharge” are used synonymously as technological processes. The glow discharge regime owes its name to the fact that the plasma is luminous. The gas glows because the electron energy and number density are high enough to generate visible light by species that were excited by collisions. The choice of dry etching technique is related to some plasma parameters such as electron and ion temperature, and electron and ion current density.

## 3.1 Basic plasma parameters

Generally, the plasma can be described as an ionized gas containing electrons and positive ions in equal quantities and a different number of non-ionized molecules [53]. There are several types of plasmas depending on the electron density ($n_e$) and electron temperature ($T_e$) (Figure 3.1) [47]. The electron and ion density are equal (on average); this density is often known as plasma density. The average speed of electrons is higher compared with those of the ions and neutrals due to both the high temperature and low mass of the electrons [54].

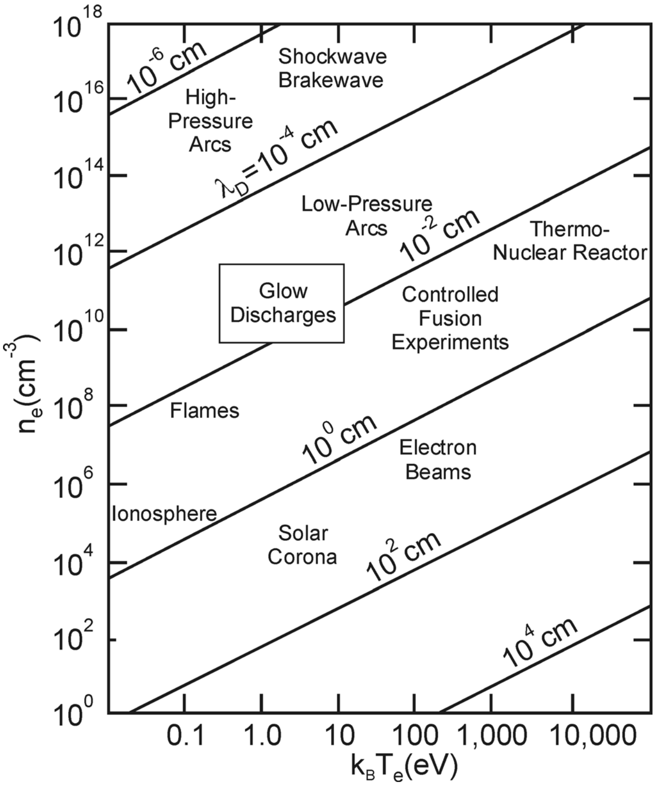

Figure 3.1. Electron density ($n_e$) versus thermal energy ($k_BT_e$) for plasmas with Debye length ($\lambda_D$) from $10^{-6}$ to $10^{4}$ cm [55].

### 3.1.1 Debye shielding

If an isolated substrate is introduced in the plasma, electrons and ions strike it. The absolute values of the current density of electrons, $j_e$, and ions, $j_i$, are defined as follows [53]:

$$j_e = \frac{|e| n_e \bar{c}_e}{4}, \qquad j_i = \frac{|e| n_i \bar{c}_i}{4}, \tag{3.1}$$

where $\bar{c}_e$ and $\bar{c}_i$ represent the mean speed and $n_e$ and $n_i$ are total number of electrons and ions, respectively. The substrate starts to build a negative charge and negative potential with respect to the plasma, because $\bar{c}_e \gg \bar{c}_i$. At steady state net flux, a potential is built up and only electrons with high enough kinetic energy can reach the surface counterbalancing the incoming ion current. Due to the negative charge of the substrate, slow positive ions will build a net positive space charge around it. The positive ions shield the negative potential, which is known as Debye shielding (Figure 3.2).

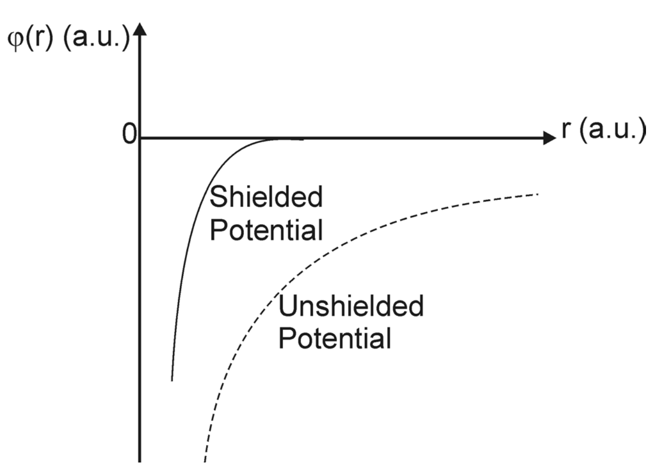

Figure 3.2. Debye potential (solid line) and unshielded Coulomb potential (dashed line) as a function of a distance.

The electrostatic potential produced by isolated point charge $e$ at distance $r$ is given by:

$$\varphi(r) = \frac{e}{4\pi\varepsilon_0}\frac{1}{r}, \tag{3.2}$$

where $\varepsilon_0$ is the permittivity of vacuum.

The plasma consists of many charged particles and the electrostatic potential inside the plasma is given by the sum of all potentials. Since the potential produced by a positive (negative) charge attracts negative (positive) charge, the net potential around a specific charge becomes smaller than that given by Eq. (3.2), approaching zero much faster than $1/r$ as $r$ increases. Therefore, to obtain the solution if other charges are present, using the Boltzmann relation with $n_i = n_e$ the Poisson equation becomes:

$$\left(\frac{d^2}{dr^2} + \frac{2}{r}\frac{d}{dr}\right)\varphi(r) = -\frac{en_i}{\varepsilon_0}\left(1 - \exp\left(-\frac{e\varphi(r)}{k_B T_e}\right)\right). \tag{3.3}$$

When $e\varphi(x) \ll k_B T_e$ then:

$$\left(\frac{d^2}{dr^2} + \frac{2}{r}\frac{d}{dr}\right)\varphi(r) = -\frac{e^2 n_i}{k_B T_e \varepsilon_0}\varphi(r). \tag{3.4}$$

The solution of Eq. (3.3) for potential distribution around a specific charge in the plasma is [53, 54, 56, 57]:

$$\varphi(r) = \frac{e}{4\pi\varepsilon_0}\frac{1}{r}\exp\left(-\frac{r}{\lambda_D}\right), \tag{3.5}$$

which in fact is the Debye potential where, the term $\lambda_D$ is the Debye length defined by:

$$\lambda_D = \sqrt{\frac{\varepsilon_0 k_B T_e}{ne^2}}, \tag{3.6}$$

which is one of the most fundamental parameter that characterizes the plasma, and is a measure of the shielding distance or thickness of the sheath. Eq. (3.6) shows that if the potential in the plasma is perturbed, then the plasma reacts to oppose that change. The Debye length describes how the potential perturbation is attenuated in the plasma. For a particular charge at a particular point in the plasma, one needs to consider the sum of the individual interactions with all other charged particles within a sphere centered on the particular point with radius of Debye length. Outside of this sphere, the detailed nature of the interaction becomes inessential and the net interaction is zero. The unperturbed plasma is equipotential except for small fluctuating voltages, which are attenuated over distances of the order of $\lambda_D$ [53]. Consequently, to consider an arrangement of charged particles as plasma, the discharge dimensions must be significantly larger than the Debye length.

## 3.2 Glow discharges

A glow discharge is a self-sustaining type of plasma and is the most used method for transferring a pattern in MEMS and microelectronics technology [1, 13]. The simplest reactor may consist of opposed parallel plate electrodes in a chamber filled with gas at low pressure (see the marked area in Figure 3.1). Applying an adequate potential between these two electrodes, leads to formation of glow discharge. The potential drops rapidly close to the cathode, varies slowly in the plasma region, and changes again close to the anode (Figure 3.3 b)). The electric fields in the system are restricted to sheaths at each of the electrodes. The sheath fields are such as to repel electrons trying to reach either electrode. Electrons originating at the cathode will be accelerated, collide, transfer energy, leave by diffusion and recombination, slowed by potential drop at the anode and get transferred into the outside circuit. The luminous glow is produced because gas molecules emit light after excitation collisions with electrons with enough energy. Since there is a continuous loss of electrons, there must be an equal degree of ionization going on to maintain the steady state. The energy is being continuously transferred out of the discharge and hence the energy balance must be also satisfied. Simplifying, the electrons absorb energy from the field, accelerate, ionize some atoms, and the process becomes continuous.

### 3.2.1 Structure of direct current glow discharge

The complex structure of DC glow discharge is shown on (Figure 3.3 a) [53, 55, 58]. Right after the cathode is the Aston dark space (***1***) with a strong electric field. The electrons are accelerated through this space away from the cathode. This region has a negative space charge, meaning that scattered initial electrons together with the secondary electrons from the cathode outnumber the ions in this region. The electrons posses too low energy to excite the gas, so it appears dark. Beside the Aston dark space, is the cathode glow (***2***). Here the electrons are energetic enough to excite the neutral atoms they collide with. The cathode glow has a relatively high ion density. The axial length of the cathode glow depends on the type of gas and the pressure. The cathode glow sometimes clings to the cathode and masks the Aston dark space. Next to the cathode glow is a relatively dark region (***3***), so called Crookes (cathode) dark space, which has a moderate electric field, a positive space charge and a relatively high ion density. Beside the cathode dark space, is the brightest intensity of the entire discharge. The negative glow (***4***) has relatively low electric field, compared to the cathode glow and is the most intensive on the cathode side. Electrons carry almost the entire current in the negative glow region. Electrons that have been accelerated in the cathode region to high speeds produce ionization, while the slower electrons that have already had inelastic collisions produce excitations. These slower electrons are responsible for the negative glow. The electron number density in the negative glow is about $10^{16}$ electrons/cm$^3$. As these electrons slow down, the energy for excitation is no longer available and Faraday dark space (***5***) begins. The electron energy is low in this region. The electron number density decreases by recombination and diffusion to the walls, the net space charge is very low, and the axial electric field is small.

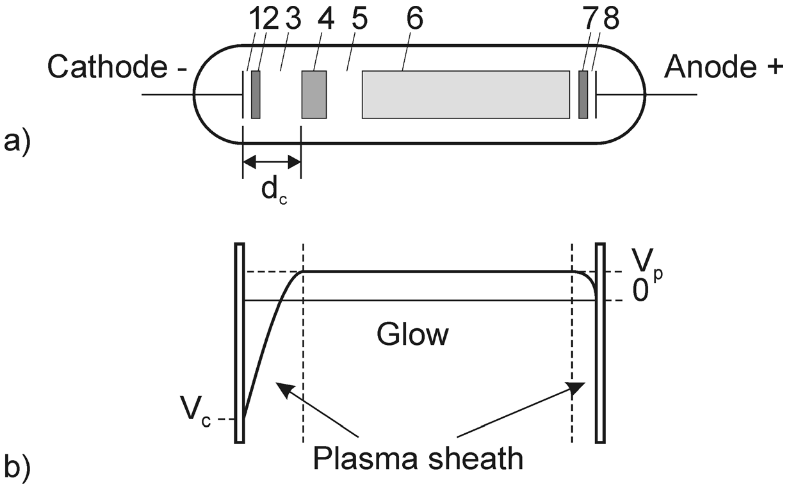

Figure 3.3. DC glow discharge: a) DC glow discharge structure – 1. Aston dark space 2. cathode glow 3. Crookes (cathode) dark space 4. negative glow 5. Faraday dark space 6. Positive column 7. anode glow 8. anode dark space; b) voltage distribution in a DC glow discharge – $V_p$ is plasma potential, $V_c$ – cathode voltage drop.

The entire region between the cathode and the negative glow is also called *Cathode region* with length $d_c$ (Figure 3.3 a)). Most of the voltage drop across the discharge tube occurs here (Figure 3.3 b). This can be explained in following manner. Because the ions are more massive, they accelerate towards the cathode in slower tempo than electrons. Thus, the ions spend more time in Crookes dark space and their concentration is greater than that of the electrons. The net effect is a very large field in front of the cathode. Consequently, the largest part of the voltage between the cathode and the anode ($V_c$) is dropped across the Crookes dark space.

The value of $V_c$ depends on the pressure and distance between the cathode and anode, following the Paschen’s law:

$$V_c \sim p\, d. \tag{3.7}$$

This product gives the Paschen minimum (Figure 3.4). At the Paschen minimum the discharge maintains itself with minimum cathode drop voltage $V_c$ and minimum power dissipation. At constant pressure, on the right side of the minimum the breakdown voltage increases slowly as the distance between the electrodes increases. This occurs, because the electron energy is too low to cause ionization. The sharp rise in the breakdown voltage at the left side is due to fact that the electrode spacing is too small, or the gas density is too low. Electrons are lost to the walls without collision with gas atoms to produce ionization. Typical values in air at a pressure of 1 Torr, at current density of 0.3 mA/cm$^2$, $d_c$ approximately 0.5 cm, result in cathode drop voltage, $V_c$, between 100 to 300 V.

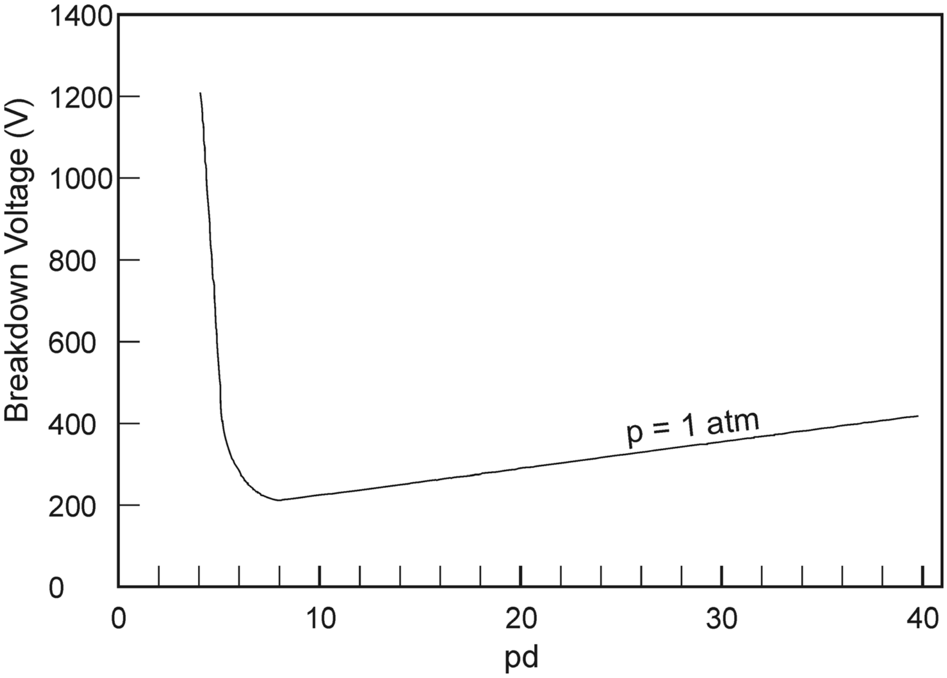

Figure 3.4. The DC breakdown voltage as a function of the product of gas pressure *p* and electrode spacing *d* for the plane parallel electrodes in air [1].

After the Faraday dark space is the positive column (***6***) (Figure 3.3 a)). This is a quasi-neutral area with small electric field, typically 1 V/cm. The electric field is large enough to maintain the degree of ionization at its cathode end. The electron number density is about $10^{15}$ – $10^{16}$ electrons/cm$^3$ in the positive column, and the electron temperature 1 – 2 eV. The next region is anode glow (*7*), which is slightly brighter than the positive column, and not always present. This is the boundary to the anode sheath (***8***). It has negative space charge due to electrons traveling from the positive column to the anode. The electric field is higher than that in the positive column, because the anode pulls electrons out of the positive column.

### 3.2.2 Voltage – current characteristic

The main characteristics of the discharge such as the breakdown voltage, the voltage current characteristic, and structure of the discharge depend on the geometry of the electrodes and the vessel, the gas used, and the electrode material. By adjusting the ballast resistor in the circuit diagram, we can sweep out a voltage current characteristic that is highly nonlinear. The V-I characteristic curve of the space between two planar electrodes is shown on Figure 3.5 [58].

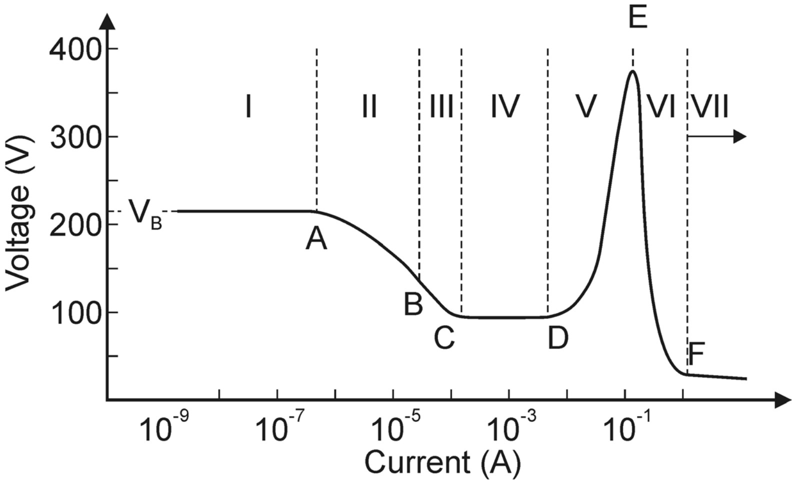

Figure 3.5. V-I Characteristic curve of DC glow discharge. I. Self sustained dark discharge. II. Corona discharge III. Sub-normal glow discharge. IV. Normal glow discharge. V. Abnormal glow discharge. VI. Transition region. VII. Arc discharge.

The regime in section ***I*** on the voltage-current characteristic is termed as dark discharge because, except for corona discharges and the breakdown itself, the discharge remains invisible to the eye.

Between points **A** – **B** *Corona discharges* occur in regions of high electric field near sharp points, edges, or wires in gases prior to electrical breakdown. If the coronal currents are high enough, corona discharges can become visible to the eye, technically called "glow discharges". For low currents, the entire corona is dark, as appropriate for the dark discharges. Related phenomena include the *silent electrical discharge*, an inaudible form of filamentary discharge, and the *brush discharge*, a luminous discharge in a non-uniform electric field where many corona discharges are active at the same time and form streamers through the gas. At point **A** electrical breakdown occurs with the addition of secondary electrons emitted from the cathode due to ion or photon impact. At the breakdown, or sparking potential $V_B$, the current might increase by a factor of $10^4 - 10^8$, and is usually limited only by the internal resistance of the power supply connected to the plates. If the internal resistance of the power supply is very high, the discharge tube cannot draw enough current to break down the gas, and the tube will remain in the corona regime with small corona points or brush discharges being evident on the electrodes. If the internal resistance of the power supply is relatively low, then the gas will break down at the voltage $V_B$, and move into the normal glow discharge regime. The breakdown voltage for a particular gas and electrode material depends on the product of the pressure and the distance between the electrodes, as expressed in Paschen's law (see Eq.(3.7)).

Increasing further the current the bright glow is reached (section ***III***), which is the transition to glow discharge. After a discontinuous transition from **A** to **C**, the gas enters the *normal glow* region (section ***IV***), in which the voltage is almost independent of the current over several orders of magnitude in the discharge current. The electrode current density is independent of the total current in this regime. This means that the plasma is in contact with only a small part of the cathode surface at low currents. As the current is increased from **C** to **D**, the fraction of the cathode occupied by the plasma increases, until plasma covers the entire cathode surface at point **D**.

In the *abnormal glow* regime above point **D**, the voltage increases significantly with the increasing total current in order to force the cathode current density above its natural value and provide the desired current.

Still further increase in current causes the potential to rise to a maximum (point **E**). If the DC power supply has a sufficiently low internal resistance, the discharge will undergo a glow-to-arc transition. The *arc regime* (section ***VII***) is one where the discharge voltage decreases as the current increases, until large currents are achieved at point **F**, and after that, the voltage decreases slowly as the current increases.

### 3.2.3 RF discharges

For the purpose of MEMS and microelectronic technology, the glow discharges are always driven by high frequency (at 13.56 MHz) supplies [53]. This configuration allows etching of dielectrics and metals in contrast to standard DC discharges where from physical limits only conducting materials can be etched. The similarity between DC and RF discharges is that RF discharges show the same Paschen's behavior (see Eq.(3.7)) [1].

The simplest RF reactor and the voltage distribution are shown on Figure 3.6. The reactor consists of two electrodes – grounded and powered. The wafer is laid onto the powered one, when etching is performed or onto the grounded electrode for performing deposition. The system is enclosed in a low-pressure gas atmosphere. The powered electrode is capacitively coupled to the RF generator and automatically develops a negative DC bias in respect to the other electrode, i.e. becomes cathode. This DC bias is called *self-bias* ($V_{DC}$). It appears, because the electrons in the generated AC plasma arc are more mobile than the ions and they charge up the capacitively coupled electrode. Therefore, the electrode surface retains a negative DC bias, since no charge can be transferred across the capacitor (Figure 3.6). The negative charging creates an electric sheath in front of any surface immersed in the plasma, counteracting any further negative charging. Like in the case of DC glow discharge, this sheath also forms a narrow region between the conductive glow region and the powered electrode where most of the voltage drops (Crookes dark space). The magnitude of the self-bias voltage depends on the amplitude of the applied RF signal [13].

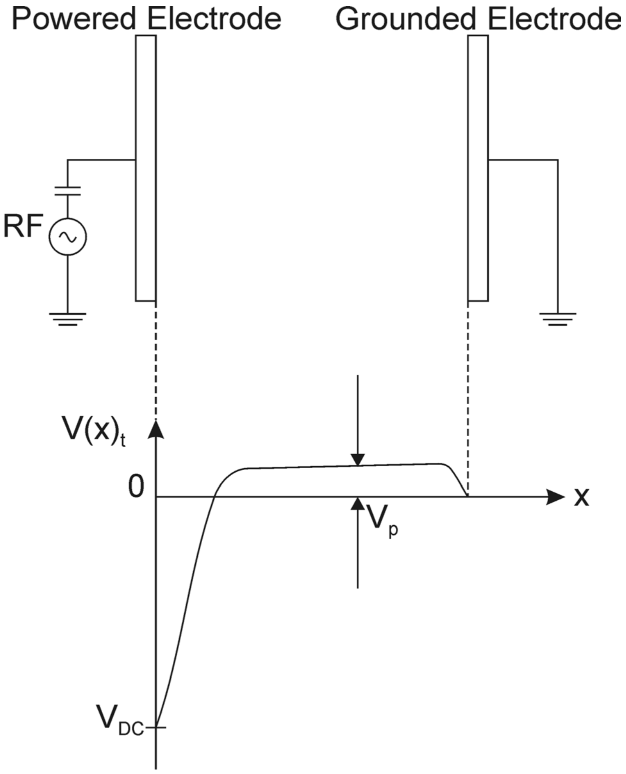

Figure 3.6. Approximate time averaged potential distribution for a capacitively coupled RF discharge.

The energy of charged particles bombarding the surface in glow discharge is determined by three different potentials established in the reaction chamber: the plasma potential, $V_P$, the self-bias potential, $V_{DC}$, and the voltage of the capacitively coupled electrode $V_{RF}$.

The cathode potential (Figure 3.7) follows the sinusoidal form, and is displaced to a negative value called *DC offset voltage* ($V_{DC}$ in Fig. 3.7). The time average of the plasma potential, depends approximately on the DC cathode potential, and the half of the peak-to-peak RF voltage ($V_{RF0}$), applied to the cathode. They are approximately related as:

$$2V_P \propto V_{RF_0} - |V_{DC}|. \tag{3.8}$$

If the potential difference between the discharge and the self-biased electrode is sufficiently large, ions will be accelerated strongly enough towards the cathode to cause sputtering there.

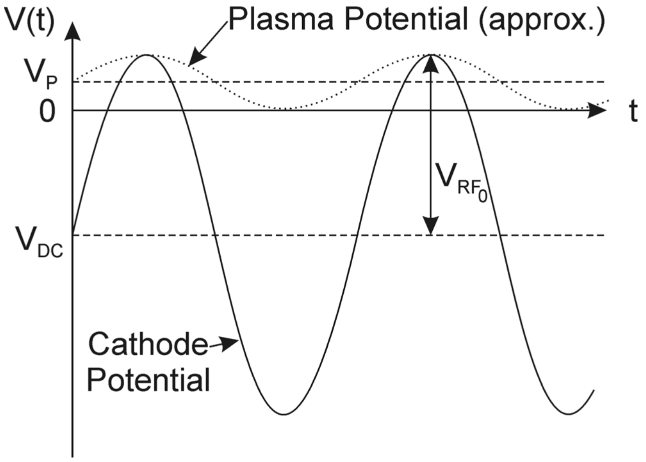

Figure 3.7. Voltage – time dependence in RF system.

Since a RF signal is applied, the sputter effect can occur at any surface in the chamber. The sheath voltages to either electrodes are equal, since these are the only DC voltages in the system and must be equal and opposite. If the target is a conductor, the self-bias voltage could be grounded from the RF generator. Therefore, an asymmetry must be created and one can fulfill this requirement by adding a *capacitor* (Figure 3.6). In these conditions, the sheath voltage $V_1$ to the cathode become large and the opposite sheath $V_2$ will be small. The physical explanation of these sheaths is given by Koenig and Maisel [59]. They started with the assumption for space-charge-limited current. The positive ions with mass $m_i$ come from the glow space and traverse the dark spaces (with thickness $d$) without making collisions, and the space-charge-limited flux $J_i$ is:

$$J_i = \frac{KV^{3/2}}{m_i^{1/2} d^2}, \tag{3.9}$$

where, $K$ is constant, and $V$ is the voltage drop across the sheath. Therefore, the current density of the positive ions is uniform and is equal at both electrodes, hence with Eq. 3.9 it gives:

$$\frac{V_1^{3/2}}{d_1^2} = \frac{V_2^{3/2}}{d_2^2}. \tag{3.10}$$

Because there is a large voltage drop across the dark space, one can conclude that the dark space is a region of limited conductivity. The electrode dark space plasma can be, therefore presented as a capacitor. The capacitance across a dark space is proportional to the electrode area $A$ and inversely proportional to the dark space thickness, $d$:

$$C \propto \frac{A}{d}. \tag{3.11}$$

The RF voltage will be capacitively divided between the two sheaths:

$$\frac{V_1}{V_2} = \frac{C_2}{C_1}. \tag{3.12}$$

Combining Eqs. 3.11 and 3.12 gives:

$$\frac{V_1}{V_2} = \frac{A_2}{d_2}\frac{d_1}{A_1}. \tag{3.13}$$

After substitution of Eq. 3.13 into Eq. 3.9, the following expression develops:

$$\frac{V_1}{V_2} = \left(\frac{A_2}{A_1}\right)^4, \tag{3.14}$$

where $A_2$ is the anode area and $A_1$ the cathode area.

The result suggests that the larger dark space voltage will develop at the electrode having a smaller area. The fourth power dependence overstates the effect of geometrically asymmetric systems. In common dry etch systems, the larger electrode consist of the entire sputtering chamber, including the wafer holder having a common electrical ground with the RF power supply. The relatively large area causes a small dark space voltage and no or little sputtering occurs at these surfaces. The target is placed to the smaller electrode, developing a large dark space voltage and strong sputtering takes place.

One of the most important parameters determining the discharge conditions is the reactor pressure. When the pressure is lowered, the total ion energy rises because the self-biased voltage and the mean free path of the bombarding ions increases. The maximum energy (time averaged) of ions striking the cathode is:

$$E_{\max}^{cathode} = e\left(\left|V_{DC}\right| + V_P\right). \tag{3.15}$$

Respectively, the maximum energy on the anode is:

$$E_{\max}^{anode} = eV_P. \tag{3.16}$$

Higher ion energies ($V_1$ *large*) result in lower etch selectivity and can cause device damage. For performing an appropriate etching, an effective ionization is required to yield very high quantities of low energy ions and radicals at low pressures. For this purpose, high-density plasmas sources have been developed such as, magnetron etcher, ICP (*Inductive Coupled Plasma*) etcher and ECR (*Electron Cyclotron Resonance*) etcher [1].

## 3.3 Types of dry etching processes

The discharges described in Section 3.2 are the basic techniques involved in dry etching processes. The dry etching is a rather complex process and depending on some basic technological parameters it is possible to distinguish three basic dry etching methods [13]:

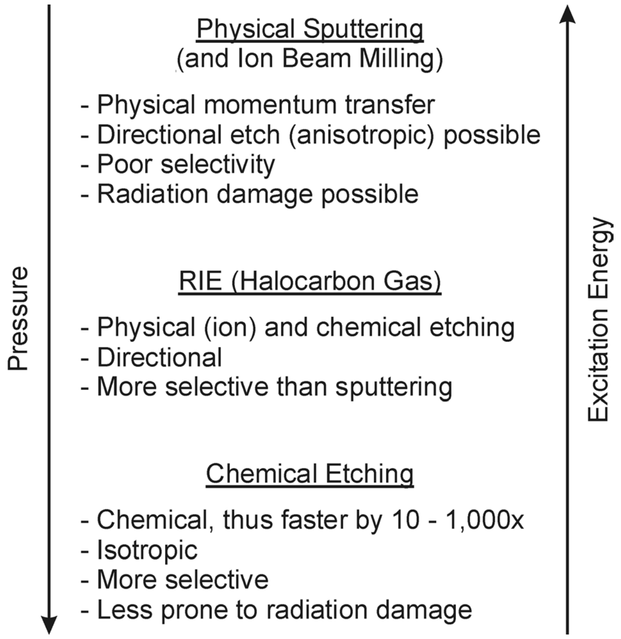

Figure 3.8. The dry etching methods [13].

The first method obeys the pure physical mechanism of *sputtering*. The strongly directional nature of this process allows material from the substrate to be removed in strongly anisotropic manner [60]. However, this kind of material removal is quite non-selective against masking material and material being etched, because the selectivity depends on the sputter yield difference between materials [61]. Another disadvantage is that the ejected species are non-volatile, thus a redeposition and trenching can occur.

Dry etching processes carried out at higher pressures with the presence of reactive gases are classified as *chemical etching*. Using this method, a high selectivity against both mask and underlying substrate layers can be achieved [52]. The etching is 10 to 1,000 times faster than the physical sputtering, but the nature of the process is isotropic. Unfortunately, such process is not adequate for structure formation, when dimensions below 1µm are needed [62].

When a physical component is added to the chemical etching, some of the disadvantages of the previous described methods can be eliminated [63]. Such processes are termed *RIE* (*Reactive Ion Etching*). Combination of physical sputtering and chemical etching offer the possibility of controlling the degree of anisotropy with adequate selectivity [64].

## 3.4 Etching mechanism

The etching mechanism in glow discharges is more complex than that in wet etching. In case of dry etching two types of reactions occur: reactions in the gas phase, so called *homogeneous reactions* and these that occur at the surface, termed *heterogeneous reactions*. Some electrons in the plasma are energetic enough to cause ionization. Collisions of these energetic electrons with neutral etch gas molecules are responsible for the production of reactive species in plasma, called *electron-impact reactions*. These reactive species can also react with themselves and change the overall plasma chemistry. In fact, in plasma, one can consider collisions between species involved. However, some collisions are more important in glow discharge environment, for example collisions involving electrons, which are necessary for understanding the behavior of the glow discharge.

### 3.4.1 Homogeneous reactions

The most important homogeneous reaction is the *ionization*, where the primary electron removes by collision an electron from the atom producing a positive ion and two electrons, which causes the same reaction after acceleration by the electric field:

$$e + A \rightarrow A^{+} + 2e. \tag{3.17}$$

Glow discharge is sustained by this multiplication. There is an energy requirement for ionization to occur. It is equal to the energy to remove the weakliest bound electron from the atom. This threshold energy is known as *ionization potential* [65]. Typically for inert gases the ionization cross-section rises quickly above the threshold to a maximum around 100 eV and drops down at higher energies [66, 67].

Another homogeneous process is *excitation*. Here the energy transfer enables a bounded electron to achieve a higher energy level within the atom:

$$e + A \rightarrow A^{*} + e. \tag{3.18}$$

These excited atoms or molecules are chemically very active and they can be differentiated in view of their lifetime and transfer of the absorbed energy. Here, as in case of ionization, a minimum energy is required for excitation to occur and is termed as *excitation potential*. In fact, the excitation potential is somewhat less than the ionization potential, since excitation raises an electron to higher shell whereas ionization removes the electron from the atom completely.

Some excited atoms have very long lifetimes and they are known as *metastable* excited atoms. When a metastable atom collides with a neutral, the latter can become ionized, if its ionization energy is less than the excitation energy of the excited atom, or the neutral atom can be excited:

$$A^{*} + B \rightarrow B^{+} + A + e, \tag{3.19}$$

$$A^{*} + B \rightarrow B^{*} + A. \tag{3.20}$$

The above processes are known as *Penning processes*: Penning ionization and Penning excitation respectively.

An electron impact with molecule causes *dissociation*:

$$e + A_2 \rightarrow A + A + e. \tag{3.21}$$

A normal result of the dissociation is an enhancement of chemical activity since the products are more reactive than the parent molecule. The dissociation is accompanied by ionization, so called *dissociative ionization*:

$$e + A_2 \rightarrow 2e + A^{+} + A. \tag{3.22}$$

There is a probability that an electron colliding with an atom joins the atom to form a negative ion. This process is called *electron attachment*. The noble gases have full-completed outer electron shell and cannot form negative ions. In contrast to noble gases, halogen gases, which are widely used in dry etching, have an uncompleted outer electron shell. They have high electron affinities and readily form negative ions [68]. This production of negative ions is called *dissociative attachment*:

$$e + A_2 \rightarrow A^+ + A^- + e. \tag{3.23}$$

The dissociation is related to the enhancement of the reactivity of the gases and enables low process temperatures.

### 3.4.2 Heterogeneous reactions

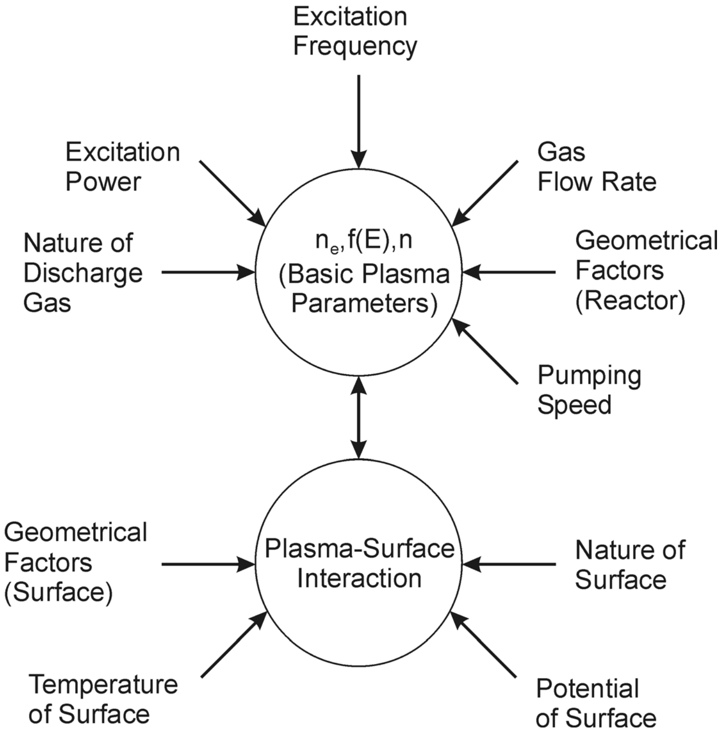

Figure 3.9. Parameters on which depend the heterogeneous reactions. $n_e$ is the electron density in discharge, f (E) is the electron energy distribution function, n is the gas density [13].

The production of species described in previous section occurs exclusively in the plasma. These species cause the chemical reaction onto the surface, resulting in etching. The processes that occur on the surface and the related effects include: a) attaching probabilities of radicals and ions; b) chemical recombination leading to film formation. This film participates in the adsorption of gas species or desorption of species in the gas phase; c) formation of volatile products; d) desorption from the surface; and e) effect of ion and electron fluxes onto the surface. Figure 3.9 shows some of the parameters that impact heterogeneous reactions, such as surface temperature, geometrical aspect of the surface (e.g. the angle of incidence of impinging ions depends whether they strike the bottom, or the sidewall of an etched feature). As it can be seen, for executing a reproducible and useful etch process a large number of parameters must be controlled. The change in any criterion modifies either some basic plasma parameters or more of the surface parameters.

## 3.5 Silicon etching mechanism

### 3.5.1 Plasma etching of silicon with fluorine

In MEMS and IC technology for structuring silicon substrate, utilizing a plasma etching, the most used are fluorine-containing gases [1, 12, 13]. Silicon reacts vigorously with all halogens to form silicon tetrahalides. The reaction with fluorine takes place at room temperature:

$$Si + 2F_2 \rightarrow SiF_4. \tag{3.24}$$

However, silicon etching with fluorine results in rough and pitted surface and thus is not used as feedstock gas in etching process [69].

Using gases such as $SF_6$ or $CF_4$ in the discharge, etching is done by the radical species namely fluorine atoms, created by the dissociation of the gas molecules. A mechanism for the fluorine atom reaction with silicon has been given by Flam et al. (Figure 3.10) [70].

Since fluorine atoms form a stable chemisorbed layer on the surface of silicon, it is assumed that the fluorine atoms can create a periodic array of $SiF_2$ groups on the surface [71]. Each of these groups, bounds to two Si atoms from the bulk crystal. Chemisorbed $SiF_2$ groups may be gasified by the reaction of impinging F atoms, which must penetrate the $SiF_2$ layer to attack the Si-Si bond. The probability $\varepsilon_{F(Si)}$ of impinging fluorine atom to undergo a reaction with silicon may be defined as [70]:

$$\varepsilon_{F(Si)} = \frac{4N_a \rho_{Si} R_{Si}}{M_{Si}\left(\frac{1}{4} n_F v\right)}, \tag{3.25}$$

where $N_a$ is Avogadro's number, $\rho_{Si}$ the density of silicon, $M_{Si}$ the atomic weight of silicon, $n_F$ the gas phase number density of atomic fluorine, $v$ the mean thermal velocity and $\frac{1}{4} n_F v$ the flux of atoms to the surface. $R_{(Si)}$ is the rate with which the fluorine atoms etch silicon in the absence of plasma. It is delivered from the experimental results and can be described by the regression equation [70]:

$$R_{(Si)} = \left(2.91 \pm 0.20 \times 10^{-12}\right) n_F T^{1/2} \exp\left(-\frac{E_{etch}}{k_B T}\right). \tag{3.26}$$

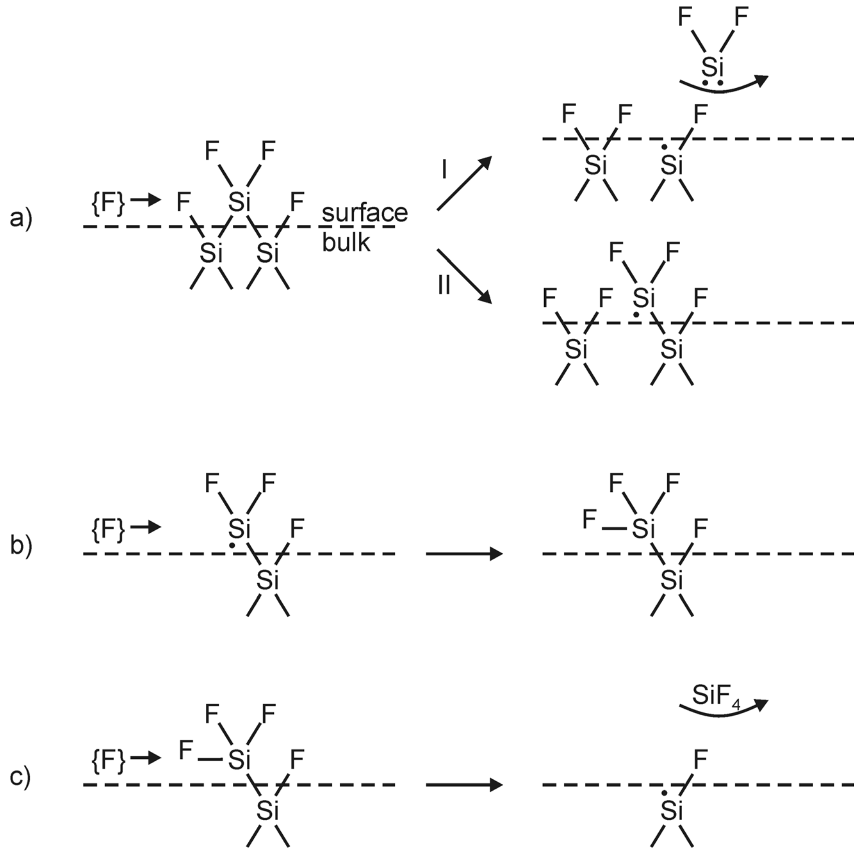

Figure 3.10. Mechanism of fluorine atom reaction with silicon. {F} indicates an incident fluorine atom. a) A two-channel concerted reaction results in direct formation of gaseous $SiF_2$ (I) or (II) bound fluorosilicon radicals b) – c) Further fluorination of bound radicals liberates gaseous $SiF_4$ [70].

Following the results from Coburn [72] and Vasile [73], where the major desorption product was determined to be $SiF_4$, it has been concluded that the etching of single crystal silicon generally proceeds by single reaction branching mechanism (Figure 3.10 a) I and II)). The bond braking occurs, and continues by reducing the number of Si-Si bonds until a volatile $SiF_4$ is formed (Figure 3.10 b) – c)). Silicon tetrafluoride can desorb with minimum energy since no more bonds connect it to the silicon. It can be concluded that the rate limiting reaction is the impinging fluorine atoms with Si-$SiF_2$ bonds on the chemisorbed layer, because the fluorine atom must penetrate the $SiF_2$ layer to attack the Si-Si bond. On the other hand, no direct information about the thickness of the fluorinated layer is given. In this model, the active zone was assumed as monolayer. In fact, the reacting zone may be 3-5 monolayers deep as shown in another recent study [74]. However, the model may apply only for the F/Si system for which it was developed.

There is another model proposed by Winters et al. [63] where it is suggested that etching is analogous to oxide formation on metal surfaces. The main difference is that saturated halides are volatile while oxides are not. The analogy is caused because halogen and oxygen atoms tend to form negative ions at the surface. According to the oxidation model taken from Winters et al., oxidation proceeds by electron tunneling through an oxide film towards the outer chemisorbed layer to form oxygen anions, while metal cations are produced at the metal-oxide interface. The generated strong electric field can pull ions through the film and produce oxide growth, apparently through metal-oxygen ions exchanging positions in the lattice. Exposure of surface to oxygen produces a chemisorbed layer, which changes into an oxide as the surface concentration of the oxygen is increased. Similar reaction sequence would apply to F/Si interaction [63]. In this model, the mass change of silicon film, deposited on a quartz crystal microbalance, as a function of fluorine exposure, was presented as evidence. Initially, this exposure produced a mass increase, which is caused by the creation of a fluoride layer of some equivalent monolayers at the surface. The precise number of these monolayers depends on the number of fluorine atoms associated with etched silicon atoms. A further increase of fluorine dose causes etching by formation of volatile $SiF_4$ resulting in enhanced mass decrease.

### 3.5.2 Silicon etching in fluorocarbon plasmas

As it was described above, the fluorine atoms cause the etching of silicon in a glow discharge generated in fluorocarbon gases. The etching rate depends strongly on the surface coverage $\Theta$ with $SiF_2$. This statement is correct when the fluorine atoms are the most abundant radicals in the gas phase [70]. However, when $CF_x$ and $CF_x^+$ are presented in the gas phase, then these particles are also expected to contribute fluorine to the etching reaction, i.e. the fluorine which leaves the surface as part of an $SiF_4$ etch product [75]. There are experimental data which point out that the etching process of silicon and silicon dioxide in fluorocarbon plasmas proceeds through a thin fluorocarbon layer [76-78]. The etching and the polymer deposition proceed in parallel and thus it is complicate to give an adequate model. Indeed, in plasma environment the surface is bombarded with reactive neutrals and reactive ions with different energies. Inert beams of ions cause only physical sputtering. The removal of material from the substrate in this case increase with increasing ion energy [79, 80]. There is a universal relation between the etching yield, $Y(E)$, and the energy, which applies to all types of ion bombardment induced etch process [79]:

$$Y(E) \approx A\left(\sqrt{E} - \sqrt{E_{th}}\right), \tag{3.27}$$

where $A$ is a constant depending on the particular projectile-target combination, and $E_{th}$ presents the threshold energy for sputtering.

Recently, a detailed model of silicon etching in fluorocarbon plasmas including the effect of fluorocarbon radicals has been developed by Gogolides et al. [75]. They propose that the reaction with fluorocarbon radicals ($CF_x$ ($x = 1 - 3$)) takes place with the following mechanisms:

*Chemisorption of $CF_x$*:

$$Si^* + CF_{x(g)} \rightarrow Si - CF_{y(s)}, \tag{3.28}$$

followed by *carbon sputtering*:

$$Si - CF_{y(s)} \rightarrow CF_{y(g)} + Si^{*}, \tag{3.29}$$

or *recombination of $CF_x$ with F*:

$$\begin{gathered} Si - CF_{y(s)} + F_{(p)} \rightarrow Si^{*} + CF_{y+1(g)}, \\ Si - CF_{y(s)} + F_{(g)} \rightarrow Si^{*} + CF_{y+1(g)}, \end{gathered} \tag{3.30}$$

where $y \leq x$, *s* presents chemisorbed atoms or radicals, *p* stands for physisorbed atoms, *g* stands for gas phase and * denotes a dangling bond or site for chemisorption. Equations 3.28-30 only visualize the possible reactions and they should not be seen as stoichiometric. The reaction of fluorine atoms with silicon follows the model of Flamm et al [70]. Furthermore, they present a surface model for polymer creation and removing, based on following mechanisms:

1) Direct ion deposition instead of sputtering – when $CF_x^+$ ions have energy less than the threshold energy, polymer deposition occurs;

2) Ion-enhanced deposition of sorbed radicals (stitching) – At ion energies less than threshold energy the $CF_x$ radicals are chemisorbed on the silicon surface creating a polymer;

3) Ion-enhanced deposition of sorbed $CF_x$ radicals on the polymer surface at energies less than threshold energy leads to further polymer formation;

4) Ion-enhanced etching of polymer by fluorine atoms or radicals sorbed on the polymer surface.

Following this surface model, it is considered that fluorine atoms, fluorocarbon radicals, and polymer are simultaneously bonded to surface atoms. Surface coverage is related to all these species in the mixed layer. The etching proceeds as long as polymer does not cover the whole mixed layer. The etching yield of silicon is given by sum of three different etching yields:

$$Y_{Si} = Y_S + Y_{CS} + Y_C, \tag{3.31}$$

where $Y_S$, $Y_{CS}$ and $Y_C$ represent the etching yields for physical sputtering, chemical etching supported by physical sputtering, and pure chemical etching respectively. Hence the silicon etching yield can be expressed as follows:

$$Y_{Si} = \sum_i x_i Y(E)_i \left(1 - \Theta_{TOT}\right) + \beta_F \Theta_F + K(T) R_F \left(1 - \Theta_{CF_x} - \Theta_P\right), \tag{3.32}$$

$$\text{if} \quad \Theta_P < 1 \quad \text{and} \quad Y(E)_i > 0,$$

where $x_i$ is the fraction of the total current carried by ion *i*, $\beta$ is ion-enhanced chemical etching coefficient, and $R_F$ presents the ratio of F to ion flux. The term $(1-\Theta_{TOT})$ in Eq. 3.32 denotes the fraction of clean surface where the $\Theta_{TOT}$ presents the total coverage from F ($\Theta_F$), $CF_x$ ($\Theta_{CFx}$) and polymer ($\Theta_p$). In Eq. 3.32, the energy dependence of the etching yield (Eq. 3.25) for ion *i* is included ($Y(E)_i$). The third term indicate the pure chemical etching. The dimensionless coefficient *K(T)* is given by:

$$K(T)=\frac{K_0 \rho N_A}{M}\exp\left(-\frac{E_A}{k_B T}\right), \tag{3.33}$$

where $\rho$ is the material density, $N_A$ Avogadro's number, and $M$ the atomic or molecular weight of material being etched.

It was shown that this model fits quite well the experimental data obtained from other research groups [75].

## 3.6 Silicon dioxide etching mechanism

The etching mechanism of silicon dioxide follows the mechanism of silicon etching, since again the fluorine is the most used component. For etching $SiO_2$ in plasma environment, mainly $CHF_3$, $CF_4$ and $C_2F_6$ gases have been used mixed with argon [77, 81]. These gases predispose the formation of polymer on the silicon dioxide surface. Oehrlein et al. distinguished three regimes during the plasma etching of $SiO_2$ (Figure 3.11) [76]:

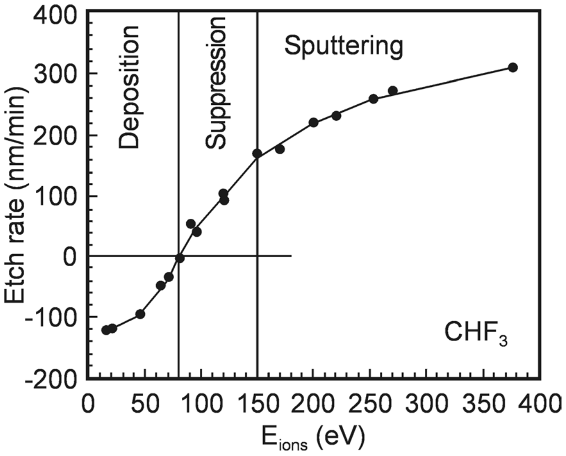

Figure 3.11. Oxide etch rate as a function of the ion energy using $CHF_3$. Three different regimes can be distinguished: the fluorocarbon film deposition, the fluorocarbon film suppression regime for intermediate energies and the sputtering regime.

In the deposition regime, no etching occurs but deposition of polymer. The fluorocarbon film growth rate decreases with the ion energy. In the intermediate regime (Suppression regime) a steady-state polymer film decreases the etch rate from that expected for reactive sputtering process [82, 83]. Once a RF voltage larger than the threshold energy for fluorocarbon film etching is applied, oxide etching will commence. The threshold energy depends on pressure, RF power and gas nature [76]. Although for energies larger than this threshold value, oxide etching takes place, the oxide surface is covered with fluorocarbon film [78]. Because of the presence of this film, the oxide etching yield decreases significantly below the expected one. Therefore, Oehrlein et al. extended the Eq. 3.27 to the form [83]:

$$Y(E)=Af\left[t_{CFx}(E),V_{th}\right]\left(\sqrt{E}-\sqrt{E_{th}}\right). \tag{3.34}$$

$f[\, t_{CFx}(E),\ V_{th}]$ is the function, which describes the effect of a fluorocarbon film with thickness $t_{CFx}$ on the oxide etch yield in the low energy regime. $V_{th}$ is the threshold voltage at which the oxide etching starts.

In the sputtering regime, the oxide etching is described by an energy dependence given by Eq. 3.27. The oxide etching rate scales linearly with the ion current.

Following this assumption Gogolides et al. proposed a surface model for the silicon dioxide etching mechanism [75]. It is presented as non-stoichiometric formulas:

*Physical sputtering*:

$$O_2\text{-}Si^* \rightarrow Si + O_{(g)} + O_2\text{-}Si^*. \tag{3.35}$$

In this stage, the dangling bond is attacked by the ion causing sputtering of silicon and oxygen creating a new dangling bond or site for chemisorption.

Reaction with fluorine atoms:

*Adsorption*:

$$O_2\text{-}Si_{(s)}^* + F_{(p)} \rightarrow O_2\text{-}Si\text{-}F_{2(s)}. \tag{3.36}$$

The fluorine atom is adsorbed at the site for chemisorption. After that, three reactions are possible (occurring at the same time or separately):

*Ion-enhanced chemical etching by F*:

$$O_2\text{-}Si\text{-}F_{2(s)} + 2F_{(p)} \rightarrow Si\text{-}F_{4(g)} + O_{2(g)} + O_2\text{-}Si^*, \tag{3.37}$$

or *ion-enhanced chemical sputtering*:

$$O_2\text{-}Si\text{-}F_{2(s)} \rightarrow Si\text{-}F_{2(g)} + O_{2(g)} + O_2\text{-}Si^*, \tag{3.38}$$

or *chemical etching by F* from the gas phase or physisorbed fluorine:

$$O_2\text{-}Si\text{-}F_{2(s)} + 2F_{(p)}\ (or\ 2F_{(g)}) \rightarrow Si\text{-}F_4 + O_{2(g)}. \tag{3.39}$$

Since the etching is performed in CF-containing gases, the above reactions are supported by reactions with $CF_x$ (x = 1 – 3) or other fluorocarbon radicals:

*Chemisorption*:

$$Si^*\text{-}O_{2(s)} + CF_{x(g)} \rightarrow Si\text{-}O_2\text{-}CF_{x(s)}, \tag{3.40}$$

followed by three possible reactions:

*Ion-enhanced chemical etching by $CF_x$ radicals*:

$$2Si\text{-}O_2\text{-}CF_{x(s)} \rightarrow SiF_{x(g)} + CO_2 + Si\text{-}O_2^*, \tag{3.41}$$

*C sputtering*:

$$Si\text{-}O_2\text{-}CF_{x(s)} \rightarrow Si_{(s)} + 2COF_{x(g)} + Si\text{-}O_2^*, \tag{3.42}$$

*Recombination of $CF_x$ with F*:

$$Si\text{-}O_2\text{-}CF_{x(s)} + F_{(p)}\ (or\ F_{(g)}) \rightarrow Si\text{-}O_2 + CF_{x+1(g)}, \tag{3.43}$$

where *s* presents chemisorbed atoms or radicals, *p* stands for physisorbed atoms, *g* stands for gas phase and * denotes a dangling bond or site for chemisorption. Reaction of polymer creation or loss is the same like in case of silicon etching.

In the current model, the above network is described almost identical to that for silicon. The only difference is that $CF_x$ radicals can also cause ion-enhanced etching of the $SiO_2$ surface. Thus, fluorocarbon radicals can be removed from the surface by reaction 3.41, causing ion-enhanced $SiO_2$ etching, by reaction 3.42 as sputtered carbon, and reaction 3.43 by recombination with F atoms. The silicon dioxide etching yield can be viewed again as a sum of three different etching yields:

$$Y_{SiO2} = Y_S + Y_{CS} + Y_C, \tag{3.44}$$

where $Y_S$, $Y_{CS}$ and $Y_C$ represent the etching yields for physical sputtering, chemical etching supported by physical sputtering, and pure chemical etching respectively. Hence the silicon etching yield can be expressed as follows:

$$Y_{SiO_2} = \sum_i x_i Y(E)_i (1 - \Theta_{TOT}) + \beta_F \Theta_F + \beta_{CFx} \Theta_{CFx} + K(T) R_F (1 - \Theta_{CFx} - \Theta_p), \tag{3.45}$$

$$\text{if} \qquad \Theta_p < 1 \qquad \text{and} \qquad Y(E)_i > 0,$$

where the sum of the second and third term represents the chemical etching supported by physical sputtering in presence of fluorine and fluorocarbon ions.

It is obvious that the etching of silicon dioxide is supported by polymer (fluorocarbon film) deposition. This film affects the etch front of the structure leading to unwanted effects changing completely the desired structure [8]. This makes the controlling of plasma etching process more complicated since changing only one of basic parameters leads to changes in the whole process (Figure 3.9) [13].

## 3.7 The dependence of etching yield on angle of incidence

Although different parameters can affect the performance of the plasma etching process, for the purposes of this work and related to the experimental results, one more important parameter will be discussed. This is the dependence of etching yield on the angle of incidence of incoming ions. Mayer et al. have presented the etching yield Y(Ψ) as a function of angle of incidence Ψ [84]:

$$Y(\Psi) = \frac{ER(\Psi)}{I_b \cos \Psi}, \tag{3.46}$$

where $ER(\Psi)$ is the etching rate and $I_b$ is the beam current density. The effect is observed for physical sputtering where a beam of inert ions is used (Figure 3.12) [85].

Changing the angle from normal incidence to grazeing incidence leads at first to yield increase, and then a maximum is reached at about 60°, after which the yield drops rapidly (Figure 3.12 b)). The increased yield in the range between 0° – 60° is due to the fact that more energy of the projectile is deposited in the near surface region for these angles of incidence. The decrease is because many particles are reflected away from the surface before they have lost much kinetic energy. The etching yield of silicon when using reactive gas ions shows different behavior, having maximum at angle of normal incidence. Moreover, Mayer et al. showed that the angular dependence of etching yield when $SiO_2$ is sputtered with low energy $CF_x^+$ ions, has the same behavior as silicon etched with $Cl^+/Cl_2$ (Figure 3.12 a)) [84].

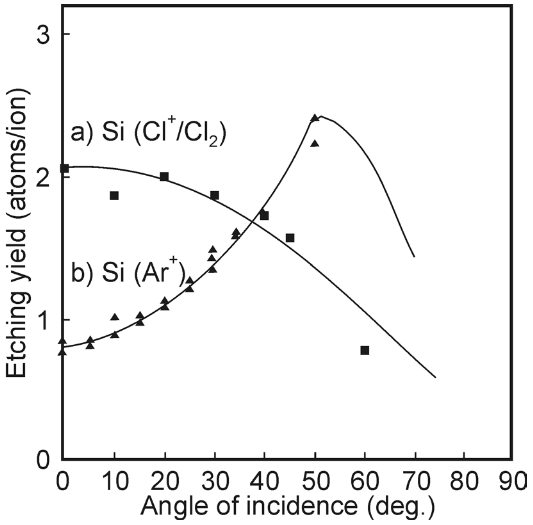

Figure 3.12. Sputtering etching yield as a function of the angle of incidence for a) silicon bombarded with $Cl^+/Cl_2$; b) single crystal silicon etched by $Ar^+$ ion beam at pressure of 0.1 mTorr [85].

Recently, Cho et al. have summarized the experimental results from different groups for angular dependence of $SiO_2$ etching in fluorocarbon plasma. The technological parameters are presented in Table 3 and the results for the etching yield based on these investigations are present in Figure 3.13 a) [86]:

| **Author** | **Process type** | **Gas (ion)** | **Pressure** (mTorr) | **Bias voltage** (V) | **Substrate** |
|---|---|---|---|---|---|
| Hamblen 1 [87] | RIE | $CHF_3$ ($CHF_x^+$) | 10 | 600 | $SiO_2$ (CVD) |
| Hamblen 2 [87] | RIE | $CHF_3$ ($CHF_x^+$) | 10 | 600 | $SiO_2$ (Oxidation) |
| Hedlund 1 [88] | RIE | $CHF_3$ ($CHF_x^+$) | 10 | 500 | $SiO_2$ (Oxidation) |
| Hedlund 2 [88] | RIE | $CHF_3$ ($CHF_x^+$) | 20 | 500 | $SiO_2$ (Oxidation) |
| Schaepkens 1 [89] | HDPE | $CHF_3$ ($CHF_x^+$) | 6 | 100 | $SiO_2$ (Oxidation) |
| Schaepkens 2 [89] | HDPE | $C_3F_6$ ($CF_x^+$) | 6 | 100 | $SiO_2$ (Oxidation) |

Table 3. $SiO_2$ etching processes using fluorocarbon plasma performed by different groups. RIE stands for *Reactive Ion Etching* and HDPE means *High Density Plasma Etching*

In comparison to the results obtained from Mayer et al. for etching silicon with $Cl^+$ and $SiO_2$ with $CF_x^+$ ion beams [85], the etching yield of $SiO_2$ using fluorocarbon gasses exhibit maximum between 45° and 75° (Figure 3.13 a)). The difference was explained in view of the process pressure, since the pressure influence the polymer film deposited on the surface [86]. This polymer film influences the etching rate according to Eq. 3.45. Figure 3.13 b) shows that maximum etching rate occurs at angle of normal incidence. This cosine-like behavior of the etching rate is supposed to be related to chemical sputtering, because it is closely related to the energy deposited on the substrate surface. That is the ion energy, which causes the collision cascade in the region near the impacted location of the surface, moves the target atoms from the original positions, induces chemical reaction and forms the weakly bond species that subsequently desorbs into the gas phase [90].

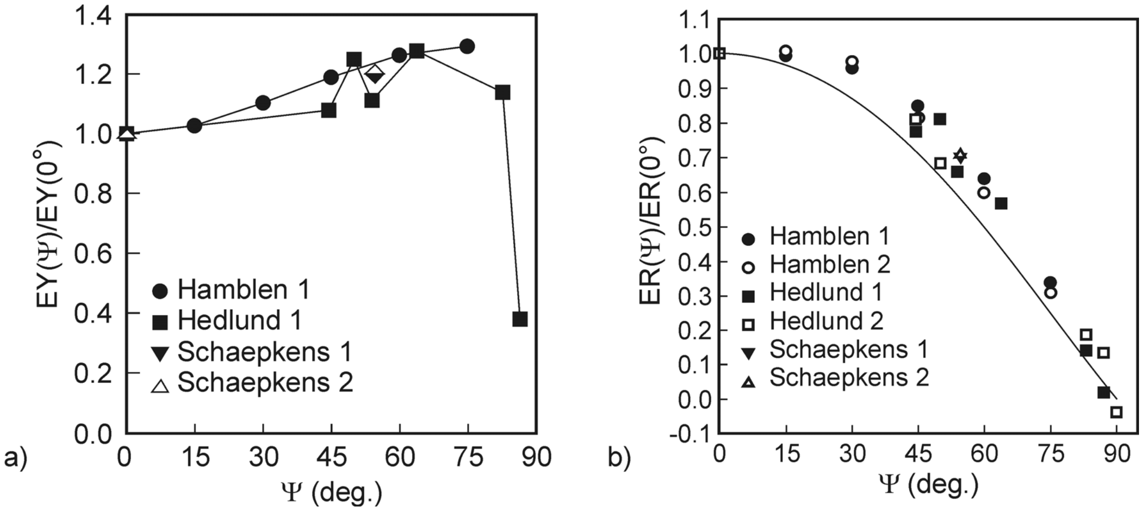

Figure 3.13. a) Angular dependence of the normalized etching yield showing maximum at high angles between 45° and 75°. b) Cosine-like angular dependence of normalized etching rates of $SiO_2$ in various fluorocarbon plasma processes. The results are summarized from different research groups [86].

This behavior of the etching yield adds a thoughtful problem to the treatment of curved and structured surfaces, because etching depends strongly on local surface orientation. However, combining the above explained etching mechanism and the angular dependence of the etch rate opens a new route of structuring and in particular nanostructure formation as will be discussed in the following chapter.

## Chapter 4

# Novel technique for fabrication of sub-100 nm structures

The development of microelectronics and MEMS requires extreme miniaturization of integrated elements. According to the International Technology Roadmap for Semiconductors (*ITRS*), device dimensions below 100 nm can be obtained in the next few years [5]. The most established route to achieve these dimensions is lithography [1]. In this case, lithography with EUV light, electrons or ions have been proposed and used. However, these techniques have met already their challenges in view of mask fabrication, process control and not at last, they are extremely cost-intensive [5]. Furthermore, these techniques are restricted to planar surfaces and therefore are not adequate for fabrication of three-dimensional devices.

Fluorocarbon plasma etching is extensively used for selective etching of contact holes trough $SiO_2$ film, trench capacitors in the modern IC fabrication [82, 83, 89], fabrication of flat panel displays based on *field emission devises* (FED) [91], etc. The precise control of the etch profile in this step is essential, therefore the angular dependence of the etch rate must be taken into account. The investigations related to the angular dependence of the etching rate are mainly directed to solving the problems, which occur during selectively etching of silicon dioxide [84, 86, 89, 92].

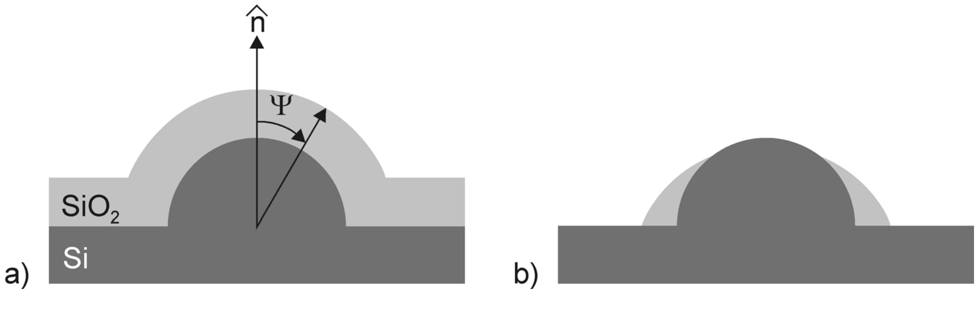

Figure 4.1. Semispherical structure exposed on plasma etching. a) Surfaces with angle $\Psi$ from the normal will be etched slowly due to the angular dependence of etching rate (see Figure 3.13 b) in Section 3.7). b) Resulting structure after completely removing the oxide from surfaces with normal incidence.

On the other hand, when a curved or structured surface is etched the angular dependence of the etching rate is a great advantage. This effect is helpful for preferentially removing of the masking layer from surfaces with normal incidence. For better visualization of the effect, lets assume a semispherical silicon structure covered with silicon dioxide (Figure 4.1 a)). After the preferential plasma etching, the surfaces with normal incidence will be etched faster than those at grazing incidence, $\Psi$ (Figure 4.1 b)). The remaining oxide can be used further as a masking layer for silicon etching.

In this chapter, etching attempts of silicon and silicon dioxide structures exploiting this unique etching behavior will be discussed. As it was discussed in Chapter 3, both a physical and chemical components can impart directionally to the etch process. Controlling the dominant parameters, allows forming structures with nanometer dimensions. The angular dependence of the etching yield during dry etching of silicon dioxide with fluorocarbon containing gases is exploited for obtaining sub-100 nm structures. The choice of process parameters must ensure that with the reactions that take place on the silicon or silicon dioxide surfaces volatile reaction products are produced. Moreover, with correct parameters variegated etch profiles can be realized.

## 4.1 Plasma etching of structured silicon dioxide layer

To demonstrate the unique possibilities for fabrication of sub-100nm structures using plasma etching, lets simplify the complex structure shown in Figure 4.1. This can be done exploiting the etch behavior of silicon in alkaline solutions (0). In this way only two well defined surfaces will be exposed to plasma etching – surfaces with normal incidence and surfaces with angle of 54.7°. Following the explanation in Section 3.7 of Chapter 3, one can expect to etch the inclined surfaces slower than the surfaces with normal incidence due to the cosine law of etch rate (see Eq. 3.46).

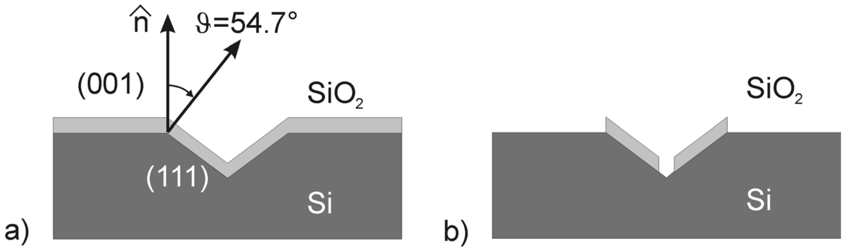

Figure 4.2. Dry etching of curved surfaces. a) Oxidized V-groove in (001) silicon with angle of 54.7° from the normal is created. b) After applying $CHF_3$ plasma etching of $SiO_2$, the silicon dioxide with surface parallel to the incoming ion flux is etched preferentially.

In order to investigate the angular dependence of the etching yield, samples of 16 times 8 $mm^2$ size were made from 3 in. (001) oriented silicon substrates (B doped with 5–10 Ωcm resistivity). After thermal oxidation both rectangular windows with 6 mm times 20 µm dimensions as well as square windows with 20 µm dimension were opened in the 2 µm thick oxide layer by optical lithography and subsequent buffered HF wet etching. V–grooves and inverse pyramidal openings with (111) sidewalls were accomplished by anisotropic wet etching with an aqueous KOH solution (40 wt %, temperature 60 °C) (Figure 4.2 a)). The opening angle of the structures is 70.5°, forming an angle of 54.7° of the sidewalls of the grooves with respect to wafer's normal. Etching was followed by another steam oxidation process to obtain a 300 nm oxide layer on the substrate surface. The oxidized structures were exposed to $CHF_3$ RF plasma (description of the etcher can be found in Appendix A). Silicon dioxide etching was performed at various pressures between 25 – 100 mTorr with 4.5 sccm $CHF_3$ gas flow and led to the particulate removal of the silicon dioxide layer (Figure 4.2 b)). Varying the RF power between 150 and 180 W gave rise to a self-bias voltage of approximately 100 – 250 V.

To reveal the impact of the plasma etching process on the silicon dioxide layer, the V-groove samples were subsequently cleaved, investigating its cross section by scanning electron microscopy (SEM) imaging. Note that all trenches and apertures shown in the following SEM images are slightly distorted owing to the charging of the insulating oxide layer during electron exposure.

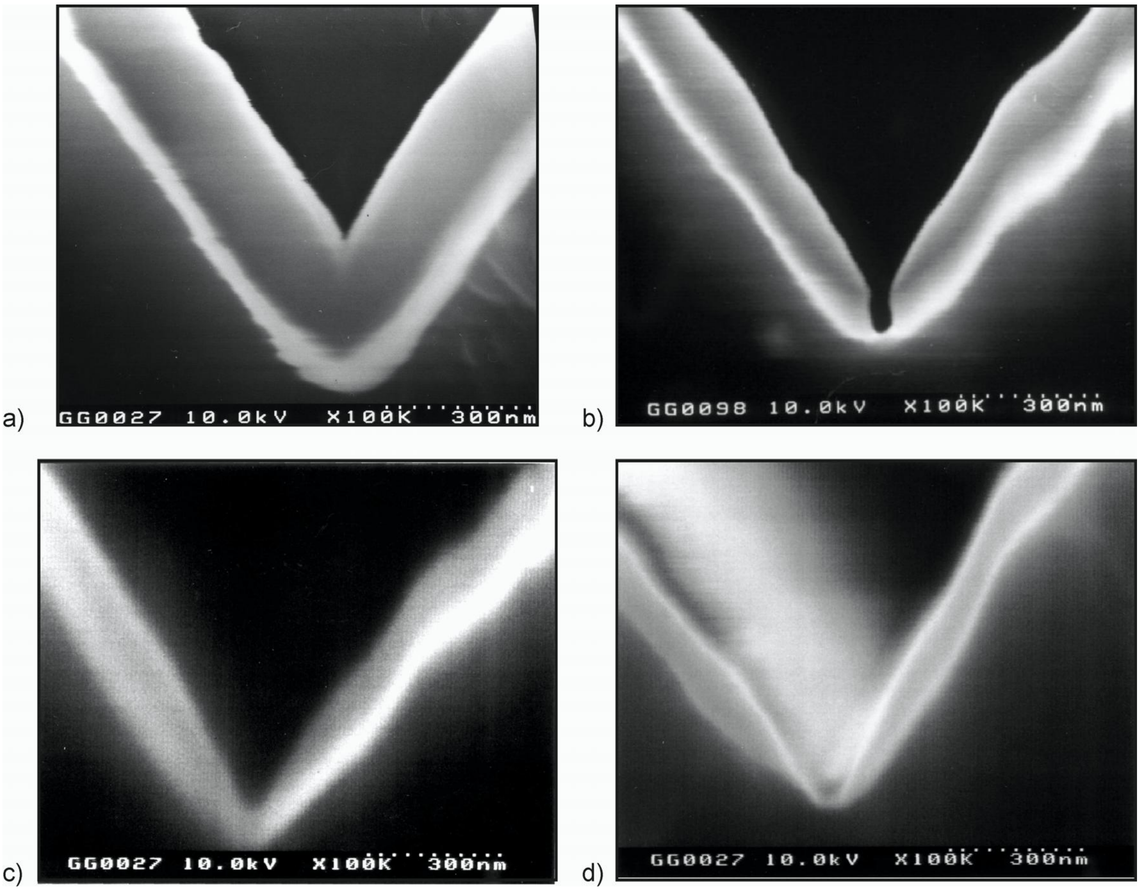

Figure 4.3. SEM images of the cross section of thermally oxidized V-grooves on a (001) oriented silicon substrate before (a) and after RIE plasma etching of the silicon dioxide layer with $CHF_3$ at b) 75 mTorr, c) 25 mTorr, and d) 100 mTorr.

Figure 4.3 shows such images of an oxidized V-groove a) before and b) after reactive ion etching at pressure of 75 mTorr, with RF power of 160 W and the maximum possible self-bias voltage of 250 V. The 240 nm thin silicon dioxide layer (Figure 4.3 a)) of almost homogeneous thickness is selectively opened at the sharp apex

(Figure 4.3 b)) of the V-groove while approx. 150 nm thin oxide layer remains on the sidewalls. The lateral dimension of the trench in the oxide layer is approximately 90 nm.

Pressure and DC bias are important parameters with regard to Table 3 and therefore the experiments were performed at different pressure and applied power. Figure 4.3 shows also images of samples etched at pressure of c) 25 mTorr and d) 100 mTorr. It can be seen that at lower pressure the etching takes place almost homogeneous allover the exposed silicon dioxide surface, since for higher pressure etching occurs at the apex. However, by varying the RF power between 150 W and 180 W and the pressure between 25 mTorr and 100 mTorr it was observed that reproducible trench fabrication was restricted to pressure of 75 mTorr and RF power of around 160 W and a corresponding self-bias voltage larger than 220 V.

The narrow range of process parameters can be explained in view of the $SiO_2$ etching mechanism (Section 3.6). From the applied RF power and the resulting DC bias, it can be concluded that the process takes place solely in the sputtering regime. The presence of the fluorocarbon layer, signed as polymer in model from Gogolides, affects also the etching process, since it appears thin for surfaces with normal incidence, allowing etching of the underlying silicon dioxide. However, for increasing inclination angle of the surface, a thicker fluorocarbon layer was observed, which reduces silicon dioxide etching rate. A steady-state etching regime is reached, when fluorocarbon deposition and fluorocarbon etching are balanced.

In order to understand the nature of deviation of the $SiO_2$ etching mechanism, depending on the pressure and applied power, X-ray photoelectron emission spectroscopy surface analysis was performed on the samples etched at different conditions. It should be mentioned that these spectra are not quantitative but qualitative and they are made after finishing the process. The investigated area is in the range of 1 mm, hence the obtained spectra are from integrated area of flat and inclined surfaces. Figure 4.4 shows the C(1s) photoelectron emission intensity of samples etched at a) – b) different RF power and constant pressure of 75 mTorr and c) – d) different pressure and constant RF power of 160 W and resulting DC bias of 250 V. The C(1s) spectrum is found to consist of four peaks at slightly different binding energies. The different peaks can be attributed to C(1s) photoelectrons originating from carbon atoms only bonded to other carbon atoms (C-C bonds) and carbon that has bonds with one up to three fluorine atoms (C-F, $C\text{-}F_2$, $C\text{-}F_3$ bonds) [93]. It is concluded that fluorocarbon material is deposited and present on the $SiO_2$ surface during the etching. It has been reported that the thickness of this film is in the range of 5 nm, therefore the spectra occur noisy [76].

The amount of fluorocarbon material on the surface, i.e. the thickness of a steady-state fluorocarbon film, is proportional to the integrated C(1s) intensity. Figure 4.4 a) shows the XPS spectrum obtained from probe etched at low RF power. The spectrum consist of the peaks attributed to the $C\text{-}F_x$ ($x = 1 - 3$) bonds showing the presence of fluorocarbon layer. When the RF power is increased the intensity of $C\text{-}F_x$ ($x=1 - 3$) peaks markedly decreases as shown on Figure 4.4 b). From this it can be concluded that the fluorocarbon film at low RF power is thicker than at high RF power. This can be explained because of lower RF power (Figure 4.4 a)) the energy of the charged particles bombarding the surface is not high enough to remove the co-deposited fluorocarbon layer, hence the etch rate is reduced, according to Eq. 3.44 (Section 3.6). The effect is enhanced by the presence of curved surfaces as seen by Shaepkens [89]. In case of higher RF power (Figure 4.4 b)) the co-deposited fluorocarbon layer almost disappears since the particles have enough energy to remove the passivation and than to attack the $SiO_2$.

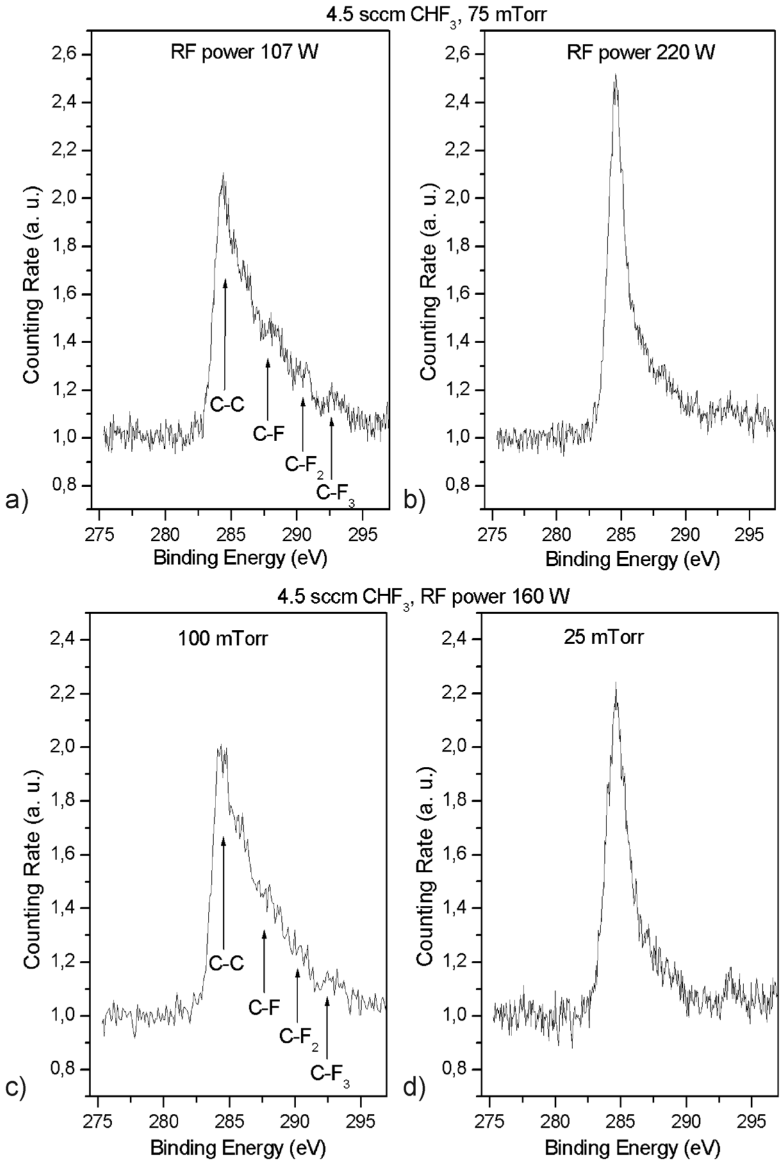

Figure 4.4. C(1s) X-ray photoelectronemission spectroscopy spectra obtained from $SiO_2$ samples etched in $CHF_3$ plasma a) and b) for different RF power (4.5 sccm $CHF_3$ gas flow, pressure 75 mTorr) and c) and d) at various pressure (4.5 sccm $CHF_3$ gas flow, RF power 160 W).

Since the pressure is important parameter in plasma etching, due to Table 3 and the related results, the XPS spectra at different pressures were made (Figure 4.4 c) and d)). At higher pressure the same co-deposited fluorocarbon layer occurs, in spite of applied high RF power, in view of the fact that the C-$F_x$ peaks are presented (Figure 4.4 c)) In this case, the etching rate at the apex is higher than on the sidewalls (Figure 4.3 d)). However, the etched silicon dioxide does not have the well-defined profile as in case of Figure 4.3 b). This can be explained regarding to that the charged particles have sufficient energy to remove the passivating layer even for angle of incidence higher than 0°. Decreasing the pressure, the C-$F_x$ peaks disappear (Figure 4.4 d)), hence the fluorocarbon deposition rate is reduced and the etch rate of the silicon dioxide is almost homogeneous allover the curved surface (Figure 4.3 c)).

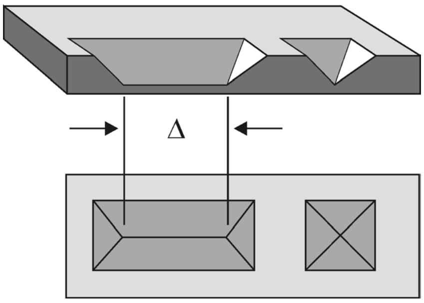

Figure 4.5. Creation of V-groove utilizing wet etching results in formation of bottom edge with length Δ. A square mask patterning results in inverse pyramid, where Δ is 0.

The above discussion is related more or less to V-groove structures resulting in slit like openings with length Δ (Figure 4.5). Further decreasing of the opening dimension is possible if a square mask patterning is used, i.e. inverse pyramid. Applying the same RIE etching process in this case, a small aperture is opened in the silicon dioxide layer at the apex. The small lateral dimension of the inverse pyramid obviates cross sectioning of the aperture by cleavage.

Therefore, Figure 4.6 shows four consecutive head on SEM images of the same sample that was plasma etched for 90 s, 150 s, 210 s, and 270 s applying RF power of 160 W with resultant self-bias voltage of 250 V. An aperture with approx. 70 nm lateral dimension forms in the oxide layer after 210 s while additional etching led to the opening of the edges formed by two adjacent sidewalls of the pyramid starting at its apex.

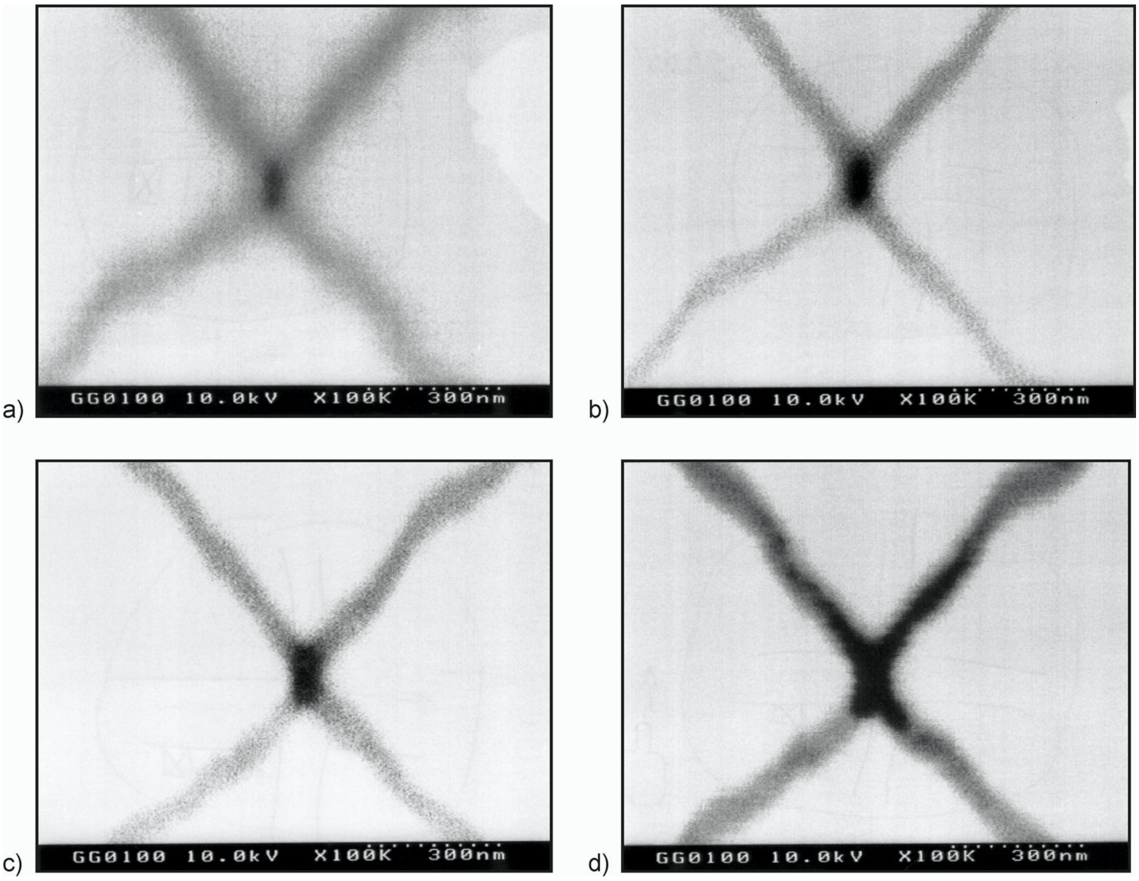

Figure 4.6. SEM head on images of oxidized pyramidal openings in silicon after $CHF_3$ etching of the silicon dioxide layer for a) 90 s, b) 150 s, c) 210 s, and d) 270 s.

### 4.1.1 Sub-100 nm structures obtained by plasma etching

Utilizing the method described in previous section, the etched silicon dioxide layer can be used as a mask for silicon etching. Figure 4.7 shows a structure made in this way. Silicon etching was performed with gas chopping process (the process will be discussed in the next section). Cross sectioning of V-groove structures, reveal high aspect ratio trenches with around 200 nm width (Figure 4.7 a)). The trench width was further reduced by thermal oxidation of silicon entailing a volume expansion by a factor of 2.25 of the oxidized material (Chapter 1). In case of the trench structure shown in Figure 4.7 b) steam oxidation led to reduction of the trench width from 200 nm to 30-40 nm (Figure 4.7 c).

In this way, nanostructures for various applications can be obtained such as microfiltration membranes [94], microsieves [95], optical cavity filters [96], etc.

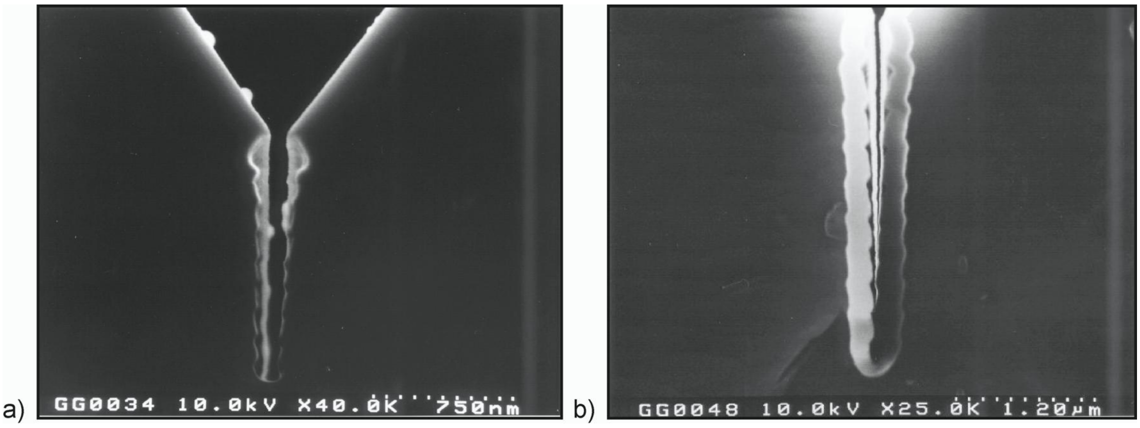

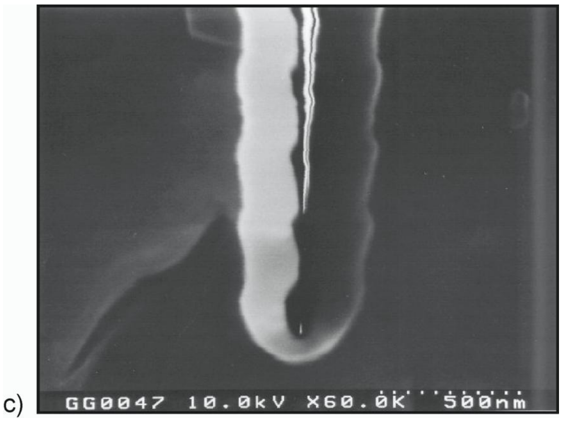

Figure 4.7. SEM image of a 1.8 µm deep trench obtained by ICP etching using the structure from Fig. 4.6 b) as a mask. b) Steam oxidation of the trench in a) allows the precise control of the lateral trench geometry between 0 and 200 nm. c) Zoom view of the structure from b) shows that longer oxidation process will close completely the structure.

Moreover, these structures can be used as a template for deposition. Micromechanical tools such as nanoscalpels for imaging and manipulation of biological structures, probes for *Scanning Probe Microscopy* (*SPM*), mechanical engraving tools require structures with superfine cutting edges or cusps with preferably dimensions about 100 nm [97-100]. At the same time, these structures must consist of as hard as possible and conducting material. The material that fulfils these requirements is diamond. There are different methods for obtaining diamond based mainly on *Chemical Vapor Deposition* (*CVD*), because this method allows homogeneous coating of large surfaces [101]. Different CVD techniques for deposition of diamond are present such as *Microwave Physically Assisted CVD* (*MW PACVD*) *Hot Filament CVD* (*HF CVD*) [102].

To apply the structures from Figure 4.7 a) as a template, HF CVD diamond deposition was performed. For this process, a $H_2$, $CH_4$ gas mixture was used, which was excited by electrically heated (2,000°C – 2,400°C) tungsten wires. In this way radicals are created, which condense on 600°C – 1,000°C heated substrate and polycrystalline diamond film is formed [99]. More detailed information about HF CVD can be found in [103]. Figure 4.8 shows 200 nm bright diamond structures obtained after HF CVD using the already structured silicon as template. In this way small diamond tips or knifes can be fabricated, evidently with high aspect ratio.

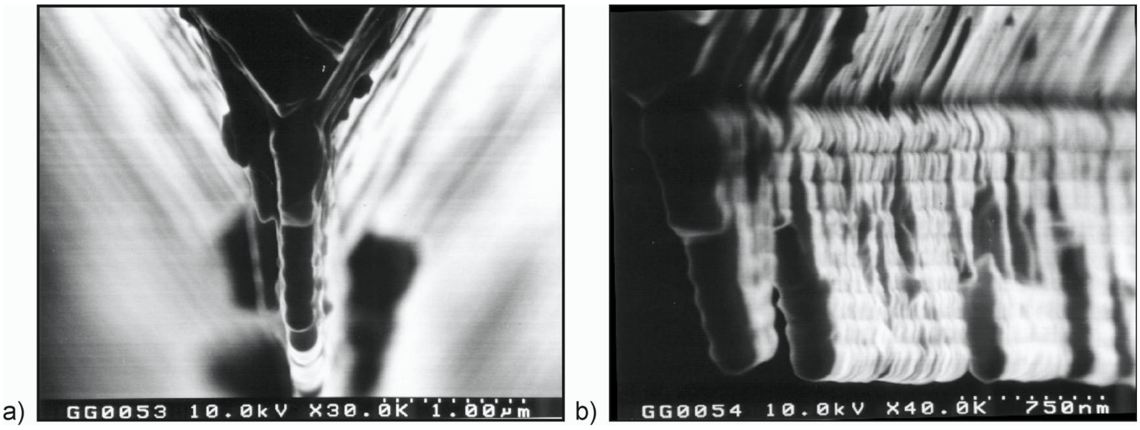

Figure 4.8. A diamond “knife” obtained after hot filament CVD deposition of polycrystalline diamond into the silicon trench and selectively removing of the silicon substrate. a) Cross section of the released diamond structure. b) Tilted view of the structure.

## 4.2 Realization of SNOM calibration standards

Miniaturized apertures in thin films have found multifaceted applications, *e.g.*, a particle size filter, spatial filters in Fourier optics, templates for nanostructures, probe array for Near-Field Optical Memory applications [104], etc. In particular, they proved to be useful as basic structures for the development of advanced probes for various scanning probe microscopy techniques. For example, subwavelength-sized apertures in pointed tips of cantilever probes found widespread application in *Scanning Near-Field Optical Microscopy* (SNOM) [105]. These aperture probes are capable of substantially improving spatial resolution, thus circumventing the well-known diffraction limit of far-field optics. Different techniques have been recently developed for fabrication of such apertures [41, 42, 106, 107].

The basic idea of SNOM lies in overcoming the diffraction limit of resolution (approx. $\lambda/2$) [108]. For this propose, tiny aperture is illuminated from the back and acts as a sub-wavelength sized light source, which is placed in optical near-field distance to a transparent sample, i.e. at a distance $z \ll \lambda$ (Figure 4.9). Obviously, lateral resolution in this case is restricted to aperture size [108]. Imaging is accomplished by scanning the sample. The great technological challenge is the fabrication of such tiny aperture and its characterization.

Mihalcea presents the fabrication process of silicon dioxide aperture tips for first time [41]. It consists of formation of pyramidal shape pits in silicon during the wet etching process (see 0). The sidewalls of these pits are defined by the (111) crystal planes of silicon (Chapter 1) that results in an opening angle of 70.5°. In the next step, these pits are wet oxidized at 900°C. Silicon dioxide growth at these conditions exhibits a complex mechanical stress distribution, in particular at shaped surfaces, owing to its rheological behavior [29].

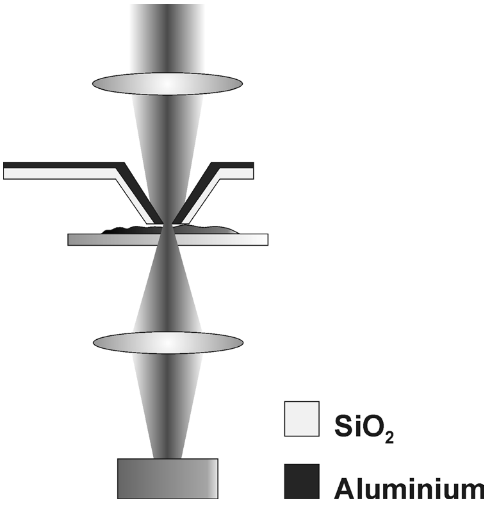

Figure 4.9. Schematic view of SNOM measurement principle. A sub-wavelength illuminated aperture serves as light source. Imaging is performed scanning the sample with respect to the tip position.

The intrinsic compressive stress locally degrades the diffusion rate of the oxidizing species through the already grown oxide layer and furthermore decreases the oxidation rate at the Si – $SiO_2$ interface. Therefore, a reduction of the oxide thickness is observed that depends strongly on the shape of the silicon surface. In case of pyramidal etch pits, a reduced oxide layer thickness occurs at the vicinity of the concave apex. Wet etching of the silicon substrate from the rear side releases the silicon dioxide tip and opens the oxide layer at its weakest point to define apertures of 170 – 190 nm dimensions [109]. Technological improvements and fabrication of aperture probes with size of approximately 100 nm were presented by Vollkopf [42]. It was shown that changing the temperature and oxidation time could result in varying dimensions of the aperture [32]. The above-described methods allow reproducible fabrication of aperture tips, which were successfully integrated in SNOM cantilever probes.

### 4.2.1 Requirements of SNOM calibration standards

The resolution of the SNOM image depends directly on aperture geometry, aperture size and the aperture separation from the sample [108]. Since there are well established techniques for fabrication of SNOM cantilever probes, it is necessary to find a possibility for characterization of the aperture. SEM imaging is often used to determine the aperture geometry [32]. However, the apertures itself consist of silicon dioxide, which is charged during the electron bombardment and with that the quality of the pictures is markedly reduced. It is not possible with this method to characterize the optical properties of the probes. Therefore, a calibration standard for characterizing is needed. However, this standard must fulfill some requirements, which will be discussed in the following.

Calibration is based on scanning of the surface of the standard. For this reason it is important that the aperture probe must approach the surface as easy as possible. An important requirement is that the geometry of the standard aperture must be well defined. Furthermore, all apertures must have exactly the same geometry. With the extensive usage of the standard scratching or impurities can damage its aperture. Therefore, it is necessary to have multitude of apertures in matrix order and very important – topography free. The density of apertures must be as large as possible assembled in useful scanning area for conventional SNOM at about 50 µm onto opaque surface.

Figure 4.10 visualizes the scheme of the first approach for fabrication of this standard using MEMS technique. It was derived from aperture fabrication scheme improved by Vollkopf [42]. It shows a silicon membrane on which pyramidal array is integrated, where each pyramid carries an aperture. These pyramids are metallized to form an optical aperture.

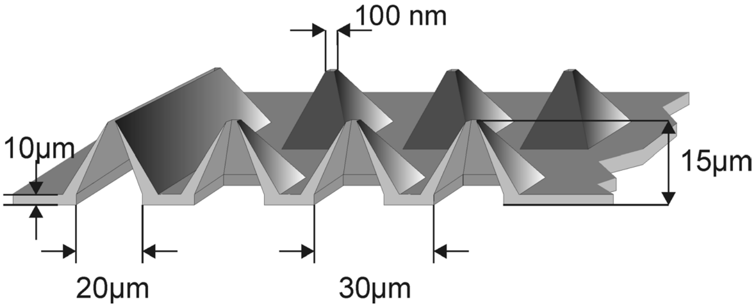

Figure 4.10. Schematic view of calibration standard. The 10 µm thick membrane holds array of hollow pyramidal $SiO_2$ tips. All tips must have an aperture at the apex with dimensions at about 100nm.

In fact, the requirement for easy approach can be fulfilled in case of fiber aperture probes, but when the cantilever probes are used, some technological restrictions occur. Since the technology is based on overcoming these restrictions, brief description of them will be given.

## 4.2.2 Technological restrictions

Figure 4.11 shows the procedure for fabrication of SNOM calibration standards based on self-adjustment technique described by Vollkopf [42]. For this procedure (001) oriented 3” silicon wafer was used. After thermal oxidation 2 µm thick oxide was obtained to serve as a mask for the etching process. The $SiO_2$ was structured using standard photolithography to open a rectangular structure. After wet etching a trough is formed, which defines a membrane with thickness of about 100 µm (Figure 4.11 a)). In the next step, another photolithography process is performed for definition of square openings. The size of these openings is 20 µm and they define the dimensions of the pyramidal openings formed in the next wet etching step (Figure 4.11 b)). After this process, another oxidation step is performed (Figure 4.11 c)). The oxide thickness is about 200 nm that defines the oxide necessary for aperture tip formation. In the last step, the hollow pyramidal tips are released from the bulk by wet etching process (Figure 4.11 d)). As it can be seen, the tips are formed in a 350 µm deep trough, which makes it hard to approach the apertures when the cantilever probe is used (Figure 4.11 e)). Etching the whole wafer from the rear side could overcome this problem, but the membrane thickness is about 10 µm, which makes handling the probes difficult. Increasing the size of the pyramid base will increase the height, but then the aperture density will be decreased. This is visualized in Figure 4.12.

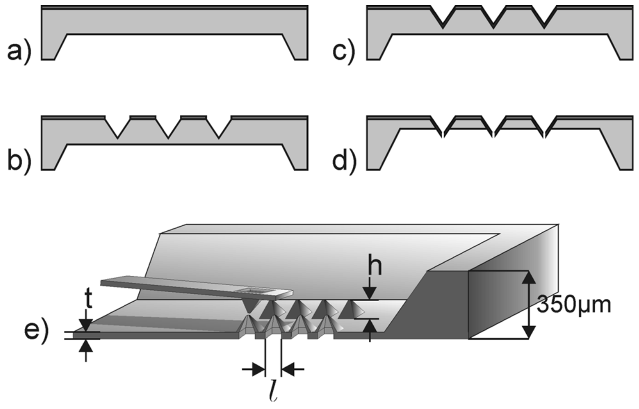

Figure 4.11. Process sequence for fabrication of calibration standard, following Vollkopf [42].

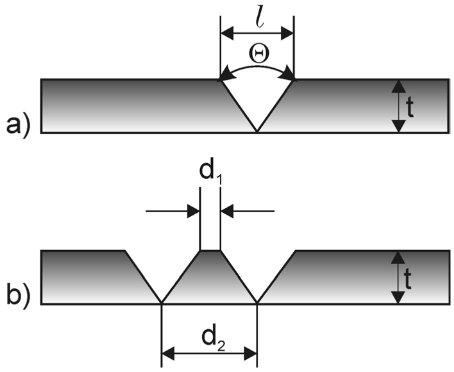

Figure 4.12. Cross section of the geometry of the etch structures in silicon for formation of aperture probes. a) The height h of the pyramid and the membrane thickness t are connected with the width l because of the angle Θ. b) The distance $d_1$ between the neighboring pyramids limits the smallest distance between the apertures $d_2$ in accordance to (Eq. 4.2).

The pyramid height *h* and the membrane thickness *t* are related with the base width *l* through the relation:

$$t = \frac{l}{2\tan(\Theta/2)}, \tag{4.1}$$

where Θ is the opening angle of the pyramid (Θ=70.53°). For fabrication of mechanically stable membrane, it is necessary the thickness t to be at least 15 µm, which results in pyramidal height 15 µm too. This requires a base width of about 20 µm resulting in aperture density of 1 aperture per 625 $\mu m^2$. Moreover, the anisotropic etching requires minimum distance $d_1$ between the neighboring pyramids. Thus, the distance between two apertures is defined by:

$$d_2 = d_1 + 2t\tan(\Theta/2) = d_1 + l, \tag{4.2}$$

resulting in 25 µm for the above given pyramid dimensions.

Since the apertures are formed after releasing the pyramidal tips from the bulk, it is obvious that always topography will occur, hence the requirement for topography free sample cannot be fulfilled. Stopping the wet etching process exactly at the pyramid edge is rather impossible since *Total Thickness Variation* (*TTV*) (see Figure 4.13) of the wafer, which is in the range of 3 µm, is always present.

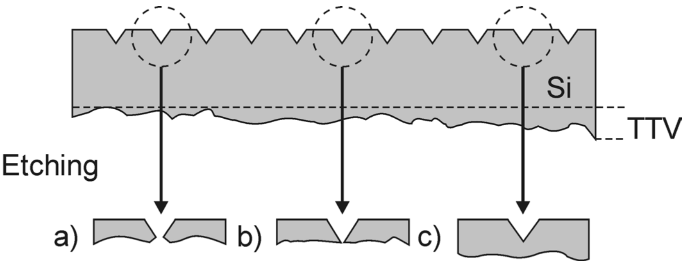

Figure 4.13. Cross-section of (001) Si wafer in which pyramidal structures are etched. The total thickness variation (TTV) is shown as nonplanar surface. After etching the rear side of the wafer, variation of pyramidal opening occurs a) too big, b) optimal opening, and c) not opened pyramid.

### 4.2.3 General scheme for overcoming the technological restrictions

Overcoming the technological restriction for aperture density and membrane thickness is possible if the size of the pyramids is decreased and next if the pyramids formation starts deep into the wafer. This is possible if the fabrication process is performed in two steps (Figure 4.14).

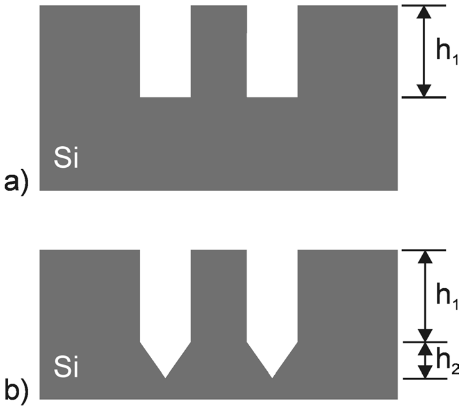

Figure 4.14. Overcoming the technological restriction for membrane mechanical stability. a) anisotropic etching process at depth $h_1$; b) wet etching forms the pyramid with height $h_2$.

The first step requires a deep anisotropic etching through square mask pattern, obtaining a channel of height $h_1$, with perpendicular sidewalls (Figure 4.14 a)). This step defines the initial location where the pyramid will be formed. In this way, the membrane thickness will be defined not only from the pyramid height $h_2$, but also with the depth $h_1$ of the anisotropically etched structure (Figure 4.14 b)).

Figure 4.15 represents the technological chart for fabrication of SNOM calibration standards. After photolithography, square patterns are defined on 2 µm thick silicon dioxide layer (Figure 4.15 a)). This silicon dioxide layer is formed by steam oxidation. For increase of the membrane thickness by $h_1$ (Figure 4.15 b)) a deep anisotropic dry etching (~ 20 µm) was performed. The following step is oxidation for creation of passivation layer (Figure 4.15 c)). The thickness of this layer is ~ 500 nm and it is necessary to protect the sidewalls of the etched structure against the wet etching. For this reason it is necessary to remove the oxide only from the structure’s bottom and this is possible utilizing again the angular dependence of the etching rate. Therefore, plasma etching is applied to remove this oxide from the structure’s bottom (Figure 4.15 d)). In the next step, pyramids are formed by wet etching. Then oxidation step is performed obtaining 150 nm oxide layer (Figure 4.15 e)). For resolving the problem of *TTV*, the technique described in Section 4.1 is applied. Etching 100 nm bright channels with depth of 3 µm overcome the *TTV* (Figure 4.15 f)).

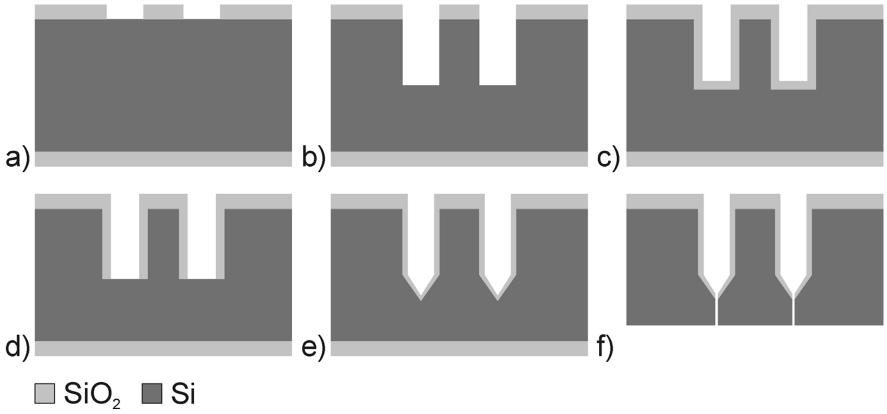

Figure 4.15. Technological chart for fabrication of calibration standard. a) Formation of square patterns on $SiO_2$ layer, b) Deep anisotropic etching, c) Oxidation of the etched structures, d) Removing of the oxide from the bottom e) Wet etching for pyramids formation followed by oxidation, f) Creating channels utilizing the technique described in Section 4.1.

### 4.2.4 Calibration standards fabrication

As it was said for overcoming the restriction of membrane stability two steps are needed. First step is performed through dry etching process. There is a widely used etching method applied for high aspect ratio structures called gas chopping [110]. This method is based on fluorine plasma etching of silicon combined with fluorocarbon plasma process to provide sidewall passivation and improved selectivity to masking materials. Figure 4.16 shows the principle mechanism of the gas chopping.

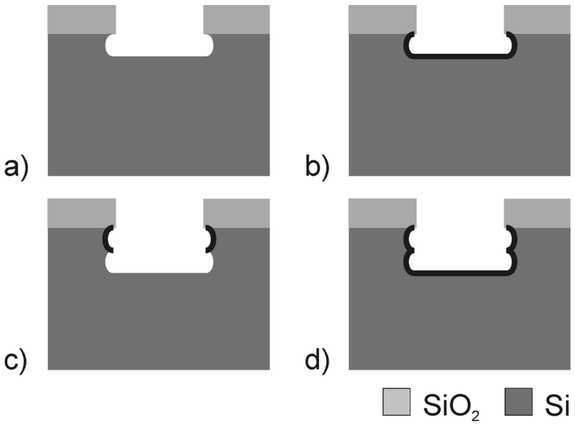

Figure 4.16. Schematic view of the gas chopping process (Bosch process [110]). The process comprises: a) etching of the silicon, b) polymerization, where passivating layer is created, c) removing of the passivation layer from the bottom and further etching of the silicon and d) polymerization and starting with a) again until the desired depth is reached.

The gas chopping consists of etching step followed by polymer deposition. In the etching, the silicon is removed solely isotropic with $SF_6$ and Ar gas mixture for a short time. In the polymerization step the surfaces that were exposed in a preceding step are covered by polymer thereby forming a temporary etch stop layer. The polymer is deposited from $CHF_3$ and $CH_4$ gas mixture at high pressure. The process parameters for both processes are summarized in Table 4 and the ICP etcher is presented in Appendix B.

| | Etching Step | Polymerization |
|---|---|---|
| Pressure | 10 mTorr | 60 mTorr |
| Gases | 35 sccm $SF_6$<br>17 sccm Ar<br>5 sccm $O_2$ | 5 sccm $CH_4$<br>40 sccm $CHF_3$ |
| HF power | 550 W | 550 W |
| DC bias | 90 V | 24 V |
| Forward Power | 10 W | 6 W |
| Step Time | 12 s | 8 s |

Table 4. Gas chopping process parameters.

For creation of 3D structures in silicon, it is necessary to choose suitable process parameters. The selectivity between the masking material and silicon must be high enough whereas the silicon etch rate must be as high as possible. The gas mixture, pressure, the HF power, and temperature directly influence these properties. Here, two examples for the influence of process parameters, having directly effect on the structures shown in Figure 4.14 will be presented. Figure 4.17 shows how the pressure changes the profile of the etched structure.

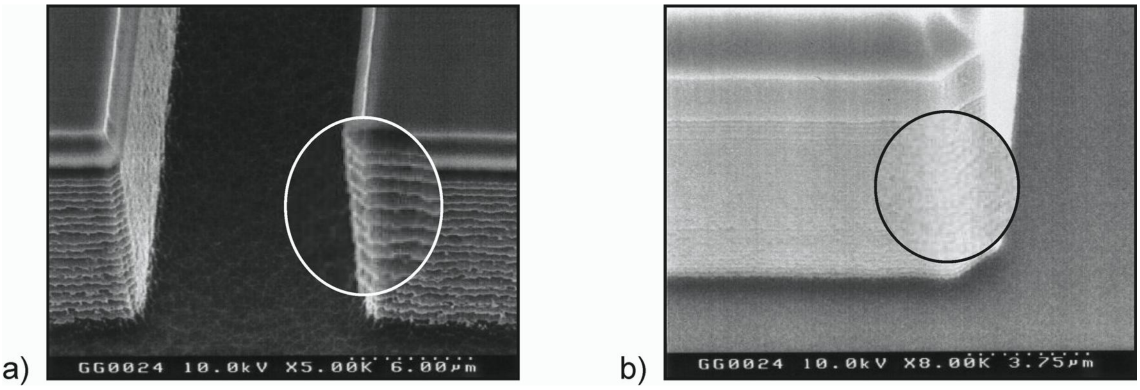

Figure 4.17. Influence of pressure change on the roughening of sidewalls during plasma etching. a) typical sidewall roughness at pressure set to 20 mTorr, b) sidewall roughness decreases after changing the pressure to 10 mTorr.

Figure 4.17 a) presents typical structure profile obtained after gas chopping. Although, the structure has perpendicular profile, the roughness is rather high. This roughness later effects the pyramid formation, since not exact square form will be obtained. The later exert influence on the aperture formation [42]. Decreasing the pressure, in the etching step, lead to smoother sidewalls (Figure 4.17 b)). This can be explained in view that when higher pressure is used, for etching, more active species are involved in the process, which means that etching is dominant against passivation. Decreasing the pressure, affects the balance between etching and passivation.

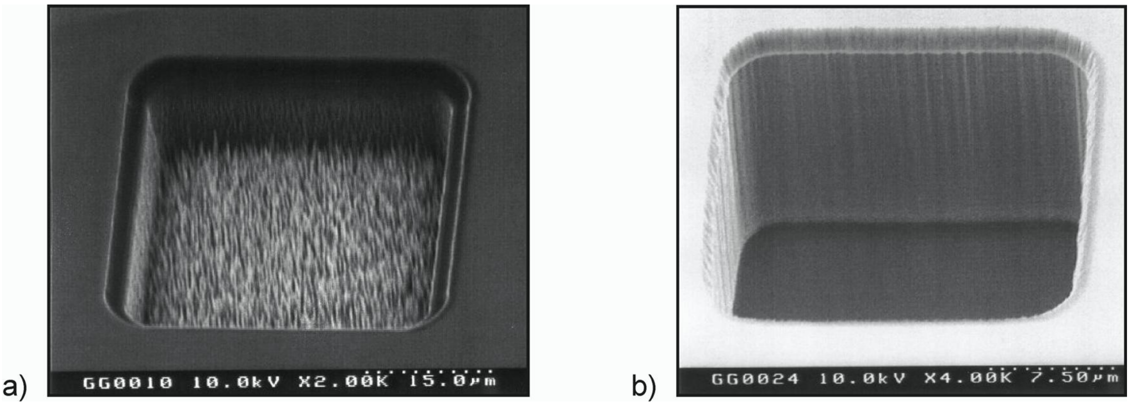

Figure 4.18. Structures obtained after silicon etching using gas chopping. a) through micromasking the bottom of the structure shows a very high roughness, which can make following structuring impossible. b) After addition of oxygen the removal of the polymer is increased as well the redeposition is decreased, hence the micromasking effect is noticeably reduced.

Another parameter, which was taken into account, is the gas mixture. Since in the gas chopping a polymer deposition is involved, often this passivation layer cannot be completely removed from the feature bottom. This leads to formation of so called micromasking (Figure 4.18 a)). Another reason for micromasking is the redeposition of polymer. Changing the gas mixture in the etching step reduces or even completely removes this secondary effect (Figure 4.18). In this case, to the standard etching gases (Ar and $SF_6$) a small amount of oxygen is added (Table 4). The oxygen enhanced the polymer etching and passivation since the silicon is oxidized [111].

Because the pyramid formation is restricted to wet etching, it is obvious that if this step is directly applied after gas chopping the etchant will attack the sidewalls. Therefore, a passivation (etch stop) layer is needed to protect these sidewalls. There are different methods for creation of etch stop layers [14]. The most widespread methods are high boron doping concentration or oxidation. Since, for creation of an effective etch stop layer in case of boron doping, a very high doping concentration is required, for the aim of this work oxidation is used. In this case, it is necessary selectively to remove the oxide from the structure's bottom. It is possible if dry etching is applied, since the etch yield follows cosine law (Chapter 3). Figure 4.19 shows the SEM images of the structures obtained by the described methods. After thermal oxidation (Figure 4.19 a), dry etching process is led in the RIE etcher with parameters 3.5 sccm $CHF_3$ at 25 mTorr process pressure and 73 W RF power. Owning to the effects described earlier, the oxide is completely removed from the structure's bottom (Figure 4.19 b)). The silicon dioxide remaining on the sidewalls serves as etch stop layer for the following wet etching. After applying wet etching, the desirable structures are obtained (Figure 4.19 c))

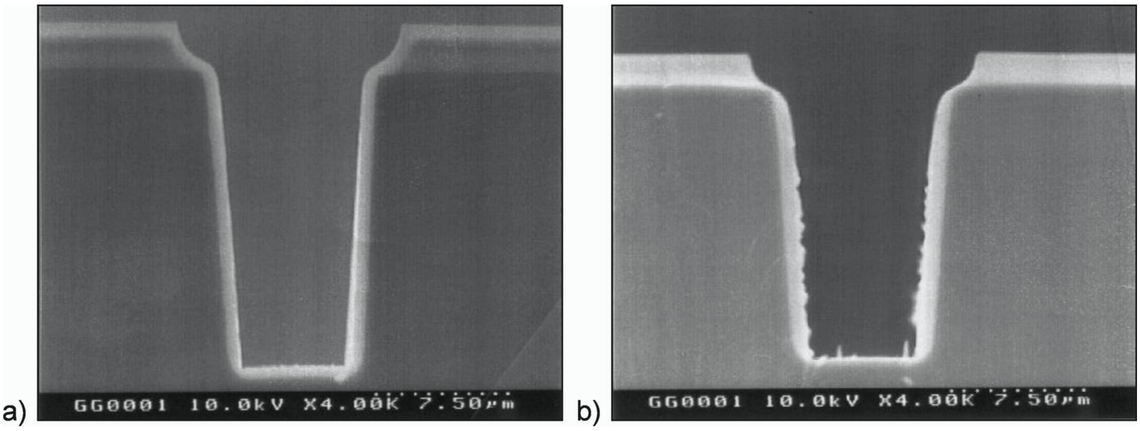

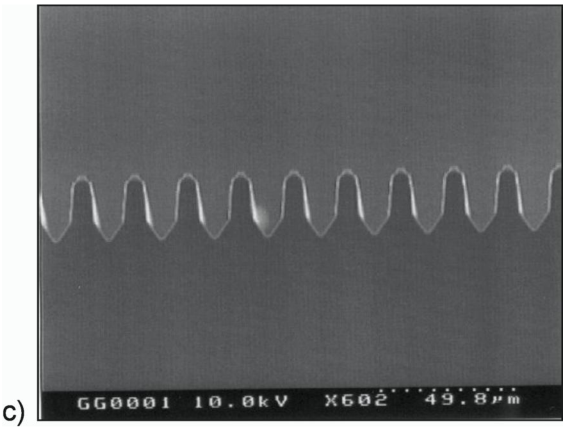

Figure 4.19. a) Profile structures obtained after gas chopping followed by thermal oxidation, b) selective removing of the silicon dioxide at the structure’s bottom, c) formation of V-grooves after silicon wet etching showing the good passivation properties of the remaining silicon dioxide on the side walls.

The same process steps have been applied to the patterns required for SNOM calibration standards and the results are shown in Figure 4.20. It is proved that the oxide is selectively removed only at the bottom (Figure 4.20 b)) allowing followed wet etching (Figure 4.20 c) and d)). In the next step, after thermal oxidation the oxide at the apex is removed and applying again anisotropic plasma etching a channel with depth of 3 µm is drilled. Then the wafer is etched from the rear side until the channels appear on the surface (Figure 4.20 d)).

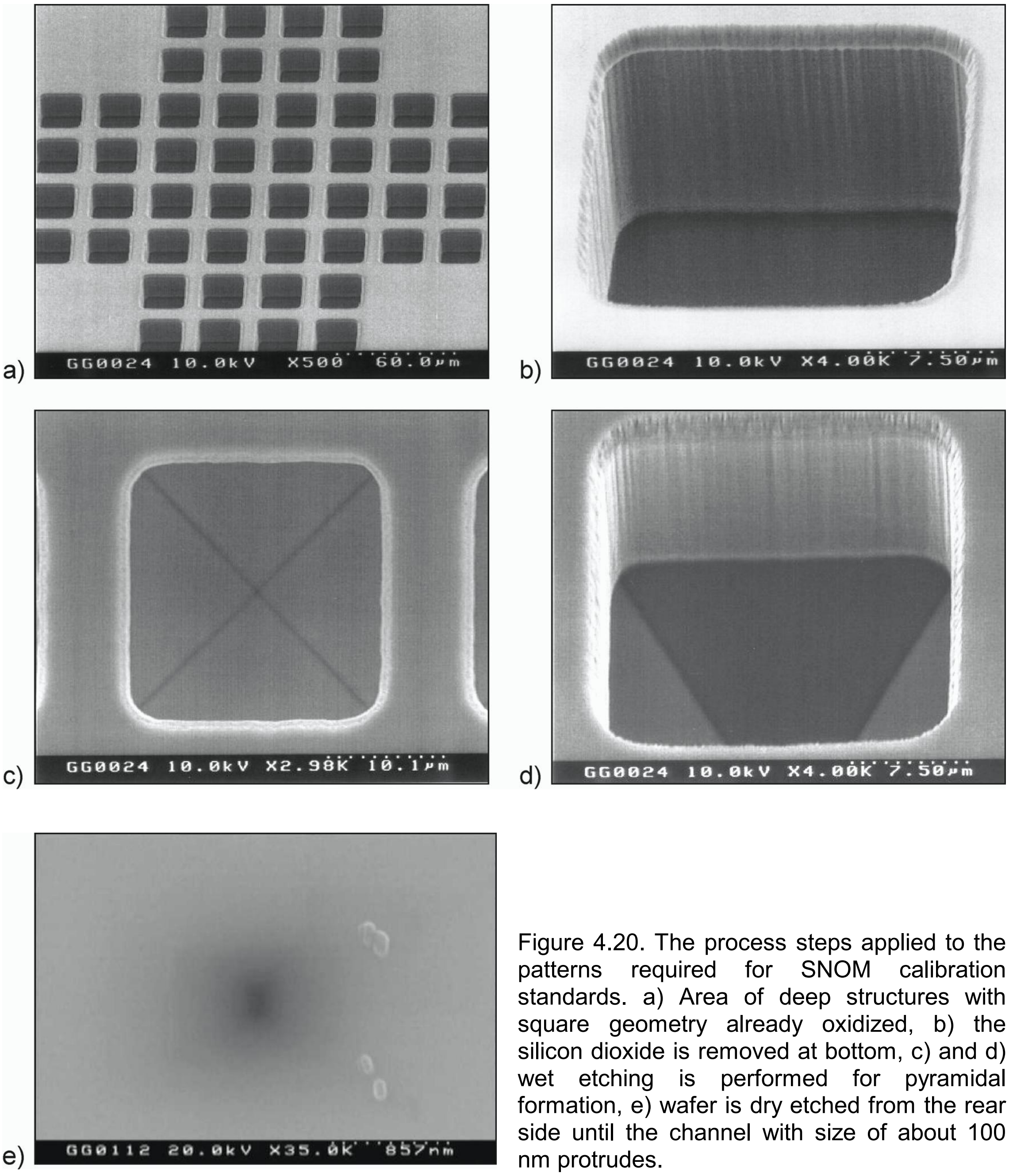

Figure 4.20. The process steps applied to the patterns required for SNOM calibration standards. a) Area of deep structures with square geometry already oxidized, b) the silicon dioxide is removed at bottom, c) and d) wet etching is performed for pyramidal formation, e) wafer is dry etched from the rear side until the channel with size of about 100 nm protrudes.

# Chapter 5

# Lithography-free sub-micrometer structuring

As it was said in the introduction of Chapter 4, lithography is the crucial step in the miniaturization of microelectronics and MEMS components. Recently, different lithography-free techniques have been developed such as imprinting techniques (*Soft Lithography*) [112-114], dewetting process in layered materials [115], self-assembled monolayers [116], etc. The *natural lithography* is relatively simple and inexpensive method for nanofabrication, based on self-assembling [117]. It has been utilized for different applications such as fabrication of lenses for projection lithography [118], texturing a substrate using a self-assembled layer of spheres as deposition mask [119]. The technique described in Chapter 4, is another lithography-free method since the structures are obtained using self-adjusted processes. However, it requires already structured surfaces to obtain nanostructures, i.e. it is necessary to structure the surface and than to obtain nanostructures.

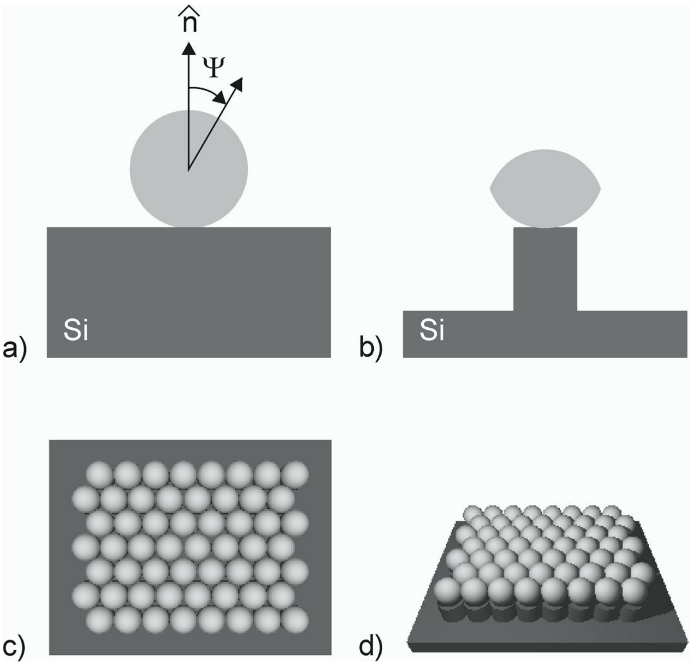

Figure 5.1. Silicon dioxide spheres used as a mask. a) Similar to Figure 4.1 the surface of the oxide sphere with normal incidence will be etched faster. Although Si is etched, $SiO_2$ is also etched, but slower b) resulting structure after completing the etching process, c) Si substrate masked with self-assembled layer of $SiO_2$ spheres, d) plasma etching of the substrate in unmasked areas.

Could it be possible to make nanostructures if the structure is built onto the surface? According to Figure 4.1 and taking into account the cosine dependence of the etching yield, it seems reasonable. For example, a silicon dioxide sphere can be used as a mask, enabling etching of underlying substrate (Figure 5.1 a)). As a sphere is exposed to plasma during the etching of the substrate, this sphere will "shadow" the underlying substrate allowing effective masking (Figure 5.1 b)). The etching yield obeys to cosine law (see Section 3.7), meaning that the surfaces with normal incidence will be etched faster than these at grazing incidence. Taking heed of the above description and applying *natural lithography*, i.e. self-assembly (Figure 5.1 c)), both periodic and non-periodic nanostructures can be integrated into the substrate (Figure 5.1 b) and d)).

In this chapter, sub-micrometer structures will be presented applying dry etching techniques combined with self-assembling technique. The dimensions of the etched structures depend on the sphere size and the process parameters.

## 5.1 Realization of sub-micrometer structures

For obtaining sub-micrometer structures, colloidal silicon dioxide spheres of 500 nm and 1 μm diameter ("SicaStar/Plane Surface" Micromod, Germany) dispersed in water with density of 50 mg/ml were assembled onto the wafer surface resulting in monolayer of spheres with hexagonal periodicity. The particles are assembled by means of surface tension and capillary forces at the meniscus, and therefore the permitted morphology is hexagonal high-density packing, determined by the particles diameter [120]. There are different methods for assembling of particles in 2D array, utilizing capillary immersion forces [121, 122]. Obtaining a monolayer of $SiO_2$ spheres depends on the substrate surface properties. Therefore, before deposition the silicon substrate was cleaned first in RCA mixture $H_2SO_4$:$H_2O_2$ (1:4), followed by treatment for 30 min in $NH_3$:$H_2O_2$:$H_2O$ (1:1:5) solution to obtain hydrophilic surface. Then a drop of $SiO_2$ sphere dispersion was putted onto the silicon surface and dried at room temperature. Figure 5.2 a) shows a monolayer of 500 nm spheres on the silicon surface used as mask. After applying gas chopping etching the resulting structure reveals the expected periodicity of 500 nm (Figure 5.2 b)). Silicon pillars of hexagonal cross section appear under each masking sphere with lateral dimension of only 430 nm and 20 nm wide bridges connecting them (Figure 5.2 c)). In contrast to the circular shadowing geometry of the 500 nm spheres both, the smaller dimension and hexagonal shape, can be explained as follows.

Owing to the divergence of the incoming ions of the plasma and the isotropic character of the etching step in gas chopping process, etching occurs not only at non-masked areas, but also in the shadow of the masking spheres. However, the neighboring spheres have a distinct influence on this process. On one hand side, an additional flux of ions emanates from the reflection at the surface of the six neighboring spheres at certain angles and leads to an increased etching in the shadow. On the other hand, the strong geometrical shielding of the shadowed area by the neighboring spheres outbalances this effect. To proof this, a single sphere of same diameter was used as mask and resulted in a single silicon pillar of now circular cross section with only 250 nm of diameter (Figure 5.3).

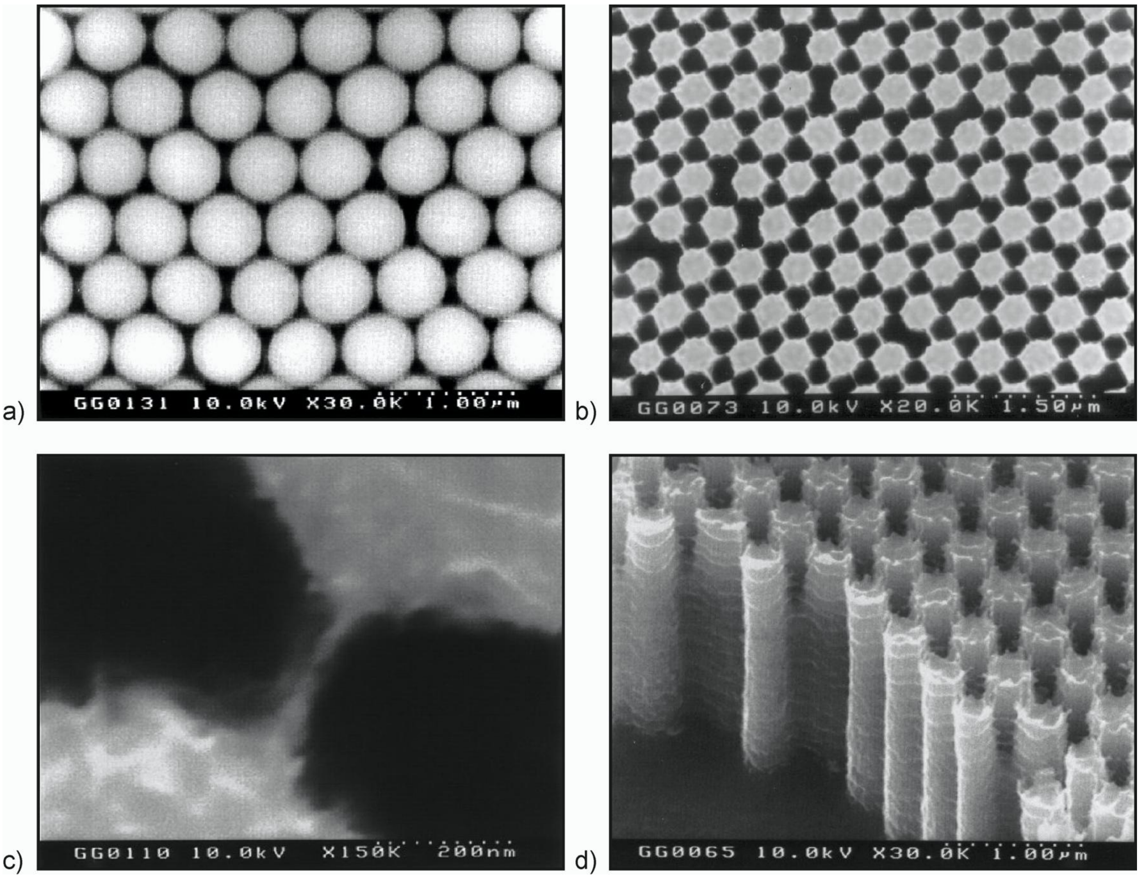

Figure 5.2. a) SEM image of monolayer of 500 nm glass spheres on silicon substrate; b) Top view of the resulting surface structure after applying gas chopping plasma etching reveals silicon pillars of hexagonal cross section; c) Zoom image of b) showing a single 20 nm silicon bridge that connects adjacent pillars; d) Tilted view of the pillars.

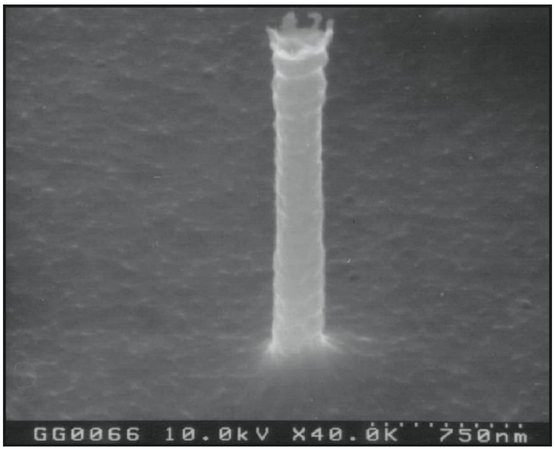

Figure 5.3. SEM image of silicon pillar obtained using a single 500 nm glass sphere as mask. The pillar has circular cross section with dimension of 250 nm in diameter and height of ca. 1.7 μm.

Cross sectioning of the sample in Figure 5.2 reveals high aspect ratio pillars of constant diameter in depth of about 2 μm (Figure 5.2 d)) which is an indication of the excellent etch selectivity between the silicon substrate and the silicon dioxide spheres.

### 5.1.1 Silicon dioxide structures

The structures obtained by the previous described technique can be applied for two-dimensional photonic crystals [123]. For this applications, it is important to control the filling factor of the structure [124, 125]. This can be done exploiting the volume expansion of silicon by factor of 2.25 during thermal oxidation (Chapter 1). Hence, the dimensions of pillars can be either increased by thermal oxidation or decreased by subsequently etching of the formed silicon dioxide. Owing to the optical properties of silicon, applications of these structures are restricted to the infrared range. One way to circumvent the restriction is the usage of the structure as template for other materials with adapted optical properties. In the following, another way to make the structure available for the optical range is presented.

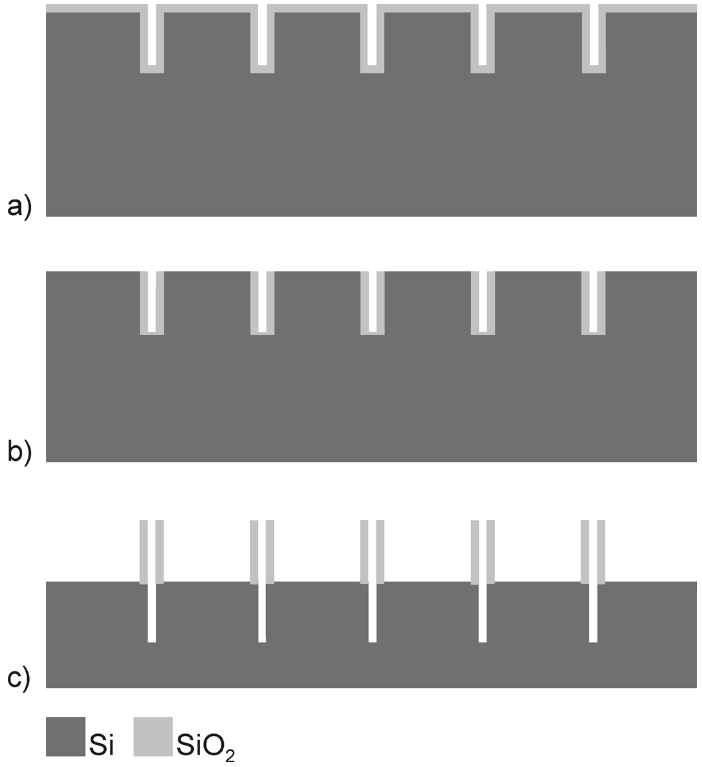

Figure 5.4. a) Silicon structures produced by the process described in Section 5.1 is thermally oxidized, b) $SiO_2$ at the top of the structure is removed selectively by plasma etching, c) selective etching of silicon results in free-standing silicon dioxide structures.

The structured substrate was thermally oxidized to obtain a 200 nm thin silicon dioxide surface layer (Figure 5.4 a)). Subsequently, the sample was exposed to $CHF_3$ plasma to remove selectively silicon dioxide from surface structures with normal orientation with respect to the ion flux of the plasma (Figure 5.4 b)). After this pretreatment, silicon is removed by selective plasma gas chopping using silicon dioxide as masking layer to accomplish a hollow periodic silicon dioxide surface structure (Figure 5.4 c)) Figure 5.5 a) and b) shows structures obtained using this process, with lateral dimensions of 200 nm, which corresponds to the silicon dioxide layer thickness. The latter can be precisely adjusted by the thermal oxidation process. The same process scheme can be applied to single silicon pillar structures (Figure 5.3) to end up with hollow silicon dioxide tubes (Figure 5.5 b)).

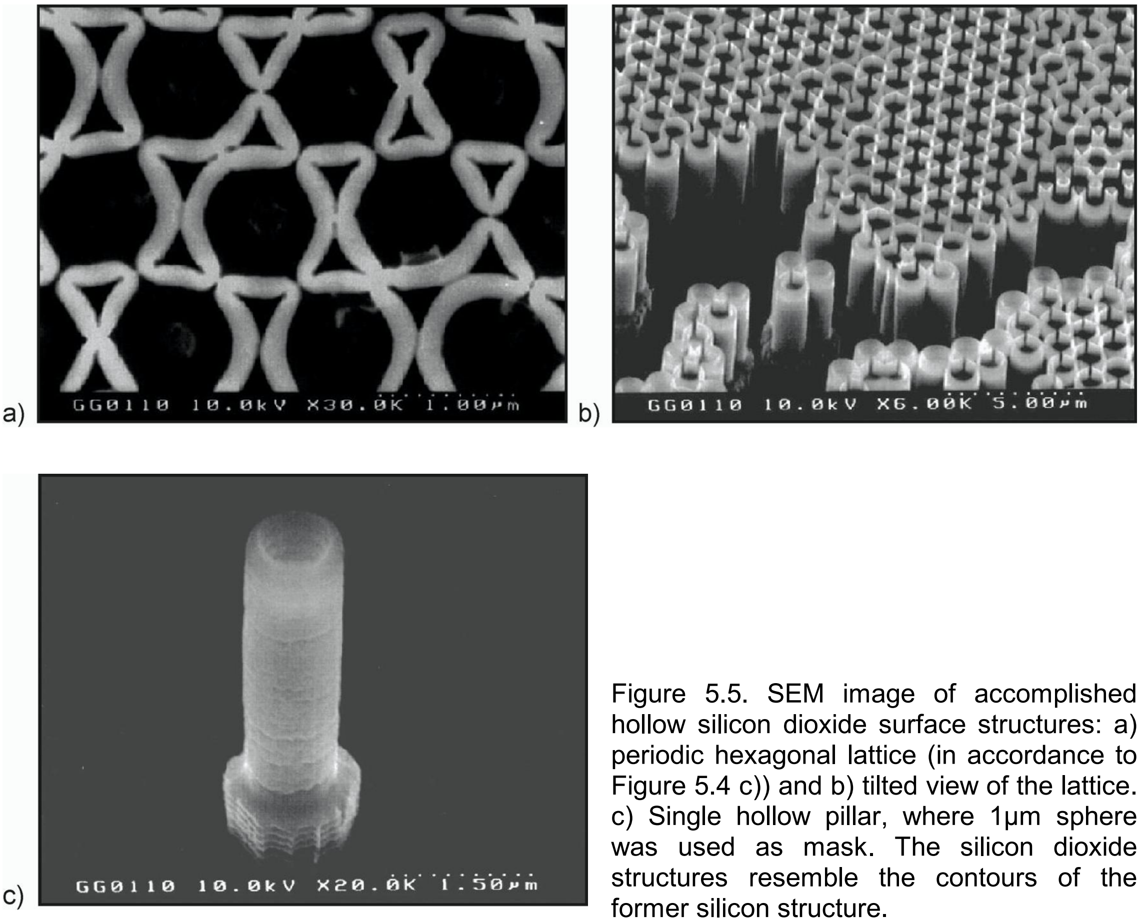

Figure 5.5. SEM image of accomplished hollow silicon dioxide surface structures: a) periodic hexagonal lattice (in accordance to Figure 5.4 c)) and b) tilted view of the lattice. c) Single hollow pillar, where 1μm sphere was used as mask. The silicon dioxide structures resemble the contours of the former silicon structure.

As an addition, the above-described technique opens a new route for lithography-free fabrication of hollow microcylinders, which can be used as a potential applications for integrated optics, optoelectronic device, cooling micro gas/fluid transport, and chemical and biomedical analysis [126-128].

## 5.2 Structuring layered materials

The method described above is suitable for fabrication of 2D photonic crystals. However, establishing 2D photonic crystals requires lateral periodic surface structure combined with a layered material with adapted refractive index profile in the third dimension to form a waveguide [129, 130]. For this reason, the process was extended to layered materials. Prior to the deposition of the masking layer of spheres, the silicon substrate was thermally oxidized to form 2 μm thick silicon dioxide intermediate layer. Applying now $CHF_3$ plasma for silicon dioxide etching, the masking layer of spheres and the plane layer on the substrate are attacked simultaneously. In first approximation, they can be assumed to form a silicon dioxide layer of locally varying effective layer thickness. However, the shape of the spheres has an influence on the etching process because as already mentioned above the etching yield of silicon dioxide in fluorocarbon plasmas depends on the orientation of the surface following a cosine law.

From a simple viewpoint, the spheres keep almost their lateral shape during etching while they are ablated from the top until the etching front reaches approximately the midpoint of the spheres (Figure 5.6 a)). From this point on the lateral dimension start to shrink until the spheres are completely removed. Consequently, etching of the underlying silicon dioxide layer results not in pillar-like structures, but in structures that resemble half spheres or micro lenses (Figure 5.6 b)). Obviously, the same technique can be used to structure layered materials if selective etching processes of the desired stacked materials are available.

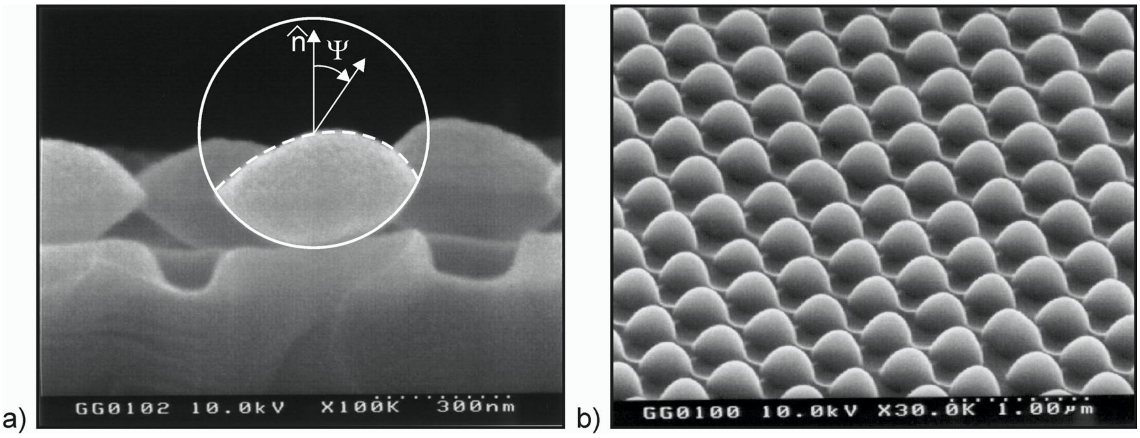

Figure 5.6. Structuring 2 µm $SiO_2$ layer through 500 nm $SiO_2$ spheres. a) Lateral shape of $SiO_2$ sphere before (solid line) and after (dashed line) partial etching, b) $SiO_2$ structure obtained after complete etching of the spheres.

Noticeably, it will be possible to take more information about the etching rate distribution using the silicon dioxide sphere, examining the changes from its initial profile (Figure 5.6 a)). Changing different plasma process parameters will result in different shape of the etched sphere. The results from the observed profile can be used as a feedback for future process simulation, theoretical models, etc.

So far only single layer of spheres were discussed as masking layer. However, the masking effect of two layers of glass spheres on a silicon dioxide intermediate layer on silicon substrate was also studied. As described in crystallography of hexagonal lattices, two layers are stacked in the A B sequence [131]. Each sphere in the first layer (A layer) is surrounded by six neighbor spheres to form six triangular shaped interstitials between them. Three of the latter are closed by spheres of the second layer (B layer) while the other three are kept opened. As was already discussed above, $CHF_3$ plasma etching of silicon dioxide attacks both masking layers of spheres and the plane layer on the substrate. However, the silicon dioxide layer is etched from the beginning through the triangular interstitials of both layers to form triangular shaped openings. At the same time each sphere of the A layer is attacked through the other interstitials in the B layer and is cut into three masking particles that appear after a sufficient etching time as white ellipsoidal features in Figure 5.7 a). For better visualization, white continuous circles in Figure 5.7 a) were added to indicate the shape and position of spheres in the A layer whereas a dashed circle indicates the former position of an already removed sphere in the B layer. Not until the B layer spheres are removed completely, the intermediate silicon dioxide layer is also attacked through the interstitials, which were closed before by B layer spheres, forming again triangular openings but of course with slightly smaller dimension due to the etch lag. During the removal of the ellipsoidal particles of the A layer spheres, an additional opening appears at the interstitial position of these particles (triangle formed by the three continuous circles in Figure 5.7 a)). As a result, quite complex periodic structures are formed in the silicon dioxide layer (Figure 5.7 b)).

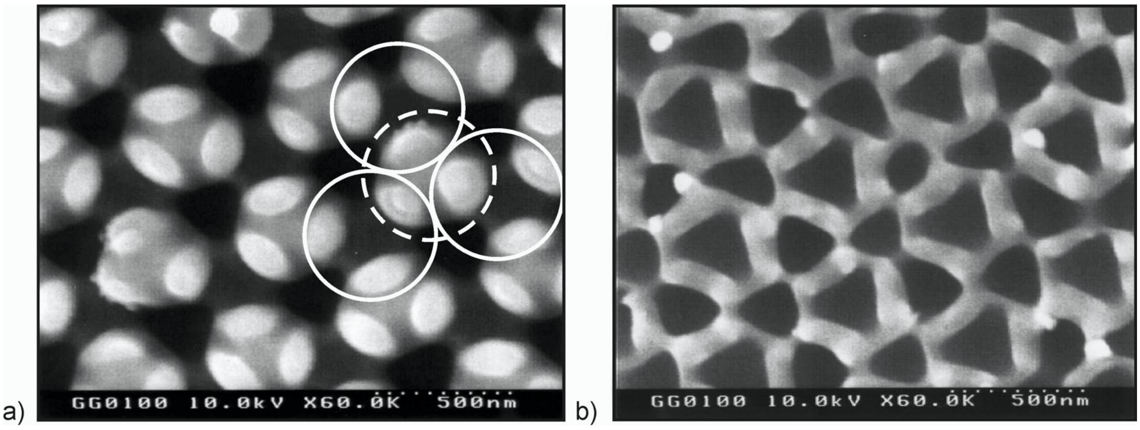

Figure 5.7. SEM image of thermally oxidized substrate masked by double layer of 500 nm spheres after a) partial and b) entire $CHF_3$ plasma removal of the spheres.

# Chapter 6

# Conclusions

The most established route to achieve device dimensions in micro- or nanoscale is lithography, followed by transferring the pattern in the substrate utilizing etching techniques (Top-Down Approach) [1]. However, in this way, lithography has met already its challenges in view of mask fabrication, process control and not at last, it became extremely cost-intensive. Furthermore, this technique is restricted to planar surfaces and therefore is not adequate for fabrication of three-dimensional devices, which is important in ambitious MEMS technology. Therefore, to go on with the scaling down device dimensions, we must look for new technological ways, which must extend the fabrication of 3D MEMS devices to the range of 1 ~ 100 nm. Recently, different lithography-free techniques have been developed such as imprinting techniques (Soft Lithography) [112-114], self-assembled monolayers [116], etc. All of them are based on formation of structure by assembling of small building blocks (Bottom-Up Approach). This “natural lithography” is a relatively simple and inexpensive method for nanofabrication, based on self-assembling and is relevant to build structures onto substrate [117].

The vast knowledge of top-down and bottom-up approaches is the basis for the conventional fabrication processes involved in Micro- and Nanotechnology. The aim of this thesis was to give a part to the bridge between these two technologies by developing of new, lithography-free technique for micro- and nanostructuring. The root to achieve this aim was the idea to combine conventional technological processes with self-adjusting and natural lithography for nanostructures accomplishment, i.e. merging Bottom-Up and Top-Down techniques.

Plasma etching is a widespread technological process in MEMS and IC device fabrication. Structuring the masking layer and the precise control of the etch profile in etching step is essential in the MEMS and IC technology. Great efforts were concentrated on the investigation of the angular dependence of the etching rate, since it is the reason for occurring of secondary effects such as microtrenching, bowing, etc., deteriorating the final shape of the desired structure due to inhomogeneous etching [84, 86, 89, 92]. The results from these investigations showed that the maximum etching rate occurs for surfaces with normal incidence rather than those having grazing incidence. In this work, this undesirable effect was successfully used to develop a unique method to generate extremely small one- and two-dimensional orifices in silicon dioxide layers without any need of a high resolution lithography process. The simplest way to proof the expectations for nanostructuring utilizing the angular dependence of the etching rate during plasma treatment of curved surfaces is using a structure with two well-defined angles. This was achieved by anisotropic etching of (001) oriented silicon, resulting in

V-grooves or pyramids formation with only two well-defined curved surfaces. Thermal oxidation of these structures followed by plasma etching with $CHF_3$ at high RF power in a conventional parallel plate reactor is capable to accomplish self-adjusted orifices of 90 nm dimensions in the oxide layer, which verifies the new concept. Based on existing models of RIE etching of silicon dioxide involving $CHF_3$ as etch gas, it is expected that formation of fluorocarbon layer onto the oxide surface affects and determines the etching rate [75, 89]. Therefore, XPS measurements were made to show the presence of fluorocarbon layer indicating that the thickness of this layer as function of process parameters and surface orientation, markedly affects the etching rate. Additionally, through SEM imaging, the influence of this layer on the final structures was shown. It was presented that the selective etching of silicon through the pierced oxide masking layer enables the formation of silicon trenches of about 200 nm dimensions [132]. Furthermore, it was demonstrated that oxidation of the silicon trenches establishes a simple route to form trenches in silicon dioxide with lateral dimensions between 0-200 nm due to the volume expansion during oxidation.

To demonstrate the potential of this route for nanostructuring a few applications were presented. Structuring diamond and diamond layers is quite hard technological task, since diamond is chemically stable and special expensive equipment is needed. Therefore, the trenches obtained by previous described method were used as a template for CVD diamond deposition. In this way it is possible to obtain 200 nm diamond knives, evidently using conventional lithography and plasma etching techniques.

Another application is the fabrication of SNOM calibration standards. Hereby, utilizing the angular dependence of the etching rate opens the route for fabrication of reproducible, high density, lithography-free small orifices on large membrane surface. Additionally, the etching of silicon dioxide in hollow pyramidal tip improved the reproducibility, concerning the SNOM cantilever probe fabrication.

The technique described by previous procedure, is a lithography-free method since the structures are obtained using self-adjusted processes. However, it requires already structured surfaces to obtain nanostructures, i.e. it is necessary to structure the surface and than to obtain nanostructures by plasma etching. As it was said in the beginning, self-assembly allows building a nanostructure onto substrate. In this work, self-assembled layer of silicon dioxide spheres was used as masking layer and the underlying material was structured with plasma etching. Since the etching rate obeys cosine law, the sphere’s shape is perfect for this application, because it keeps its lateral shadowing shape, while the surfaces with normal incidence will be etched preferentially. In this way, both periodic and non-periodic nanostructures can be integrated into the substrate. Therefore, a new lithography-free technique for nanostructuring is introduced, which is a combination of bottom-up and top-down approaches. This method can be applied to bulk as well as layered materials [133].

In case of bulk silicon a hexagonal surface lattice made of hexagonal shaped pillars of 430 nm dimensions arose using 500 nm glass spheres where each pillar was connected with the neighbor by only 20 nm bridges. However, it is reasonable to have a process, which allows adjusting the dimensions of these structures. Thermal oxidation of the structured silicon samples was suggested a workable tool to vary the filling factor of the surface lattice. Oxidizing theses structures and utilizing anisotropic etching of silicon dioxide with $CHF_3$ plasma followed by selective silicon plasma etching resulted in periodic silicon dioxide surface structures. Furthermore, it was demonstrated that the technique is applicable to layered materials as was shown exemplary in case of structuring planar silicon dioxide layers by means of self-assembled deposition of a single and double layer of glass spheres as masking layer for $CHF_3$ plasma etching.

These methods can be a simple route e.g. to combine photonic crystals with opto-electronic devices, to build up percolation lattices for studying transport phenomena, but also to form optical micro-resonators or micro-antennas if single spheres are used as mask. Other attractive applications are the formation of trench capacitors, optical waveguides in the third dimension, optical apertures for near-field microscopy probes and confocal microscopy, mechanical sieves, etc.

Although this thesis presents the unique possibilities given from plasma etching for nanostructuring, combining self-adjusting and natural lithography, some questions are still open. Therefore, further investigations about the effects that occur in nanostructures during plasma etching must be considered. One of these effects is the local charging, opening the question how it affects the structure formation in nanolevel.

# Appendix A

# Reactors for dry etching

For the aims of this work, two plasma etchers are used. In the following a very brief description of these etchers will be given.

## A.1 Parallel electrode etcher

The etcher used for this work is Oxford, Plasmalab µRIE 80. Minimum process pressure is 5 mTorr. The wafers are placed onto capacitively coupled electrode. The RF generator power output is 300 W at 13.56 MHz.

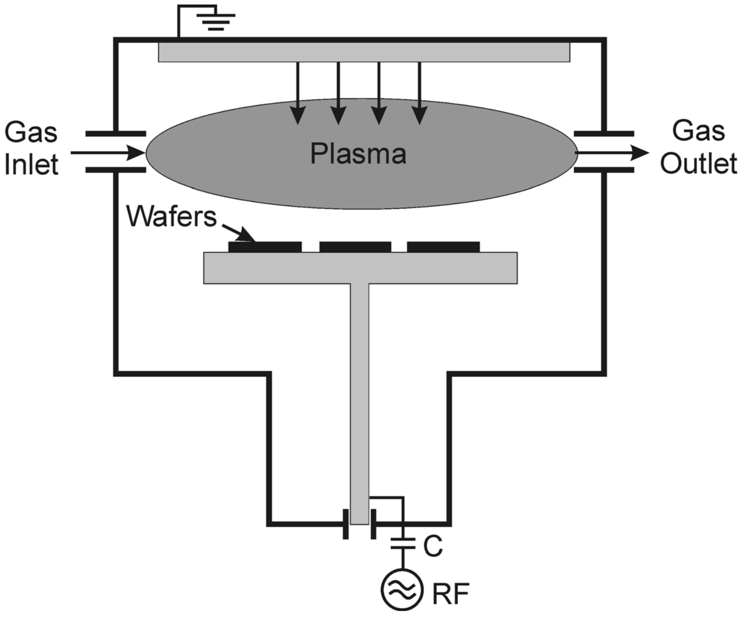

Figure B.1. Parallel electrode type etcher. The wafers are placed on the powered capacitively coupled electrode therefore the system is operated in reactive ion etch mode.

The parallel electrode etcher (Figure B.1) is a vacuum chamber in which between two plane electrodes the discharge is generated in gas mixture. The electrodes are disposed parallel and facing each other. Positive ion sheath surrounds the electrode and the walls in the reactor. The electrode develops a negative self-bias voltage. The electric field due to the negative charge accelerates the positive ions entering the sheath region perpendicular to the target's surface. This leads to directional ion bombardment of the wafer, which results in greater vertical than lateral etch rates. In these conditions, the system is configured in *Reactive Ion Etching* (*RIE*) mode. An intense ion bombardment at the target is achieved by grounding the chamber. In this case, the target area is less than the area of the grounded chamber, so that a large sheath is developed at the target (Eq.3.14), having a value defined by Equation 3.8. For this work, this mode was primarily used for etching of silicon dioxide.

## A.2 ICP etcher

For application in the MEMS technology it is desirable a high-density plasma at lower pressure to be applied. The low pressure prevents ion scattering in the sheath. High density plasma enables the achievement of high etch rate and good control of the critical dimensions and etching profiles. Moreover, high density plasma allows uniform patterning over large diameter substrates. A prerequisite for this are uniform ion and neutral fluxes over the substrate.

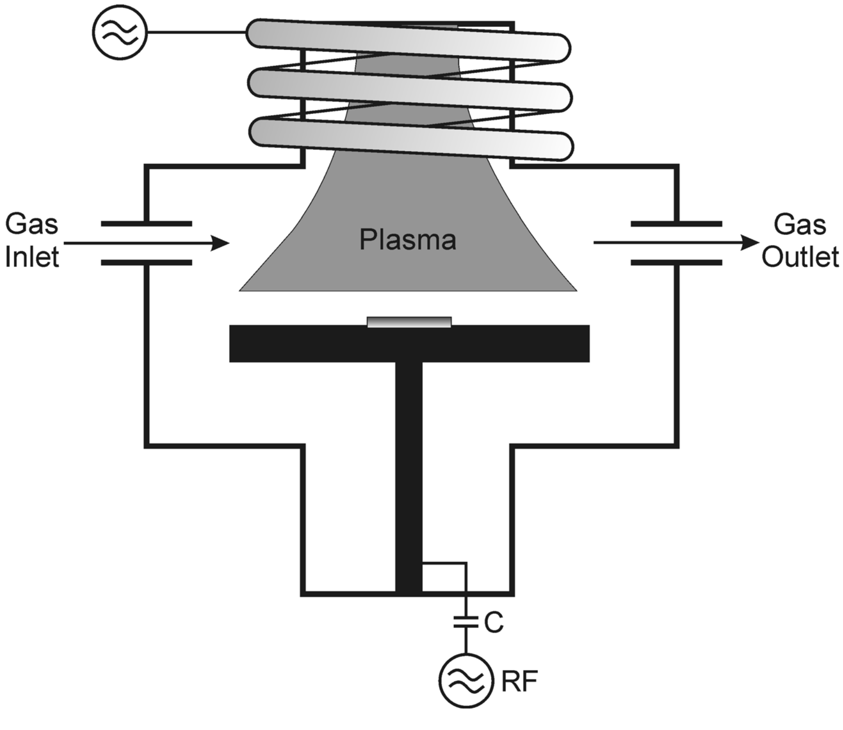

Figure B.2. Schematic design of ICP etcher.

To meet the demand of linewidth control and selectivity it is necessary to control the average ion bombarding energy independently of the ion flux. Instead of capacitive coupled RIE systems, ICP[1] and ECR[2] systems are intensively used [134]. The main advantage of high-density plasmas is the reduction of the possible inter-molecular collisions. As well, the free length of path by low pressure is increased. Since these plasma sources operate in molecular flow pressure regime, the ionic flux can be directed by an electric field with far fewer intermolecular collisions. As a result, the flux of

---

[1] Inductive Coupled Plasma

[2] Electron-Cyclotron-Resonance

etchant species is directed more perpendicularly to the wafer surface. This is useful for creation of high aspect ratio trenches. In these systems, the ion bombarding energy can be separately controlled by placing the wafer on an electrode that is biased with a separate RF capacitively coupled power supply (Figure B.2).

Detailed information about the principles of the described etchers can be found in the technical literature [53, 135, 136].

# References

[1] M. J. Madou, *Fundamentals of Microfabrication*, 1997.

[2] H. I. Smith, M. L. Schattenburg, S. D. Hector, J. Ferrera, E. E. Moon, I. Y. Yang, and M. Burkhardt, "X-ray nanolithography: Extension to the limits of the lithographic process," *Microelectron. Eng.*, vol. 32, pp. 143-158, 1996.

[3] H. Hiroshima, S. Okayama, M. Ogara, M. Komuro, H. Nakazawa, Y. Nakagawa, K. Ohi, and K. Tanaka, "Electron beam writing and direct processing system for nanolithography," *Nucl. Instrum. Methods Phys. Res., Sect. A*, vol. 363, pp. 73-78, 1995.

[4] S. Zissi, A. Bertsch, J.-Y. Jézéquel, S. Corbel, D. J. Lougnot, and J. C. André, "Stereolithography and microtechniques," *Microsys. Technol.*, vol. 2, pp. 97-102, 1996.

[5] http://public.itrs.net, "International Technology Roadmap for Semiconductors," 2004.

[6] G. Timp, *Nanotechnology*. New York: Springer, 1999.

[7] D. Wang and H. Möhwald, "Template-directed colloidal self-assembly – the route to "top-down" nanochemical engineering," *J. Math. Chem.*, vol. 14, pp. 459-468, 2004.

[8] Gottlieb S. Oehrlein and Y. Kurogi, "Sidewall surface chemistry in directional etching processes," *Mater. Sci. Eng., R*, vol. 24, pp. 153-183, 1998.

[9] Christophe Cardinaud, Marie-Claude Peignon, and P.-Y. Tessier, "Plasma etching: principles, mechanisms, application to micro- and nano-technologies," *Appl. Surf. Sci.*, vol. 164, pp. 72-83, 2000.

[10] T. Schwarzl, W. Heiß, G. Kocher-Oberlehner, and G. Springholz, "$CH_4/H_2$ plasma etching of IV-Vi semiconductor nanostructures," *Semicond. Sci. Technol.*, vol. 14, pp. L11-L14, 1999.

[11] S. M. Sze, *Physics of Semiconductor Devices*, Second ed. New York: John Wiley & Sons, 1981.

[12] S. M. Sze, *VLSI Technology*, Second ed. New York, St. Louis, San Francisco: McGraw-Hill, Inc., 1988.

[13] S. Wolf and R. N. Tauber, *Silicon Processing for the VLSI Era*, vol. 1, Second ed. California: Lattice Press, 2000.

[14] S. D. Collins, "Etch Stop Techniques for Micromachining," *J. Electrochem. Soc.*, vol. 144, pp. 2242-2262, 1997.

[15] H. F. Wolf, *Semiconductors*. Toronto: Wiley-Interscience, 1971.

[16] B. K. Vainshtein, *Symmetry of crystals, methods of structural crystallography*. Berlin: Springer, 1981.

[17] I. Brodie and J. J. Muray, *The Physics of Microfabrication*. New York: Plenum Press, 1982.

[18] G. E. McGuire, *Semiconductor Materials and Process Technology Handbook*. New Jersey: Noyes Publications, 1988.

[19] B. E. Deal, "Thermal Oxidation Kinetics of Silicon in Pyrogenic $H_2O$ and 5% $HCl/H_2O$ Mixtures," *J. Electrochem. Soc.*, vol. 125, pp. 576-579, 1978.

[20] B. E. Deal, D. W. Hess, J. D. Plummer, and C. P. Ho, "Kinetics of the Thermal Oxidation of Silicon in $O_2/H_2O$ and $O_2/Cl_2$ Mixtures," *J. Electrochem. Soc.*, vol. 125, pp. 339-346, 1978.

[21] C. R. M. Grovenor, "Microelectronic Materials," 1998, pp. 292-301.

[22] S. K. Ghandhi, "Silicon and Gallium Arsenide," in *VLSI Fabrication Principles*.

[23] B. E. Deal and A. S. Grove, "General Relationship for the thermal oxidation of silicon," *J. Appl. Phys.*, vol. 36, pp. 3770-3778, 1965.

[24] F. J. Norton, *Nature*, vol. 171, pp. 701, 1961.

[25] A. J. Moulson and J. P. Roberts, *Trans. Faraday Soc*, vol. 57, pp. 1208, 1961.

[26] D. H. Kao, J. P. McVittie, W. D. Nix, and C. S. Krishna, "Two-Dimensional Thermal Oxidation of Silicon -- I. Experiments," *IEEE Transactions on Electron Devices*, vol. ED-34, pp. 1008-1017, 1987.

[27] E. A. Lewis and E. A. Irene, "The effect of surface orientation on silicon oxidation kinetics," *J. Electrochem. Soc.*, vol. 134, pp. 2332-2339, 1987.

[28] E. Kobeda and E. A. Irene, "Intrinsic $SiO_2$ film stress measurements on thermally oxidized Si," *J. Vac. Sci. Technol. B*, vol. 5, pp. 15-19, 1987.

[29] D. H. Kao, J. P. McVittie, W. D. Nix, and C. S. Krishna, "Two-Dimensional Thermal Oxidation of Silicon---II. Modeling Stress Effects in Wet Oxides," *IEEE Transactions on Electron Devices*, vol. ED-35, pp. 25-37, 1988.

[30] V. Senez, D. Collard, and B. Baccus, "Analysis and Application of a viscoelastic model for silicon oxidation," *J. Appl. Phys.*, vol. 76, pp. 3285-3296, 1994.

[31] L. M. Landsberger and W. A. Tiller, "Refractive index, relaxation times and the viscoelastic model in dry-grown $SiO_2$ films on Si," *Appl. Phys. Lett.*, vol. 51, pp. 1416-1418, 1987.

[32] A. Vollkopf, O. Rudow, M. Müller-Wiegand, G. Georgiev, and E. Oesterschulze, "Influence of the oxidation temperature on the fabrication process of silicon dioxide aperture tips," *Appl. Phys. A*, vol. 76, pp. 923-926, 2003.

[33] K.-H. Hellwege and O. Madelung, *Numerical Data and Functional Relationships in Science and Technology*, vol. III/17c. Berlin-Heidelberg: Springer-Verlag, 1984.

[34] M. Köhler, *Ätzverfahren für die Mikrotechnik*. Weinheim, 1998.

[35] K. E. Bean, "Anisotropic Etching of Silicon," *IEEE Transactions on Electron Devices*, vol. 25, pp. 1185-1193, 1978.

[36] E. Bassous, "Fabrication of Novel Three-Dimensional Microstructures by the Anisotropic Etching of (100) and (110) Silicon," *IEEE Transactions on Electron Devices*, vol. 25, pp. 1178-1185, 1978.

[37] H. Seidel, L. Csepregi, A. Heuberger, and H. Baumgärtel, "Anisotropic Etching of Crystalline Silicon in Alkaline Solution - Orientation Dependence and

Behaviour of Passivation Layers," *J. Electrochem. Soc.*, vol. 137, pp. 3612-3632, 1990.

[38] E. D. Palik, V. M. Bermudez, and O. J. Glembocki, "Elipsometric Study of Orientation-Dependent Etching of Silicon in Aqueuos KOH," *J. Electrochem. Soc.*, vol. 132, pp. 871, 1985.

[39] H. Seidel, L. Csepregi, A. Heuberger, and H. Baumgärtel, "Anisotropic Etching of Crystalline Silicon in Alkaline Solution - II. Influence of Dopants," *J. Electrochem. Soc.*, vol. 137, pp. 3612-3632, 1990.

[40] M. Elwenspoek, "On the Mechanism of Anisotropic Etching of Silicon," *J. Electrochem. Soc.*, vol. 140, pp. 2075-2080, 1993.

[41] C. Mihalcea, "Mikromechanische Herstellung optischer Nahfeldsensoren für die Rastersondenmikroskopie," 1998.

[42] A. Vollkopf, "Untersuchungen zum Oxidationsverhalten von Silizium - Einfluß auf die Aperturgeometrie von $SiO_2$-Hohlspitzen -," in *Physik*. Kassel: Universität Kassel, 2001, pp. 89.

[43] D. T. J. Hurle, *Handbook of Crystal Growth*, vol. 1. North-Holland: Elsevier, 1993.

[44] J. S. Judge, "A study of the dissolution of $SiO_2$ in Acidic Fluoride Solutions," *J. Electrochem. Soc.*, vol. 118, pp. 1772, 1971.

[45] A. C. Westerheim, A. H. Labun, J. H. Dubash, J. C. Arnold, H. H. Sawin, and V. Yu-Wang, "Substrate bias effects in high-aspect-ratio $SiO_2$ contact etching using an inductively coupled plasma reactor," *J. Vac. Sci. Techonol. A*, vol. 13, pp. 853-858, 1995.

[46] O. Auciello, "Basic phenomena in reactive etching of materials," in *Plasma-Surface Interactions and Processing of Materials*, A. G.-M. O. Auciello, J. A. Valles-Abarca and D. L. Flamm, Ed. Dordrecht / Boston / London: Kluwer Academic Publishers, 1990, pp. 201-249.

[47] A. T. Bell, *Fundamental of Plasma Chemistry in Techniques and Application of Plasma Chemistry*. New York: Wiley Intersciences, 1974.

[48] O. Auciello, A. Gras-Marti, J. A. Valles-Abarca, and D. L. Flamm, "Plasma surface interactions and processing of materials," in *NATO ASI Series*. Dordrecht: Kluwer Academic Publishers, 1990.

[49] John C. Arnold, David C. Gray, and H. H. Sawin, "Influence of reactant transport on fluorine reactive ion etching of deep trenches in silicon," *J. Vac. Sci. Techonol. B*, vol. 11, pp. 2071-2080, 1993.

[50] M. Schaepkens, N. R. Rueger, J. J. Beulens, X. Li, T. E. F. M. Standaert, P. J. Matsuo, and G. S. Oehrlein, "Effect of capacitive coupling on inductively coupled fluorocarbon plasma processing," *J. Vac. Sci. Techonol. A*, vol. 17, pp. 3272-3280, 1999.

[51] M. J. Buie, A. M. Joshi, and J. Regis, "The role of $N_2$ in aspect-ratio-dependent etching of $SiO_2$," *J. Electrochem. Soc.*, vol. 144, pp. 3935-3939, 1997.

[52] R. Hsiao and J. Carr, "Si/$SiO_2$ etching in high density $SF_6$/$CHF_3$/$O_2$ plasma," *Mater. Sci. Eng., B*, vol. 52, pp. 63-77, 1998.

[53] B. Chapman, *Glow Discharge Processes*. New York: John Wiley & Sons, 1980.

[54] F. F. Chen, *Plasma Physics and Controlled Fusion*, vol. 1. New York: Plenum Press, 1984.

[55] A. Ricard, "Basic Physics of Plasmas/Discharges: Production of Active Species," presented at NATO Advanced Study Institute on Plasma-Surface Interactions of Materials, Alicante, Spain, September 4-16, 1988.

[56] K. Nishikawa and M. Wakanati, *Plasma Physics - Basic Theory with Fusion Applications*. New York: Springer-Verlag, 1990.

[57] G. Franz, *Oberflächentechnologie mit Niederdruckplasmen*, Second ed. Berlin Heidelberg: Springer-Verlag, 1994.

[58] G. Francis, "The Glow Discharge at Low Pressure," in *Encyclopedia of Physics*, vol. XXII, *Gas Discharges II*, S. Flügge, Ed. Berlin Göttingen Heidelberg: Springer-Verlag, 1956, pp. 53.

[59] H. R. Koenig and L. I. Maissel, "Application of RF Discharges to Sputtering," *IBM J. Res. Develop.*, vol. 44, pp. 106-110, 2000.

[60] O. Auciello, "Ion interaction with solids: Surface texturing, some bulk effects, and their possible applications," *J. Vac. Sci. Technol.*, vol. 19, pp. 841-867, 1981.

[61] G. Carter, "The physics and application of ion beam erosion," *J. Phys. D: Appl. Phys.*, vol. 34, pp. R1-R22, 2001.

[62] R.E. Hurley and H. S. Gamble, "Some current issues in the use and application of ionised plasma for silicon semiconductor processing research," *Vacuum*, vol. 63, pp. 627-639, 2001.

[63] H. F. Winters, J. W. Coburn, and T. J. Chuang, "Surface processes in plasma-assisted etching environments," *J. Vac. Sci. Techonol. B*, vol. 1, pp. 469-480, 1983.

[64] J. van Zwol, J. van Laar, A. W. Kolfschoten, and J. Dieleman, "Effects of $Ar^+$ angle of incidence on the etching of Si with $Cl_2$ and low-energy $Ar^+$ ions," *J. Vac. Sci. Technol. B*, vol. 5, pp. 1410-1414, 1987.

[65] H. Haken and H. C. Wolf, *The Physics of Atoms and Quanta*, 5th ed. Berlin, Heidelberg: Springer-Verlag, 1996.

[66] D. Rapp and P. Englander-Golden, "Total Cross Section for Ionization and Attachment in Gases by Electron Impact. I. Positive Ionization," *J. Chem. Phys.*, vol. 43, pp. 1464-1479, 1965.

[67] B. L. Schram, F. J. D. Heer, M. J. v. d. Wiel, and J. Kistemaker, "Ionization cross sections for electrons (0.6–20 keV) in noble and diatomic gases," *Physica*, vol. 31, pp. 94-112, 1965.

[68] D. Flamm, "Plasma chemistry in etching," in *Plasma Surface Interactions and Processing of Materials*, vol. 176, *Applied Science*, D. L. Flamm, Ed. Dordrecht: Kluwer Academic Publishers, 1990.

[69] M. Chen, V. J. Minkiewicz, and K. Lee, "Etching silicon with fluorine gas," *J. Electrochem. Soc.*, vol. 121, pp. 1946-1948, 1979.

[70] Daniel L. Flam, Vincent M. Donnelly, and J. A. Mucha, "The reaction of fluorine atoms with silicon," *J. Appl. Phys.*, vol. 52, pp. 3633-3639, 1981.

[71] T. J. Chuang, "Electron Spectroscopy Study of Silicon surfaces exposed to $XeF_2$ and the Chemisorption of $SiF_4$ on Silicon," *J. Appl. Phys.*, vol. 51, pp. 2614-2619, 1980.

[72] J. W. Coburn and H. F. Winters, "Ion- and electron-assisted gas-surface chemistry—An important effect in plasma etching," *J. Appl. Phys.*, vol. 50, pp. 3189-3196, 1979.

[73] M. J. Vasile and F. A. Stevie, "Reaction of atomic fluorine with silicon: The gas phase products," *J. Appl. Phys.*, vol. 53, pp. 3799-3805, 1982.

[74] C. D. Stinespring and A. Freedman, "Studies of atomic and molecular fluorine reactions on silicon surfaces," *Appl. Phys. Lett.*, vol. 48, pp. 718-720, 1986.

[75] Evangelos Gogolides, Philippe Vauvert, George Kokkoris, Guy Turban, and A. G. Boudouvis, "Etching of $SiO_2$ and Si in fluorocarbon plasmas: A detailed surface model accounting for etching and deposition," *J. Appl. Phys.*, vol. 88, pp. 5570-5584, 2000.

[76] G. S. Oehrlein, Y. Zhang, D. Vender, and M. Haverlag, "Fluorocarbon high-density plasmas. I. Fluorocarbon film deposition and etching using CF4 and CHF3," *J. Vac. Sci. Techonol. A*, vol. 12, pp. 323-332, 1994.

[77] M. Schaepkens, T. E. F. M. Standaert, N. R. Rueger, P. G. M. Sebel, G. S. Oehrlein, and J. M. Cook, "Study of the $SiO_2$-to-$Si_3N_4$ etch selectivity mechanism in inductively coupled fluorocarbon plasma and a comparison with the $SiO_2$-to-Si mechanism," *J. Vac. Sci. Techonol. A*, vol. 17, pp. 26-37, 1999.

[78] T. E. F. M. Standaert, M. Schaepkens, N. R. Rueger, P. G. M. Sebel, and G. S. Oehrlein, "High density fluorocarbon etching of silicon in an inductively coupled plasma: Mechanism of etching through a thick steady state fluorocarbon layer," *J. Vac. Sci. Technol. A*, vol. 16, pp. 239-249, 1998.

[79] C. Steinbrüchel, "Universal energy dependence of physical and ion-enhanced chemical etch yields at low ion energy," *Appl. Phys. Lett.*, vol. 55, pp. 1960-1962, 1989.

[80] S. W. Pang, "Surface damage on GaAs induced by reactive ion etching and sputter etching," *J. Electrochem. Soc.*, vol. 133, pp. 784-787, 1986.

[81] F. Gaboriau, G. Cartry, M-C. Peignon, and C. Cardinaud, "Selective and deep plasma etching of $SiO_2$ : Comparison between different fluorocarbon gases ($CF_4$, $C_2F_6$ , $CHF_3$) mixed with $CH_4$ or $H_2$ and influence of the residence time," *J. Vac. Sci. Technol. B*, vol. 20, pp. 1514-1521, 2002.

[82] N. R. Rueger, M. F. Doemling, M. Shaepkens, J. J. Beulens, T. E. F. M. Standaert, and G. S. Oehrlein, "Selective etching of $SiO_2$ over polycrystalline silicon using $CHF_3$ in an inductively coupled plasma reactor," *J. Vac. Sci. Techonol. A*, vol. 17, pp. 2492-2502, 1999.

[83] G. S. Oehrlein, Y. Zhang, D. Vender, and O. Joubert, "Fluorocarbon high-density plasmas. II. Silicon dioxide and silicon etching using $CF_4$ and $CHF_3$," *J. Vac. Sci. Technol. A*, vol. 12, pp. 333-344, 1994.

[84] T. M. Mayer, R. A. Barker, and L. J. Whitman, "Investigation of plasma etching mechanism using beams of reactive gas ions," *J. Vac. Sci. Technol.*, vol. 18, pp. 349-352, 1981.

[85] T. M. Mayer, M. S. Ameen, E. L. Barish, T. Mizutani, and D. J. Vitkavage, "Summary Abstract: Ion-enhanced processes in etching of silicon," *J. Vac. Sci. Technol. B*, vol. 3, pp. 1373-1375, 1985.

[86] Byeong-Ok Cho, Sung-Wook Hwang, Gyeo-Re Lee, and S. H. Moon, "Angular dependence of $SiO_2$ etching in a fluorocarbon plasma," *J. Vac. Sci. Technol. A*, vol. 18, pp. 2791-2798, 2000.

[87] D. P. Hamblen and A. Cha-Lin, "Angular etching correlations from RIE. Application to VLSI fabrication and process modeling," *J. Electrochem. Soc.*, vol. 135, pp. 1816-1822, 1988.

[88] C. Hedlund, C. Strandman, I. V. Katardjiev, Y. Bäcklund, S. Berg, and H.-O. Blom, "Angular dependence of the polysilicon etch rate during dry etching in $SF_6$ and $Cl_2$," *J. Vac. Sci. Techonol. A*, vol. 15, pp. 686-691, 1997.

[89] Marc Schaepkens, Gottlieb S. Oehrlein, Christer Hedlund, Lars B. Jonsson, and H.-O. Blom, "Selective $SiO_2$-to-$Si_3N_4$ etching in inductively coupled fluorocarbon plasmas: Angular dependence of $SiO_2$ and $Si_3N_4$ etching rates," *J. Vac. Sci. Techonol. A*, vol. 16, pp. 3281-3286, 1998.

[90] H. Winters, "Ion-induced etching of $SiO_2$: The influence of mixing and lattice damage," *J. Appl. Phys.*, vol. 84, pp. 2305-2308, 1988.

[91] F. Mendoza, B. Sarette, D. McReynolds, B. Richardson, and J. Holland, "Dry etch technology for large area flat panels," *Semiconductor International*, vol. 22, pp. 143, 1999.

[92] K. H. A. Bogart and V. M. Donnelly, "Composition of trench sidewalls and bottoms for $SiO_2$-masked Si (100) etched in $Cl_2$ plasmas," *J. Appl. Phys.*, vol. 87, pp. 8351-8360, 2000.

[93] G. S. Oehrlein, A. A. Bright, and S. W. Robey, "X-ray photoemission spectroscopy characterization of silicon surfaces after $CF_4/H_2$ magnetron ion etching: Comparisons to reactive ion etching," *J. Vac. Sci. Techonol. A*, vol. 6, pp. 1989-1993, 1988.

[94] S. Kuiper, C. J. M. v. Rijn, W. Nijdam, and M. C. Elwenspoek, "Development and applications of very high flux microfiltration membranes," *J. Membr. Sci.*, vol. 150, pp. 1-8, 1998.

[95] Stein Kuiper, Meint de Boer, Cees van Rijn, Wietze Nijdam, G. Krijnen, and M. Elwenspoek, "Wet and dry etching techniques for the release of sub-micrometre perforated membranes," *J. Micromech. Microeng.*, vol. 10, pp. 171-174, 2000.

[96] D. Hohlfeld, M. Epmeier, and H. Zappe, "A thermally tunable, silicon-based optical filter," *Sens. Actuators, A*, vol. 103, pp. 93-99, 2003.

[97] D. Fotiadis, S. Scheuring, S. A. Müller, A. Engel, and D. J. Müller, "Imaging and manipulation of biological structures with the AFM," *Micron*, vol. 33, pp. 385-397, 2001.

[98] R. Ramesham, "Fabrication of diamond microstructutres for microelectromechanical systems by a surface micromachining process," *Thin Solid Films*, vol. 340, pp. 1-6, 1999.

[99] E. Oesterschulze, W. Scholz, C. Mihalcea, D. Albert, B. Sobisch, and W. Kulisch, "Fabrication of Small Diamond Tips for Scanning Probe Microscopy Application," *Appl. Phys. Lett.*, vol. 70, pp. 435-437, 1997.

[100] W. Kulisch, A. Malavé, G. Lippold, W. Scholz, C. Mihalcea, and E. Oesterschulze, "Fabrication of integrated diamond cantilevers with tips for SPM applications," *Diamond Relat. Mater.*, vol. 6, pp. 906, 1997.

[101] S.-T. Lee, Z. Linb, and X. Jiangc, "CVD diamond films: nucleation and growth," *Mater. Sci. Eng., R*, vol. 25, pp. 123-154, 1999.

[102] P. W. May, "CVD diamond: a new technology for the future?," *Endeavour*, vol. 19, pp. 101-106, 1995.

[103] R. Haubner and B. Lux, "Diamond growth by hot-filament chemical vapor deposition: state of the art," *Diamond Relat. Mater.*, vol. 2, pp. 1277-1294, 1993.

[104] Y. J. Kim, K. Kurihara, K. Suzuki, M. Nomura, S. Mitsugi, M. Chiba, and K. Goto, "Fabrication of Micro-Pyramidal Probe Array with Aperture for Near Field Optical Memory Applications," *Jpn. J. Appl. Phys.*, vol. 39, pp. L1538-L1541, 2000.

[105] S. Werner, O. Rudow, C. Mihalcea, and E. Oesterschulze, "Cantilever Probes with Aperture Tips for Polarisation Sensitive Scanning Near-field Optical Microscopy," *Appl. Phys. A*, vol. 66, pp. S367-S370, 1998.

[106] P. N. Minh, T. Ono, and M. Esashi, "Microfabrication of miniature aperture at the apex of $SiO_2$ tip on silicon cantilever for near-field scanning optical microscopy," *Sensors and Actuators*, vol. 80, pp. 165-171, 2000.

[107] A. Vollkopf, O. Rudow, and E. Oesterschulze, "Technology to reduce the aperture size of microfabricated aperture SNOM tips," *J. Electrochemical Society*, vol. 148, pp. G587-G591, 2001.

[108] E. Oesterschulze, "Recent Developments of Probes for Scanning Probe Microscopy," in *Advances in Imaging and Electron Physics*, vol. 118, t. Mulvey, Ed.: Academic Press, 2001, pp. 129-206.

[109] C. Mihalcea, A. Vollkopf, and E. Oesterschulze, "Reproducible large area microfabrication of sub 100 nm Apertures on hollow tips," *J. Electrochemical Society*, vol. 147, pp. 1970, 2000.

[110] F. Lärmer and A. Schilp, "Method of anisotropically etching silicon." USA patent: 5501893.

[111] J. Ohara, K. Kano, Y. Takeuchi, N. Ohya, Y. Otsuka, and S. Akita, "A new deep reactive ion etching process by dual sidewall protection layer," presented at MEMS, Miyazaki, 2000.

[112] Y. Xia and G. M. Whitesides, "Soft lithography," *Angew. Chem. Int. Ed.*, vol. 37, pp. 550-575, 1998.

[113] Y. S. Kim, J. Park, and H. Lee, "Three-dimensional pattern transfer and nanolithography: modified soft molding," *Appl. Phys. Lett.*, vol. 81, pp. 1011-1013, 2002.

[114] M. Li, L. Chen, and S. Chou, "Direst three-dimensional patterning using nanoimprint lithography," *Appl. Phys. Lett.*, vol. 78, pp. 3322-3324, 2001.

[115] M. Müller-Wiegand, G. Georgiev, E. Oesterschulze, T. Fuhrmann, and J. Salbeck, "Spinodal patterning in organic-inorganic hybrid layer systems," *Appl. Phys. Lett.*, vol. 81, pp. 4940-4942, 2002.

[116] A. Kumar, H. Biebuyck, N. Abbott, and G. Whitesides, "The use of self-assembled monolayers and selective etch to generate pattern gold features," *J. Am. Chem. Soc*, vol. 114, pp. 9188-9189, 1992.

[117] H. W. Deckman and J. H. Dunsmuir, "Natural lithography," *Appl. Phys. Lett.*, vol. 41, pp. 377-379, 1982.

[118] M.-H. Wu and G. Whitesides, "Fabrication of arrays of two-dimensional micropatterns using microspheres as lenses for projection photolithography," *Appl. Phys. Lett.*, vol. 78, pp. 2273-2275, 2001.

[119] U. C. Fischer, J. Heimel, H.-J. Maas, M. Hartig, S. Hoeppener, and H. Fuchs, "Latex bead projection nanopatterns," *Surf. Interface. Anal.*, vol. 33, pp. 75-80, 2002.

[120] C. L. Haynes and R. P. v. Duyne, "Nanosphere Lithography: A Versatile Nanofabrication Tool for Studies of Size-Dependent Nanoparticle Optics," *J. Phys. Chem. B*, vol. 105, pp. 5599-5611, 2001.

[121] S. Matsushita, T. Miwa, and A. Fujishima, "Distribution of components in composite two-dimensional arrays of latex particles and evaluation in terms of the fractal dimension," *Langmuir*, vol. 13, pp. 2582-2584, 1997.

[122] R. Micheletto, H. Fukuda, and M. Ohtsu, "A simple method for production of a two-dimensional, ordered array of small latex particles," *Langmuir*, vol. 11, pp. 3333-3336, 1995.

[123] J. D. Joannopoulos, P. R. Villeneuve, and S. Fan, "Photonic crystals: putting a new twist on light," *Nature*, vol. 386, pp. 143-149, 1997.

[124] S. G. Johnson and J. D. Joannopoulos, *Photonic Crystals: The Road from Theory to Practice*. Dordrecht: Kluwer, Academic, 2001.

[125] E. Yabblonovitch and G. Cody, "Intensity enhancement in textured optical sheets for solar cells," *IEEE Trans. Electron Devices*, vol. ED-29, pp. 300-305, 1982.

[126] G. B. Pavlovski, G. P. Lednyeva, and L. A. Kotomtseva, "Steady-states of two-mode lasing in infinite microcylinder," *J. Aerosol Sci.*, vol. 30, pp. 293-294, 1999.

[127] S. Gianordoli, L. Hvozdara, G. Strasser, T. Maier, N. Finger, K. Unterrainer, and E. Gornik, "GaAs/AlGaAs microresonator quantum cascade lasers," *Physica E*, vol. 7, pp. 29-32, 2000.

[128] S. Anders, W. Schrenk, A. Lugstein, and G. Strasser, "Room temperature lasing of electrically pumped quantum cascade micro-cylinders," *Physica E*, vol. 17, pp. 626-628, 2003.

[129] J. D. Joannopoulos, "Molding the Flow of Light," 1995.

[130] E. Yabblonovitch, "Inhibited Spontaneous Emission in Solid-State Physics and Electronics," *Phys. Rev. Lett.*, vol. 58, pp. 2059-2062, 1987.

[131] C. Giacovazzo, *Fundamentals of crystallography*. Oxford: Oxford Univ. Press, 1995.

[132] G. Georgiev, M. Müller-Wiegand, A. Georgieva, K. Ludolph, and E. Oesterschulze, "Lithography-free fabrication of sub-100nm structures by self-aligned plasma etching of silicon dioxide layers and silicon," *J. Vac. Sci. Technol. B*, vol. 21, pp. 1361-1363, 2003.

[133] E. Oesterschulze, G.Georgiev, M. Müller-Wiegand, A. Georgieva, and K. Ludolph, "Fabrication of sub-wavelength surface structures combining self-assembled masking layer with plasma etching techniques," *J. Vac. Sci. Technol. B*, vol. 21, pp. 2496-2499, 2003.

[134] J. Bhardwaj, H. Ashraf, and A. McQuarrie, "Dry silicon etching for MEMS," in *Annual Meeting of the Electrochemical Society, The Symposium on Microstructures and Microfabricated Systems*. Montreal, Quebec, Canada.: Surface Technology Systems Limited, 1997, pp. 1-13.

[135] J. Bhardwaj and H. Ashraf, "Advanced silicon etching using high density plasmas," presented at SPIE Micromachining and Microfabrication Process Technology, 1995.

[136] J. Hopwood, C. R. Guarnieri, S. J. Whitehair, and J. J. Cuomo, "Electromagnetic fields in radio-frequency induction plasma," *J. Vac. Sci. Techonol. A*, vol. 11, pp. 147-151, 1993.

# List of publications

L. Zambov, B. Ivanov, G. Georgiev, C. Popov, V. Vassilev and G. Beshkov, “Low pressure chemical vapour deposition of $CN_x$ layers by interaction between tetramethylguanidine and cyanurchloride,” *J. Phys. IV*, vol. 9, pp Pr8-501-509, 1999.

B. Ivanov, L. Zambov, G. Georgiev, C. Popov, M. Plass and W. Kulisch, “Low-Pressure CVD of Carbon Nitride Using Triazine-Containing Precursors,” *Adv. Mater., CVD*, vol. 5, pp 265-273, 1999.

L. Zambov, B. Ivanov, C. Popov, G. Georgiev, I. Stoyanov and M. Dimitrov, “Characterization of low-dielectric constant SiOCN films synthesized by low pressure chemical vapour deposition,” *J. Phys IV*, vol. 11, pp Pr3-1005-1013, 2001.

E. Oesterschulze, G. Georgiev, A. Vollkopf and O. Rudow, "Transmission Line Probe on Base of a Bow-Tie Antenna," *J. Microscopy*, vol. 202, pp 39-44, 2001.

O. Rudow, A. Vollkopf, M. Müller-Wiegand, G. Georgiev and E. Oesterschulze, "Theoretical Investigations of a Coaxial Probe Concept for Scanning Near-field Optical Microscopy," *Opt. Commun.*, vol. 189, pp 187-192, 2001.

A. Vollkopf, G. Georgiev, O. Rudow, M. Müller-Wiegand and E. Oesterschulze, “Technology to Reduce the Aperture Size of Microfabricated Silicon Dioxide Aperture Tips” *J. Electrocem Soc.*, vol. 148, pp G587-G591, 2001.

G. Georgiev, A. Vollkopf, D. Albert, and E. Oesterschulze, “Optimized Technique for Aperture Probe Fabrication”, presented at DPG-Frühjahrstagung, Hamburg, 2001.

M. Müller-Wiegand, G. Georgiev, E. Oesterschulze, T. Fuhrmann and J. Salbeck, "Spinodal patterning in organic-inorganic hybrid layer systems," *Appl. Phys. Lett.*, vol. 81, pp 4940-4942, 2002.

E. Oesterschulze, R. Kassing, and G. Georgiev, "Verfahren zur Herstellung wenigstens einer kleinen Öffnung in einer Schicht auf einem Substrat und damit hergestellte Bauelemente," Patentanmeldung, September 2002.

E. Oesterschulze, R. Kassing, and G. Georgiev, "Verfahren zur Herstellung einer eine schmale Schneide oder Spitze aufweisenden Struktur und mit einer solchen Struktur versehener Biegebalken," Patentanmeldung, September 2002.

E. Oesterschulze, R. Kassing, and G. Georgiev, "Verfahren zur Herstellung von stab- und/oder lochförmigen Strukturen in einer Substratoberflache, damit hergestelltes Bauelement und Anwendung des Verfahrens," Patentanmeldung, September 2002.

A. Vollkopf, O. Rudow, M. Müller-Wiegand, G. Georgiev and E. Oesterschulze, "Influence of the oxidation temperature on the fabrication process of silicon dioxide aperture tips," *Appl. Phys. A*, vol. 76, pp 923-926, 2003.

T. Ono, E. Oesterschulze, G. Georgiev, A. Georgieva and R. Kassing, “Field-assisted assembly and alignment of carbon nanofibres” *Nanotechnology*, vol. 14, pp 37-41, 2003.

G. Georgiev, K. Ludolph, M. Müller-Wiegand, A. Georgieva and E. Oesterschulze “Self-assembled Patterning and MEMS Based Fabrication of 2D Photonic Crystals” presented at MRS Fall Meeting, December 1 – 5, Boston, USA, 2002

G. Georgiev, M. Müller-Wiegand, A. Georgieva, K. Ludolph and E. Oesterschulze, "Lithography-free fabrication of sub-100nm structures by self-aligned plasma etching of silicon dioxide layers and silicon," *J. Vac. Sci. Technol. B*, vol. 21, pp 1361-1393, 2003.

E. Oesterschulze, G.Georgiev, M. Müller-Wiegand, A. Georgieva and K. Ludolph, "Fabrication of sub-wavelength surface structures combining self-assembled masking layer with plasma etching techniques," *J. Vac. Sci. Technol. B*, vol. 21, pp 2496-2499, 2003.

W. Kulisch, C. Popov, S. Boycheva, G. Beshkov, V. Vorlicek, P. N. Gibson, G. Georgiev, “Investigation of the growth mechanism and structure of nanocrystalline diamond films by rapid thermal annealing,” submitted in *Thin Solid Films*

# Acknowledgments

At this place, I would like to thank numerous persons from whom I have received much support during completion of this work.

First of all, I would like to thank Prof. Dr. R. Kassing for giving me the chance to start and complete this work, for his energetic support by financial means and unreserved confidence and trust.

I am deeply grateful to PD Dr. E. Oesterschulze, for his detailed and fruitful discussions, giving substantial part for the solutions of many problems and directing me to the right path for completing this work.

My special thanks to Dr. O. Rudow and Dr. A. Vollkopf for the collaboration introducing me in the SNOM and SNOM cantilever fabrication and special appreciation for helping me in adaptation in new working environment.

As well, I would like to thank Dr. T. Leinhos, Dr. T. Kurzenknabe, Dr. M. Müller-Wiegand and Dipl. Phys. K. Ludolph for the cooperative team work.

I owe a dept of gratitude to Dr. C. Popov for opening the door of science for me and his selflessly help.

To Dr. W. Scholz I am thankful for the lithography mask fabrication, his advices about technological problems and SEM imaging.

I would like to express my deep appreciation to Dipl. Phys. D. Albert, Dipl. Ing. A. Malkomes and Mr. M. Plätzer for their unhesitating help for all small and big technical problems, which occurred during this work.

I wish to thank Dr. K. Maßeli for the enormous help in administrative and organizational matters.

I would like to thank Assoc. Prof. Dr. V. Vassilev, Assoc. Prof. Dr. L. Zambov and Dr. B. Ivanov for the help in my first scientific steps.

My special thanks to Dr. K. Berge and Dr. M. Bürgener, for performing the XPS measurements.

To all co-workers of the Technological Physics I am thankful, especially to the cooperatively secretary team (P. Draude, U. Gerlach-Groß, C. Pfitzmann, and H. Krug)

At last but not at least, I am deeply thankful to my family for their permanent support and encouragement.

# Curriculum Vitae

| | |
|---|---|
| Name: | Georgi Todorov Georgiev |
| Date/Place of Birth: | 5 August 1972, Sofia, Bulgaria |
| 1979 – 1987 | Primary School, Sofia Bulgaria |
| 1987 – 1991 | Technical School for Polymer Technologies, Sofia, Bulgaria |
| 1991 – 1996 | University of Chemical Technology and Metallurgy, Department of Semiconductor Technology, Sofia, Bulgaria |
| 1996 | Diploma thesis under the supervision of Dr. D.-B. Daspet at LAAS, CNRS, Toulouse, France |
| 1998 – 2000 | University of Chemical Technology and Metallurgy – research engineer in CVD group |
| 2000 | University of Kassel, Institute of Microstructure Technologies and Analytics – PhD student in physics under the supervision of Prof. Dr. R. Kassing |

# Declaration

I certify herewith that I made this thesis independently, without any disallowed assistance and I did not use others than the aids indicated in the thesis.
I marked all places, which are literally or in a general manner taken out of published or unpublished books or articles. No part of this thesis has been previously submitted in support of an application for any other degree or qualification in this or any other University.

Hiermit versichere ich, dass ich die vorliegende Dissertation selbständig und ohne unerlaubte Hilfe angefertigt und andere als die in der Dissertation angegebenen Hilfsmittel nicht benutzt habe.
Alle Stellen, die wörtlich oder sinngemäß aus veröffentlichten oder unveröffentlichten Schriften entnommen sind, habe ich als solche kenntlich gemacht. Kein Teil dieser Arbeit ist in einem anderen Promotions- oder Habilitationsverfahren verwendet worden.